VALIDATION OF THE β-OSLO METHOD; AN INDIRECT METHOD FOR CONSTRAINING NEUTRON-CAPTURE CROSS SECTIONS

By

Katherine Louise Childers

A DISSERTATION

Submitted to
Michigan State University
in partial fulfillment of the requirements
for the degree of

Chemistry - Doctor of Philosophy

2021

ABSTRACT

VALIDATION OF THE β-OSLO METHOD; AN INDIRECT METHOD FOR CONSTRAINING NEUTRON-CAPTURE CROSS SECTIONS

By

Katherine Louise Childers

One of the prevalent questions in nuclear science is the origin of the elements. There are two stellar nucleosynthesis processes considered to be responsible for the production of the majority of the abundances of the elements heavier than iron; the slow neutron-capture process (s-process) and the rapid neutron-capture process (r-process). Both of these processes are characterized by the successive capture of neutrons on nuclei, with the major differences between the processes being the timescale over which the processes occur and the host environment. The s-process occurs in low neutron-density environments, such as low- to intermediate-mass stars, and proceeds slowly along the valley of stability. Since the nuclei involved are close to stability, the reactions involved are amenable to direct measurements. The r-process progresses through an explosive event with high neutron densities which drives material far from stability. The recent observation of a neutron star merger event by LIGO and Virgo and the subsequent electromagnetic follow up has demonstrated that an r-process event can occur in these rare events, but it has not ruled out other potential astrophysical sites. To better understand and model the r-process, several nuclear properties are needed for a large number of nuclei, including neutron-capture cross sections. R-process nuclei are not viable for direct measurement of neutron-capture cross sections since the nuclei involved are far from stability, and thus have short half-lives. Therefore, several indirect measurement techniques have been developed to provide experimental constraints on neutron-capture cross sections. One such method is the β-Oslo method, which uses β decay to populate highly

excited states of a nucleus. The resulting de-excitation via the emission of γ rays is used to extract statistical nuclear properties of the daughter nucleus. These properties are then used as input in a reaction model to constrain the neutron-capture cross section. The β-Oslo method can provide a large number of constrained neutron-capture cross sections far from stability, but it is necessary to validate the method using a direct neutron capture measurement. This work will present a validation of the β-Oslo method in the A = 80 mass region with the ^{82}Se(n,γ)^{83}Se reaction. The nuclide ^{83}Se can be accessed through the β-decay of ^{83}As, which was studied at the National Superconducting Cyclotron Laboratory with the total absorption spectrometer, SuN. Using the β-Oslo method, the cross section of the ^{82}Se(n,γ)^{83}Se reaction was constrained. A direct measurement of the ^{82}Se(n,γ)^{83}Se reaction was performed with the Detector for Advanced Neutron Capture Experiments and the cross section obtained from the direct measurement is compared to the cross section determined using the β-Oslo method. The results are in good agreement, validating the β-Oslo method as a viable method for constraining neutron-capture cross sections.

To Mom and Dad: Jo and Malcolm Childers

ACKNOWLEDGMENTS

It has definitely been a journey to get to this point, and I have met so many amazing people along the way. It is hard to express in words how much I appreciate all of you, but I will try!

First off, I would like to thank my advisor, Sean Liddick. Thank you for giving me so many opportunities to learn, through my research, the many experiments, and all of the conferences and schools you encouraged me to go to. I appreciate your patience and all of the knowledge you have passed on. (Also, thanks for all the fajitas.) I would also like to thank my committee members: Paul Mantica, Dave Morrissey, and Artemis Spyrou. Thank you all for your guidance and support. I have always felt that I could come talk to any of you for advice or help.

A huge thank you goes to Aaron Couture. I dont think I would have been able to get through the selenium analysis without you. Thank you for putting up with me for so long (probably a little longer than expected...) and thank you for all the support and advice. I am really lucky to have had the opportunity to work with you, and I have learned so much. I would also like the thank the rest of the DANCE team: Chris Prokop, Cathleen Fry, Shea Mosby, and John Ullmann. Being able to run an experiment out at LANL was an awesome opportunity and I appreciate all of your support so much.

I would be remiss to not give a shout out to the Chemistry and Physics faculty at Otterbein University, especially Robin Grote, Joan Esson, Carrigan Hayes and Jerry Jenkins. You guys were supportive throughout undergrad and taught me the skills I needed to be successful in graduate school and become the scientist I am today. I have many fond memories of all of you and my time at Otterbein.

Graduate school would not be possible without the support and encouragement of friends, and I have made some wonderful friends during my time here. Becky Lewis, thank you for welcoming me in when I started grad school and showing me the ropes, and for always cheering me on, even from afar. Ben Crider, thank you for your help (and infinite patience) with analysis and coding. I have learned so much from you. Andrea Richard, a simple thank you isn't enough. You have been there for me through some tough times, and you always know what to say to support and encourage me. Thank you for all of your mentorship, and most of all, your friendship. Thank you to the many other friends I have made: Kyle Brown, Stephanie Lyons, Mallory Blyth, Caley Harris, Alicia Palmisano, Aaron Chester, and many more. I appreciate you guys so much and will cherish the many memories.

Lastly, thank you to my family. Aunt Cathy, thank you for always being so excited and encouraging me to go for what I wanted. The time I have spent with you has been a big part of my life. Those of you that know me know that I of course need to mention the smallest member of my family, my guinea pig Revan. You won't be able to read this but thank you for being the best little buddy and roommate. Most importantly, thank you to my parents, Jo and Malcolm Childers. I am where I'm at today because of you. Thank you for your endless support, for cheering on every accomplishment, no matter how big. I love you both so much.

TABLE OF CONTENTS

LIST OF TABLES

LIST OF FIGURES

Chapter 1

Introduction

1.1 Stellar nucleosynthesis of heavy elements

The origin of the elements remains one of the mysteries that scientists are still working to understand today. It is known that the majority of the elements on Earth were not created terrestrially and instead were present when the Earth was formed. So where did they come from? The lightest nuclei (hydrogen, helium, and trace amounts of lithium) were created through primordial nucleosynthesis during the Big Bang. After the Big Bang, as galaxies and the earliest stars, or protostars, began forming, conditions became right for fusion reactions to begin, starting a chain of stellar nucleosynthesis pathways. These fusion reactions are responsible for the production of most of the nuclei up to A $\sim$ 60. However, around A $\sim$ 60, there is a peak in the nuclear binding energy of nucleons as a function of mass, and combined with the large Coulomb barrier between charged particles, these fusion reactions are no longer energetically favored. A reaction that *is* energetically favorable is neutron capture, since there is no Coulomb barrier hindering the addition of a neutron to nuclei. Neutron capture is instead influenced by the free neutron density in the stellar environment. There are two main neutron capture processes, the slow neutron-capture process (s-process), and the rapid neutron-capture process (r-process). The s-process is characterized by a low neutron density ($\sim 10^{10}/cm^3$) environment [1], which leads to a relatively long time between

neutron captures, hundreds or thousands of years, compared to the relatively quicker β-decay half lives. This keeps the s-process close to the valley of stability. A schematic of the s-process pathway is shown in Figure 1.1. Since the nuclei involved in the s-process are close to stability, many of the properties of these nuclei have been experimentally determined, and therefore, through the use of astrophysical models, the basic mechanisms and astrophysical sites of the s-process are fairly well constrained. Currently, theoretical studies support low to intermediate mass asymptotic giant branch (AGB) stars as one of the sites of the s-process [1]. Unlike the s-process, there is much that is still unknown about the r-process, which will be discussed in more detail in the following section.

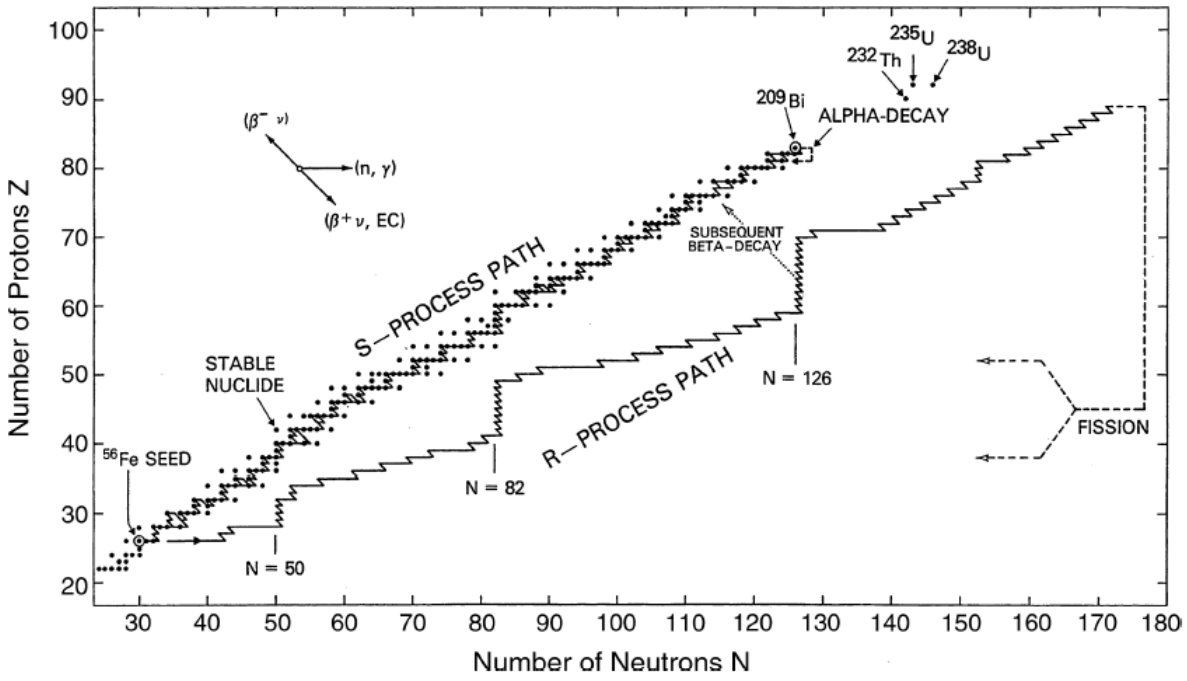

Figure 1.1: A schematic of the paths of both the s-process and r-process and the subsequent decay modes. From [2], © 2006 John Wiley & Sons, Inc.

1.2 The rapid neutron-capture process

The r-process occurs in stellar environments with a much higher neutron density ($\sim 10^{20}/cm^3$) than the s-process, and because of this, the rate of neutron capture is also much higher. In most cases, the time scale of neutron capture reactions will be much less than β-decay half-lives (on the order of fractions of a second), leading to many rapid, sequential neutron captures before β decaying, creating a zig-zag pattern progressing up the chart of the nuclides. This drives the r-process farther from stability, as shown in Figure 1.1, to the neutron-rich region of the chart of the nuclides. Eventually, the neutron density will drop, neutron-capture reactions will cease, and the neutron-rich nuclei produced will β decay back to stability, populating the nuclei in between.

The observed solar abundance of heavy nuclei produced is assumed to be a combination of both the s-process and the r-process. (As a note: The solar abundances are considered here as the default abundances of elements in the universe, or the cosmic abundances.) Since the s-process is better understood and easier to model, the solar abundance pattern resulting from the r-process is determined by subtracting the contribution of the s-process from the total observed solar abundance. The resulting r-process residual abundance pattern is shown in Figure 1.2. The three main peaks that are visible in the r-process abundance, at A = 80, 135, and 195, correspond to the shell closures at the magic neutron numbers of 50, 82, and 126 (see Figure 1.1). Nuclei with these magic numbers will have additional stability, and will therefore accumulate as the reaction flow passes through them, leading to an increase in their abundance.

Due to the exotic nature of the nuclei produced along the r-process path, there is uncertainty in the properties of many of these nuclei, as well as the general astrophysical conditions

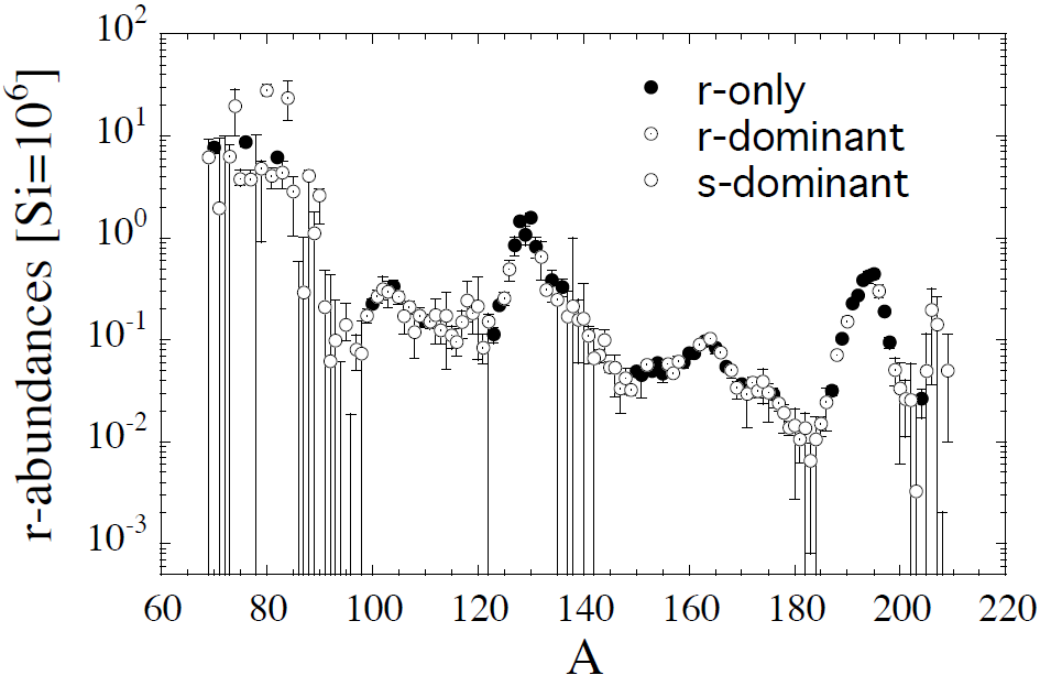

Figure 1.2: Calculated residual abundances produced through the r-process, as a function of mass number. Reprinted from [3], with permission from Elsevier.

that drive the r-process. In order to define the astrophysical conditions of the r-process, the astrophysical locations must be determined. While there have been many locations proposed, the most likely candidates are supernovae and neutron star mergers [1, 3]. Unfortunately, there has been no evidence of r-process nuclei observed in supernova events so far, and even the most promising models have issues, such as not producing a successful explosion or the heaviest nuclei, that prevent a conclusive result [1]. Neutron-star mergers were originally put forth as a potential r-process site, as this site has the high neutron density needed to support the r-process. However, until recently, a neutron-star merger had never been observed, and thus were not considered to be as likely as supernova. In August of 2017, the Advanced LIGO and Advanced Virgo gravitational-wave detectors made the first observation of a neutron star merger, GW170817 [4]. The subsequent transient kilonova event that was observed had characteristics consistent with what would be expected of an r-process environment and

the production of lanthanide elements [5–7], supporting neutron-star mergers as a site of the r-process. There are still many questions remaining about astrophysical conditions and other possible astrophysical sites have been hypothesized [8]. Every astrophysical site is characterized by distinct conditions, including the temperature, neutron density, and initial composition. These different conditions will produce a unique abundance pattern, which can be modeled and compared to the observed solar r-process abundance pattern. Comparisons have proven to be difficult, however, due to the uncertainties the nuclear properties that are needed for these models, namely, the masses, β-decay half lives, and neutron-capture cross sections.

1.3 Uncertainties of nuclear properties

In order to determine the impact that the uncertainties of nuclear properties have on modeled abundance patterns, a study employing Monte Carlo simulations was performed by Mumpower et al. [8]. The masses, β-decay half-lives, and neutron-capture cross sections over a large mass range were varied using a probability distribution based on the current uncertainties of each property, and for each set of inputs, a simulated r-process abundance pattern was generated. Shown in Figure 1.3 are abundance patterns calculated using three different mass models (HFB-17 [9], DZ [10], and FRDM1995 [11]). Based on a comparison to measured masses, the uncertainty of the masses calculated via the models was determined to be 500 keV rms. The uncertainty in the calculated abundance pattern, based on the propagation of the mass uncertainty, can be large, causing difficulty in comparing to the known abundance pattern. If an artificial reduction of the uncertainty is performed, to 100 keV rms (indicated by the dark band in Figure 1.3), then the calculated abundance pat-

tern become more distinct, but in some areas the uncertainty still remains large. However, without this reduction, the light band represents the current predictive power of these mass models. For β-decay half lives, current uncertainties were approximated to be a factor of 10 based on a comparison of known experimental half-lives to a global QRPA calculation of half-lives [8]. For neutron-capture cross sections, a comparison of experimental values to those calculated using three different models (TALYS [12], NONSMOKER [13], and CIGAR [14]) led to the determination of a current uncertainty of a factor of 1000. Shown in Figure 1.4 are abundance patterns calculated with the uncertainties associated with β-decay half lives and neutron-capture rates. Again, these uncertainty bands are large. With the uncertainty of the masses, β-decay half-lives, and neutron-capture cross sections combined, it becomes clear that the current theoretical models used to predict these inputs lead to error bars that are too large to distinguish between different astrophysical models. Therefore, the reduction of uncertainty introduced into the calculation of abundance patterns from nuclear properties of heavy nuclei is of great importance. There have been advances in the measurements of both masses (see References [15–18] for a selection of recent work) and β-decay half-lives (see References [19–22]) of nuclei that are critical for r-process simulations. However, the uncertainty in neutron-capture cross sections for most r-process nuclei remain large due to the difficulty of directly measuring these reactions. A direct measurement of a neutron-capture reaction requires a target of the nucleus of interest, which, in the case of r-process nuclei far from stability, is not feasible due to their short half lives. This has led to the development of indirect methods of constraining neutron-capture cross sections using experimental information [23]. Many of these indirect methods (as well as current theoretical cross-section calculations) rely on the Hauser-Feshbach statistical model of neutron capture.

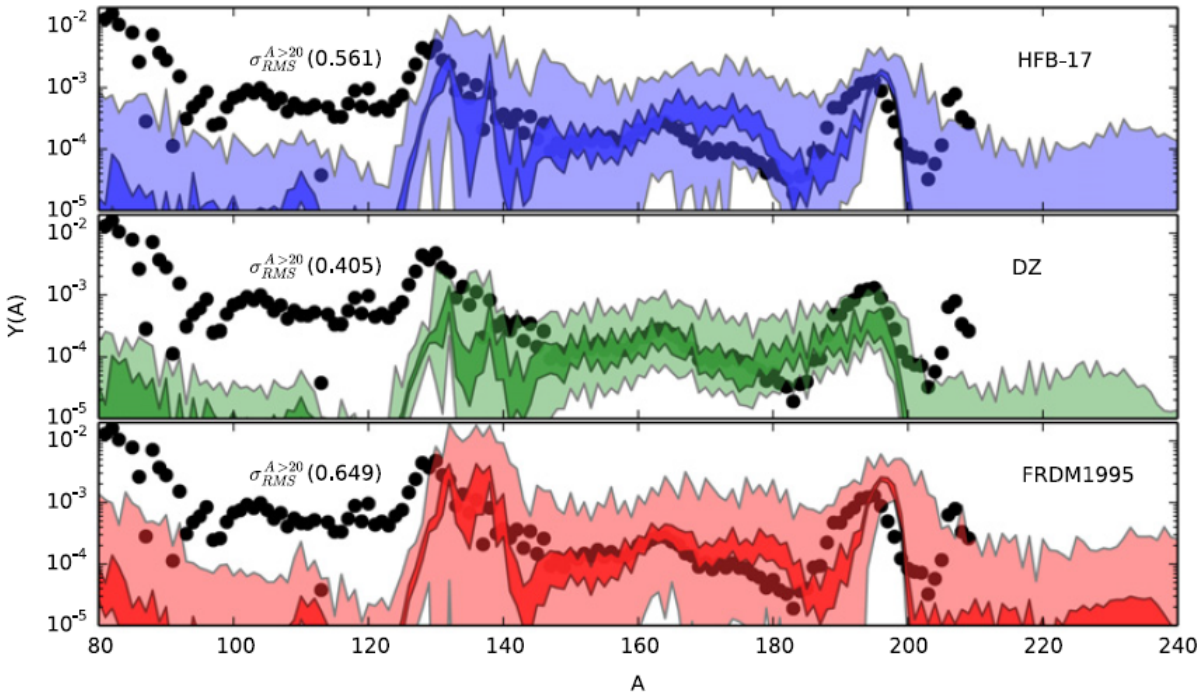

Figure 1.3: Residual solar r-process abundance pattern (black dots) compared to modeled r-process abundance patterns using three different mass models. The lighter bands represent the uncertainty of the calculation with the rms error compared to known masses. The darker bands represent the uncertainty when the rms error is artificially reduced to 100 keV. Reprinted from [8], with permission from Elsevier.

1.4 Hauser-Feshbach model of neutron capture

In lieu of directly measuring neutron-capture reactions, the cross section can be calculated using the Hauser-Feshbach model of neutron capture [24]. The Hauser-Feshbach model describes neutron capture as a two-step process; first, a compound nucleus is formed, and second, the compound nucleus decays via the emission of γ rays. It is assumed that the second step is independent of the first step [25], and therefore, the subsequent decay of the compound nucleus is independent of the method through which the nucleus was formed. Instead, the decay is governed by the statistical properties of the nucleus. The Hauser-Feshbach model relies on information about the interaction between the neutron and the target nucleus (optical model potential - discussed in Section 1.4.1), as well as information

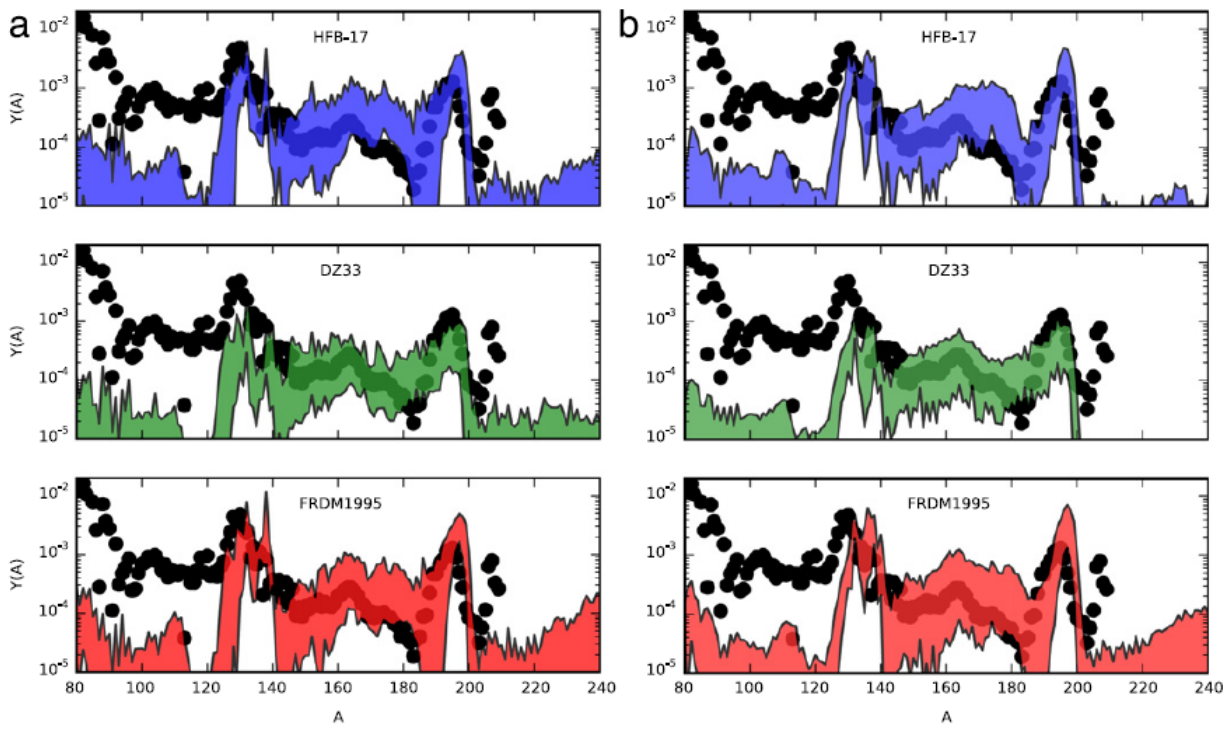

Figure 1.4: (a) Comparison of the residual solar r-process abundance pattern to abundance patterns modeled for the same three mass models as in Figure 1.3. Here the uncertainty taken into account is that of the β-decay half-lives. (b) Same as (a) but with the uncertainty of neutron-capture rates studied instead of the β-decay half-lives. Reprinted from [8], with permission from Elsevier.

describing statistical properties of the compound nucleus formed during the reaction (nuclear level density - Section 1.4.2 and γ-ray strength function - Section 1.4.3). In many cases, especially for r-process nuclei, most of this information is not known, so theoretical models are required to obtain the necessary information. Validating indirect means of inferring neutron-capture rates, which is the subject of this thesis, is necessary to provide confidence when extrapolating theoretical models to unknown nuclei.

1.4.1 Optical model

An optical model potential is used to describe the interaction that takes place between the target nucleus and the incoming neutron. The central assumption of the optical model

is that the complicated interaction can be represented by a single mean field potential. There are two main types of optical model potentials - a phenomenological potential, and a microscopic potential. The optical model potential most often used for r-process calculations is that of Koning and Delaroche [26], which is a phenomenological optical model. A suitable analytical form for the potential is chosen (often the Woods-Saxon potential), and parameters are determined via fitting to experimental data, where available. If experimental data are not available, a global parameterization is used. In a microscopic optical model potential, the strength and shape of the nuclear potential is calculated by folding the nucleon-nucleon effective interaction with the nuclear density distribution. A semi-microscopic (in between phenomenological and microscopic) optical model potential that is available and commonly used is the Jeukenne-Lejeune-Mahaux (JLM) model [27]. This potential usually results in a calculated neutron-capture cross section that is within 20% of what would be obtained using the Koning-Delaroche model. The most important quality (particularly for r-process nuclei) of an optical model potential is that it is able to reliably predict nuclear properties that are unable to be measured experimentally. Fortunately, for most r-process nuclei, the uncertainty propagated from the optical model potential is the smallest source of uncertainty in the calculated cross section. Most of the uncertainty in the results of the Hauser-Feshbach calculation comes from the models used for calculating the properties that will be discussed next - the nuclear level density and the γ-ray strength function.

1.4.2 Nuclear level density models

The nuclear level density (NLD) is the number of energy levels available at a given excitation energy (E_x), spin (J), and parity (π). It can be represented by the function:

$$\rho(E_x, J, \pi) = \Delta N(E_x, J, \pi)/\Delta E_x, \tag{1.1}$$

where $\Delta N(E_x, J, \pi)$ is the number of levels with the energy bin ΔE_x. A level spacing parameter, $D(E_x, J, \pi)$, can be determined as the inverse of the level density,

$$D(E_x, J, \pi) = 1/\rho(E_x, J, \pi). \tag{1.2}$$

The total level density within an excitation energy bin can then be calculated by summing over all spins and parities. In cases where only a subset of levels are populated, it is important to know the distribution of the spin and parity amongst the states in the nucleus. The spin and parity distributions are commonly assumed to be uncorrelated. The spin distribution, $s(E_x, J)$, is dependent on excitation energy and spin, and following Ericson [28], and can be approximated as:

$$s(E_x, J) \simeq \frac{2J+1}{2\sigma^2(E_x)} e^{-\frac{(J+1/2)^2}{2\sigma^2(E_x)}}. \tag{1.3}$$

The σ^2 parameter in Eq. 1.3 is called the spin cut-off parameter. This expression is derived assuming that many particles and holes are excited to higher-lying states, and has been found to be an appropriate approximation for J $\leq$ 30 [28]. In a study done by von Egidy and Bucurescu [29], a set of 310 nuclei were fit with Eq. 1.4 to obtain an empirical

parameterization of σ^2 based on its mass dependence.

$$\sigma^2(E_x) = p_1 A^{p2}(E - 0.5P\acute{a})^{p3} \tag{1.4}$$

From the fit of the above equation, it was determined that $p_1 = 0.391$, $p_2 = 0.675$, and $p_3 = 0.312$. $P\acute{a}$ is the deuteron pairing energy, which can be calculated using mass excess values $M(A, Z)$ via:

$$P\acute{a} = \frac{1}{2}[M(A+2, Z+1) - 2M(A, Z) + M(A-2, Z-1)]. \tag{1.5}$$

The fit was repeated separately for sets of only the even-even, odd, and odd-odd nuclei and the parameters determined from the fit were found to be essentially the same as the parameters listed above, confirming this parameterization to be independent of nuclear shell structure differences. It is worth noting that the nuclei used in this study were all stable or close to stability. There is a trend in experimentally determined spin distribution favoring lower spins at lower excitation energies and the distribution shifting to higher spins as the excitation energy increases. It is assumed that this trend will hold for nuclei further from stability, but as of now, the spin distribution is not considered to be well known for nuclei at the far reaches of the nuclear chart.

The two parities (positive and negative) are usually assumed to be distributed equally across all nuclear states, regardless of energy. It has been shown through several experimental and theoretical studies that even if there is a deviation from an equal number of positive and negative parities, it does not have a large effect of the determination of the level density [23].

The first nuclear level density model developed was the Fermi gas (FG) model, which described the nucleus as a gas of nucleons arranged in single-particle orbits. These nucleons behave in accordance with the Pauli exclusion principle, which states that they must each have a unique set of quantum numbers. In the lowest energy configuration of a nucleus, the nucleons will fill up the lowest-energy single-particle states. When energy is added to the nucleus, nucleons are excited to higher energy single particle states. The number of available configurations and the density of the single particle states will both increase with an increasing amount of energy available to the system. Using this description, Bethe determined a level density function [30],

$$\rho(Ex) = \frac{\pi e^{2\sqrt{aE_x}}}{12a^{1/2}E_x^{5/4}} \tag{1.6}$$

where E_x is the excitation energy, and a is the level density parameter, determined using the single particle level density parameters of protons (g_p) and neutrons (g_n),

$$a = \frac{\sqrt{\pi}}{6}(g_p + g_n). \tag{1.7}$$

Since nucleons do interact, a modification was made to the FG model, and led to the Back-shifted Fermi Gas (BSFG) model [31]:

$$\rho(Ex) = \frac{\pi e^{2\sqrt{a(E_x-\Delta)}}}{12a^{1/2}(E_x-\Delta)^{5/4}}. \tag{1.8}$$

The BSFG model includes a shift parameter, Δ, which is intended to take into account the effect of the interactions of nucleons, based on the separation energy the interacting nucleons must overcome [32,33]. Δ can be calculated from the pairing energy of protons and neutrons,

but along with the level density parameter a, it can be adjusted to match an experimental nuclear level density [12].

Another commonly used level density model is the Constant Temperature (CT) model [34], which describes the level density by the function,

$$\rho(Ex) = \frac{1}{T} e^{(Ex - E_0)/T} \tag{1.9}$$

where E_x is the excitation energy and E_0 and T are free parameters that are related to an energy shift and constant temperature, respectively, that can be found by fitting to experimental data. The CT model was found to reproduce known nuclear level densities are lower excitation energies, while the FG and BSFG models were found to reproduce level densities are higher energies better [34, 35]. For this reason, the CT and BSFG models are often used together to describe a full range of excitation energy.

While the nuclear level density models described above do a reasonable job at reproducing experimental data, they are unable to describe some of the finer details in the level density. When used to extrapolate to nuclei far from the valley of stability, the nuclear level density models become more unreliable, with no experimental data to help constrain the model, which leads to a larger uncertainty in the calculated cross section. Ideally, a microscopic model, based on fundamental interactions and first principles, would be used to calculate level densities. However, the limits of computational power limit the applicability of microscopic approaches to determining the nuclear level density. A recently developed approach by Goriely et al. has been used to calculate level densities for a large range of nuclei (up to 150 MeV and J=30) using a Hartree-Fock basis [36]. Several other versions of this approach have also been developed; the spin- and parity-dependent combined Hartree-Fock-Bogoliubov and

combinatorial method [37], and the temperature-dependent Hartree-Fock-Bogolyubov-plus-combinatorial method [38]. To date, the efficacy of microscopic methods for level densities of nuclei far from stability has been difficult to determine due to the scarcity of data available for comparison.

1.4.3 γ-ray strength function models

The γ-ray transmission coefficient $\mathcal{T}(E_\gamma)$ represents the probability of a γ ray of energy E_γ being emitted from a nucleus. $\mathcal{T}(E_\gamma)$ is related to the γ-ray strength function (γSF), $f(E_\gamma)$, through the expression

$$\mathcal{T}_{XL}(E_\gamma) = 2\pi E_\gamma^{(2L+1)} f_{XL}(E_\gamma), \tag{1.10}$$

where X denotes the type of electromagnetic radiation the transition is (E for electric and M for magnetic), and L denotes the angular momentum. In general, the strength function can be defined in terms of the average partial radiative width, Γ_{XL}, of a γ ray of energy E_γ from an initial energy level E_i, with a spin J_i and parity π_i, and the level density at that energy, $\rho(E_i, J_i, \pi_i)$ [39]:

$$\overleftarrow{f}_{XL}(E_i, J_i, \pi_i, E_\gamma) = \frac{\langle \Gamma_{XL}(E_i, J_i, \pi_i, E_\gamma)\rangle \rho(E_i, J_i, \pi_i)}{E_\gamma^{(2L+1)}}. \tag{1.11}$$

Through the principle of detailed balance, this "downward" strength function (designated by the left arrow symbol) describing γ decay, can be connected to the "upward" strength function (designated by the right arrow symbol), which describes the reverse process of photoabsorption. This "upward" strength function can be described in terms of the average

photoabsorption cross section, $\sigma(E_\gamma)$ [39]:

$$\overrightarrow{f}_{XL}(E_f, J_f, \pi_f, E_\gamma) = \frac{1}{(2L+1)(\pi\hbar c)^2} \frac{\langle \sigma_{XL}(E_f, J_f, \pi_f, E_\gamma) \rangle}{E_\gamma^{(2L+1)}}, \tag{1.12}$$

where E_f is the final state after absorption, with a spin J_f and parity π_f. One feature of the photoabsorption cross section that has been observed to be constant throughout the nuclear chart is a broad E1 resonance, called the Giant Dipole Resonance (GDR). Through the Brink hypothesis [40,41], which states that the shape of the photoabsorption cross section is independent of the initial excitation energy of the nucleus, it can be assumed that the shape of the E1 cross section at an excited state will be the same as at the ground state. Through this assumption and the connection of the photoabsorption cross section to the γSF, the γSF can be described using the shape of the lower energy tail of the GDR. Therefore, the GDR can be used to help constrain models of the γSF, since there is generally more data available on the GDR than on the γSF.

In order to describe the shape of the GDR, and in turn the γSF, several phenomenological models have been developed. One of the first functions to be used to fit the GDR is the Standard Lorentzian (SLO) function, which was developed by Brink and Axel [40, 41]. The SLO function is characterized by the energy (E_{XL}), strength (σ_{XL}), and width (Γ_{XL}) of the GDR:

$$f_{XL}(E_\gamma) = K_{XL} \frac{\sigma_{XL} E_\gamma \Gamma_{XL}^2}{(E_\gamma^2 - E_{XL}^2)^2 + E_\gamma^2 \Gamma_{XL}^2}, \tag{1.13}$$

where K_{XL} is defined as:

$$K_{XL} = \frac{1}{(2L+1)\pi^2\hbar^2c^2}. \tag{1.14}$$

This function was found to fit the GDR well and was thus used to represent the E1 strength, considered the dominant contribution to the GDR, as well as contributions from M1 and E2 transitions. Kopecky and Uhl introduced a temperature dependence to the SLO, in order to account for a discrepancy between the SLO function and GDR data at lower energies, that ultimately, can impact calculations of the neutron-capture cross section [42]. This new function, the Generalized Lorentzian, is predominantly used to represent the E1 component of the GDR and is also characterized by the energy (E_{E1}), strength (σ_{E1}), and width (Γ_{E1}) of the GDR:

$$f_{E1}(E_\gamma, T) = K_{E1}\left(\frac{E_\gamma \tilde{\Gamma}_{E1}(E_\gamma)}{(E_\gamma^2 - E_{E1}^2)^2 + E_\gamma^2 \tilde{\Gamma}_{E1}(E_\gamma)^2} + \frac{0.7\Gamma_{E1}4\pi^2T^2}{E_{E1}^3}\right)\sigma_{E1}\Gamma_{E1}, \quad (1.15)$$

where

$$\tilde{\Gamma}_{E1}(E_\gamma) = \Gamma_{E1}\frac{E_\gamma^2 + 4\pi^2T^2}{E_{E1}^2}. \quad (1.16)$$

The temperature, T, can be approximated by $T \approx \sqrt{E_x/a}$, and is connected to the Fermi Gas nuclear temperature, but currently it is often used as a free parameter when fitting data. This function differs from the SLO function most significantly at lower γ-ray energies, but it has been found to correct discrepancies in cross section calculations using the SLO function.

Recently, a surprising feature of the γSF was discovered - an enhancement in the strength at low γ-ray energies (below 4 MeV) and high excitation energies. This feature has been called the "upbend", and was first seen in Fe isotopes in 2004 [43]. Since then, the upbend has been observed in many other nuclei, including Mo [44, 45], Sc [46, 47], La [48], and Sm [49]. One of the Mo studies used a different technique to determine the γSF [45], thus confirming the upbend as being a feature of the γSF, and not the method used. The upbend has been found to impact the calculation of neutron-capture cross sections, and therefore,

it is important to have a good understanding of the characteristics [50]. In a study of ^{56}Fe, the upbend was found to be predominantly dipole in nature [51], and while it is not clear if the upbend is electric or magnetic, it has been shown to have a bias towards a magnetic character [52], and the nuclear shell model also predicts a magnetic character [53].

Like the NLD, it would be best to use microscopic models of the γSF to determine information about the finer details of the γSF and to be able to predict the shape of the γSF for many nuclei, particularly those far from stability. While there has been much research dedicated to microscopic modeling of the γSF, two publications in particular have reported the results of large-scale calculations of γSF parameters. One of the publications used the the quasi-particle random-phase approximation (QRPA) model incorporated into Hartree-Fock models [54] and the other used the QRPA model incorporated into Hartree-Fock-Bogoliubov [55] models.

1.5 Indirect techniques for constraining (n,γ) cross sections

The majority of the uncertainty in Hauser-Feshbach calculations of neutron-capture cross sections comes from the unreliability of the nuclear level density and γ-ray strength function models described above. To reduce the uncertainty of these calculations, the nuclear properties needed for neutron-capture cross section calculations need to be constrained based on experimental data. Since neutron-capture reactions on nuclei far from stability are unable to be measured directly at this time, indirect methods have been developed. Four of the major indirect techniques being used today are: the surrogate method [56], the γ-ray strength function method [57, 58], the Oslo method [59–62], and the β-Oslo method [63].

The surrogate method utilizes charged particle reactions to populate the compound nucleus that would be formed in the neutron-capture reaction of interest. The surrogate reactions can be performed with both traditional stable-beam experiments, or in inverse kinematics experiments. In normal kinematics, the targets available for measurement are restricted to those that are stable or near stability. In inverse kinematics, though, the major limitation is the ability of current facilities to deliver radioactive beams with a sufficient rate for the measurement of interest. A recent validation of the surrogate method, in inverse kinematics, for constraining neutron-capture cross sections cites a beam rate of at least 10^4 particles per second is needed for successful measurements [64]. The γ-ray strength function method utilizes photodisintigration reactions (γ, n) to study the γ-ray strength function of the compound nucleus of interest. The goal is to infer the cross section of the inverse (n, γ) reaction. As with other measurements, the γ-ray strength function method is also limited by the stability of the target needed for the reaction being studied. The Oslo method also utilizes charged particle reactions to study the compound nucleus of the neutron-capture reaction of interest, and is therefore also restricted by the stability of the targets needed. It has been used extensively for nuclei along the valley of stability to extract nuclear level densities and γ-ray strength functions, and has been shown to reliably reproduce known cross sections of neutron-capture reactions. A method based on the Oslo method, the β-Oslo method, has recently been developed. Instead of charged particle reactions, the β-Oslo method utilizes β decay to populate the compound nucleus, which gives it the advantage of being applicable to neutron-rich nuclei that are further from the valley of stability. As the subject of this work, the β-Oslo method will be covered in more detail in Chapter 3.

1.6 Current status of β-Oslo validation

While the traditional Oslo method has been validated extensively [65–67], the β-Oslo method has not been validated as extensively. To date, there is only one comparison of an (n,γ) cross section constrained via the β-Oslo method to one determined through a direct measurement [68]. The cross section of ^{50}Ti$(n,\gamma)^{51}$Ti was constrained by both the β-Oslo method (via the measurement of ^{51}Sc$\rightarrow^{51}$Ti) and the Oslo method (via the measurement of ^{50}Ti$(d,p)^{51}$Ti), and these results were then compared to existing data of a direct measurement of ^{50}Ti$(n,\gamma)^{51}$Ti, as shown in Figure 1.5. All three cross sections were found to be in good agreement, and it was concluded that the β-Oslo method is indeed a valid method for constraining neutron-capture cross sections. However, since ^{50}Ti is a lighter mass nucleus, it has a lower level density, and it cannot be assumed that neutron capture on ^{50}Ti proceeds through a compound system. Therefore, a validation needs to be performed in a heavier mass region, with a nucleus that has a higher level density and is, in principle, a more statistical system.

1.7 Dissertation Outline

In this dissertation, the process of validating the β-Oslo method in a high mass region is detailed. Chapter 2 covers the details of the β-decay experiment performed at the National Superconducting Cyclotron Laboratory and the steps of the data analysis to isolate the β decay of ^{83}As. Chapter 3 provides the details of the β-Oslo method, along with the results of the β-Oslo method applied to the β decay of ^{83}As, to constrain the cross section of ^{82}Se$(n,\gamma)^{83}$Se. Chapter 4 covers the experimental details of a direct measure of ^{82}Se$(n,\gamma)^{83}$Se performed at Los Alamos National Laboratory, along with the subsequent

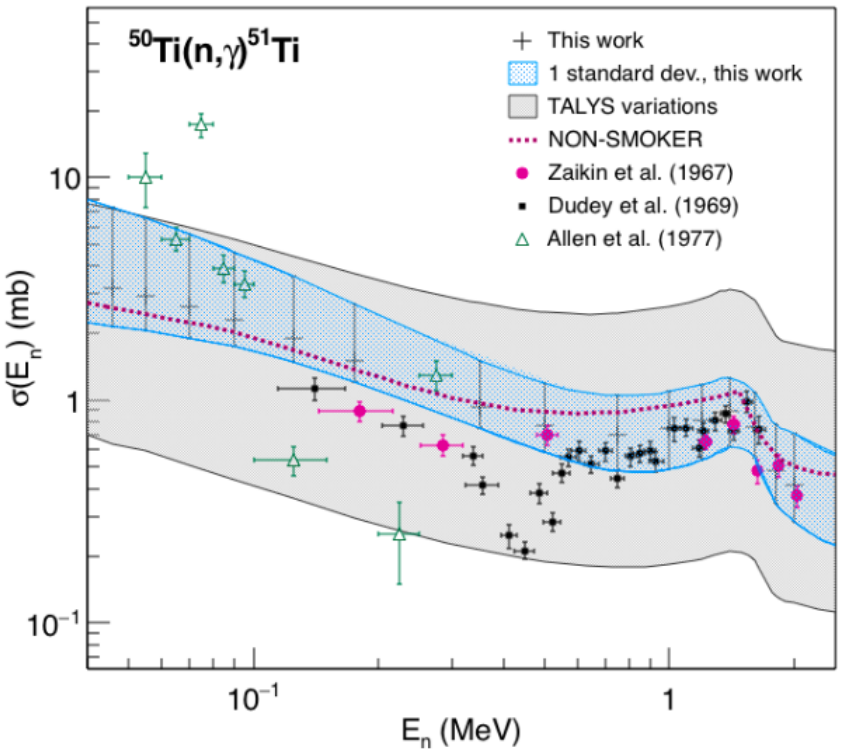

Figure 1.5: Comparison of the ^{50}Ti$(n,\gamma)^{51}$Ti cross section constrained using the β-Oslo and Oslo methods (grey crosses) to experimentally determined cross sections (points). Reprinted figure with permission from [68] Copyright 2019 by the American Physical Society.

data analysis. Chapter 5 shows a comparison of the directly measure neutron-capture cross section to the cross section obtain via the β-Oslo method, and provides a final conclusion and an outlook of future work.

Chapter 2

Study of ^{83}As β decay at the NSCL

2.1 Experimental Setup

An experiment measuring the β decay of ^{83}As was performed at the National Superconducting Cyclotron Laboratory (NSCL) at Michigan State University in East Lansing, Michigan. A primary beam of ^{86}Kr at 140 MeV/μ was produced by the Coupled Cyclotron Facility (CCF) and impinged on a 188 mg/cm^2 ^{9}Be target, producing a cocktail beam with multiple fragments. A schematic of the front end of the CCF is shown in Fig. 2.1. The fragments were separated in the A1900 fragment separator [69, 70] with a 0.5% momentum acceptance, producing a beam centered on ^{83}As that was delivered to the end station in the S2 vault. At the end station, ions were implanted in a Si double sided strip detector (DSSD) located in the center of the Summing NaI (SuN) detector [71], used to detect β-delayed γ rays. In order to veto light ions, which could increase the background, a Si surface detector was placed behind the DSSD. Ions were identified on an event-by-event basis based on a measurement of energy loss in two Si PIN detectors placed upstream of SuN, and the time-of-flight (TOF) measured between a thin scintillator at the focal plane of the A1900 and one of the PIN detectors. A picture of the end station setup is shown in Fig. 2.2.

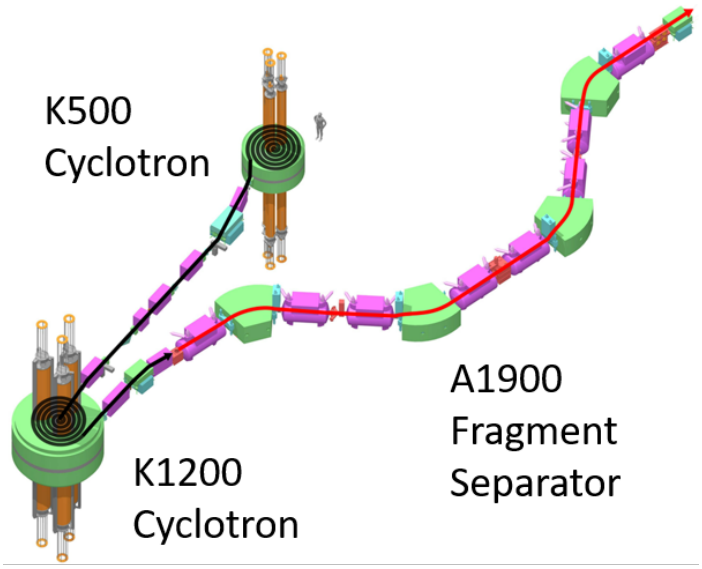

Figure 2.1: A representation of the layout of the CCF (comprised of the K500 and K1200 cyclotrons) and the A1900 Fragment Separator.

Figure 2.2: A picture of the e14505 setup in the S2 vault. SuN is shown on the right in the large blue box, the DSSD and veto and located in the center of SuN (indicated by the purple box), and the PIN detectors are located upstream of SuN in the red box.

2.1.1 The Summing NaI (SuN) detector

SuN is a total absorption spectrometer (TAS), which employs the γ-summing technique [71].

A cylindrical NaI(Tl) scintillator detector, SuN is 16 inches long and 16 inches in diameter

with a 1.8 inch borehole down the center. The SuN detector is depicted in Fig. 2.3. SuN has eight optically-isolated segments of NaI (separated by aluminum), which are each read out by three photomultiplier tubes (PMTs). The signals from each of the PMTs in a segment are added together to obtain the total signal observed in that segment. The total signal from all of the segments are then summed in order to obtain a summed γ-ray spectrum. SuN has a high efficiency for detecting γ rays (85(2)% for the 662 keV transition from the decay of ^{137}Cs) and has nearly 4π coverage.

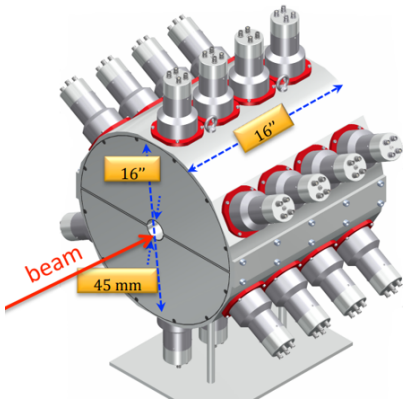

Figure 2.3: A schematic of the SuN detector.

There are several methods through which γ rays can interact with the NaI crystals of SuN. The three main interactions are photoelectric absorption, Compton scattering, and pair production. For low energy γ rays (< 1 MeV) the dominant interaction is photoelectric absorption, in which the γ ray is absorbed by an atom. The absorbing atom will then emit a photoelectron. The interaction of the photoelectron with the NaI will then create scintillation light that will be detected by the PMTs. The process of Compton scattering takes place when an incident γ ray interacts with an electron in the detector material. A portion of the energy of the γ ray is transferred to the electron (called the recoil electron), leading to a detection of only the energy transferred to the electron. Compton scattering is the most likely process for mid-energy γ rays. Pair production is a possible process for γ rays

above 1.022 MeV, but will most likely happen above 5 MeV. Pair production is the creation of a electron-positron pair through the interaction of the incident γ ray with the Coulomb field of the nucleus. The positron will annihilate, producing two characteristic 511-keV γ rays. One or both of these γ rays have the possibility of interacting with SuN.

The γ-summing technique is used to determine the excitation energy of a nucleus after β decay. While SuN can be used in order to obtain the energy of the individual γ rays being emitted in a cascade, the signals from all eight segments can be summed to obtain the full energy deposited from all γ rays in a cascade, which corresponds to energy of the excited state(s) populated through β decay. It is worth noting that there is the chance for multiple γ rays depositing in a single crystal, leading to additional peaks that could appear in the single segment spectrum. It is also possible for some γ rays to escape the volume of the detector, leading to an incomplete recorded energy, which would appear in the spectrum as peaks below the energy of the excited state fed through β decay.

The γ-summing technique can be illustrated with an example of ^{60}Co, as shown in Figure 2.4. The β decay of ^{60}Co populates a 2505-keV state in ^{60}Ni, which then decays through two characteristic γ rays (1173 keV and 1332 keV). The γ ray energy spectrum from a single segment of SuN, shown in panel (a) of Figure 2.4, would exhibit two peaks attributed to the full energy of the 1173- and 1332-keV γ-ray transitions in ^{60}Ni. There would also be a small peak at 2505 keV corresponding to the summed energy of the 1173- and 1332-keV γ rays, from instances where both γ rays are simultaneously deposited in the single segment. The spectrum of the top half of SuN is shown in panel (b), where again there are two peaks corresponding to the two γ rays transitions in ^{60}Ni, as well as a larger peak at 2505 keV (relative to the spectrum of a single segment) since the chance of both γ rays depositing in the segments comprising the top half of SuN is higher than the chance of both depositing

in only a single segment. The spectrum from the total summation of the signal from all segments (panel (c) of Figure 2.4) shows a "sum peak" at 2505 keV, corresponding to the 2505 keV state populated in the β decay of ^{60}Co.

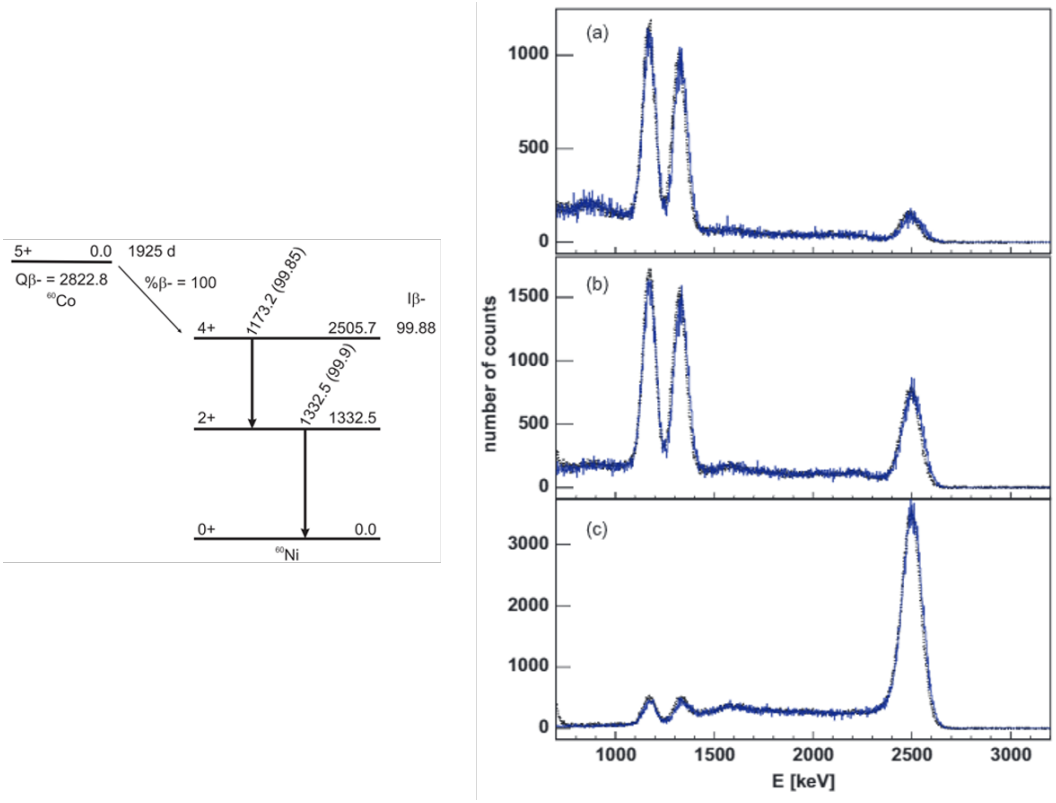

Figure 2.4: An example of TAS for ^{60}Co. On the left is the decay scheme of ^{60}Co. On the right is a figure from [71], showing the ^{60}Co gamma spectra obtained with (a) a single segment of SuN, (b) the top half of SuN, and (c) the total summation of all segments. Reprinted from [71], with permission from Elsevier.

SuN's PMTs were gain matched using the 1460.8 keV γ ray from ^{40}K, which is naturally occurring and can be observed in background data. The first step in gain matching is adjusting the high voltage applied to the PMTs, such that the ^{40}K peak appears in approximately the same channel for each PMT. The second step involves the application of a multiplication factor applied in software to precisely center the centroid of the ^{40}K peak in the same channel number for each PMT. The voltages and multiplication factors are listed in Table 2.1. After being gain matched, the energy spectrum of each of the three PMTs of

a segment can be summed together in software to determine the segment signal. All eight segments were then calibrated with a linear energy calibration using a ^{60}Co source and a ^{137}Cs source. The parameters determined from the linear calibration are shown in Table 2.2.

Table 2.1: Voltage applied to each PMT and scaling factors used for gain matching for SuN.

PMT Number	Voltage (+V)	Gain Matching Factor	PMT Number	Voltage (+V)	Gain Matching Factor
0	730	1.0920	12	835	1.0866
1	740	1.0000	13	820	1.0000
2	780	1.1099	14	821	1.0995
3	774	1.1302	15	831	1.0959
4	771	1.0000	16	865	1.0000
5	764	1.1195	17	824	1.1033
6	794	1.1148	18	889	1.1467
7	803	1.0000	19	853	1.0000
8	812	1.1316	20	831	1.1131
9	838	1.0949	21	909	1.0796
10	824	1.0000	22	930	1.0000
11	848	1.0993	23	892	1.1026

2.1.2 Double-sided silicon strip detector

The beam, centered on ^{83}As, delivered to the experimental end station was implanted into a 2.54 x 2.54 cm^2 and 1 mm thick double sided silicon detector (DSSD) located in the center of the borehole of SuN. The DSSD consists of 16 electrically-segmented strips on the front,

Table 2.2: Scale factor and intercept used for the calibration of SuN's segments.

Segment Number	Calibration Scale	Calibration Intercept
0	0.4193	-16.02
1	0.4195	-15.95
2	0.4113	-14.95
3	0.4260	-16.50
4	0.4191	-16.41
5	0.4216	-17.93
6	0.4046	-16.20
7	0.4172	- 14.74

and another set of 16 perpendicular strips on the back. These strips provide the ability to define pixels in software. A pixel is defined as the intersection of a front strip and a back strip. Together, these pixels create a grid-like pattern that allows for the determination of the location of events. When an event occurs, the location is defined by the pixel with the highest deposited energy recorded. A picture of the DSSD is shown in Figure 2.5. Two gain ranges were used to capture the full energy of ion implantations (on the order of 1000s of MeV) and the energy loss of the β-decay electrons (keV to MeV range). Both gain ranges needed to be adjusted to ensure that all front and back strips have the same response. The low gain, used for detecting ion implantations, is gain matched by applying a multiplication factor in software to shift the centroid of the maximum energy peak of implanted ions of each strip so the peak was centered in the same channel for all front or back strips. The low gain matched energy spectrum of both the front strips and the back strips is shown in Figure 2.6. The high gain, used for detecting β-decay electrons, was gain matched using the most intense alpha peak from a ^{228}Th source. Similarly to the low gain, a multiplication

factor was applied in software to shift the centroid of the peak in each DSSD strip so that it was centered in the same channel for all strips. The high gain matched energy spectrum of both the front and back strips is shown in Figure 2.7. All scaling factors used for both the high gain and low gain matching are given in Table 2.3.

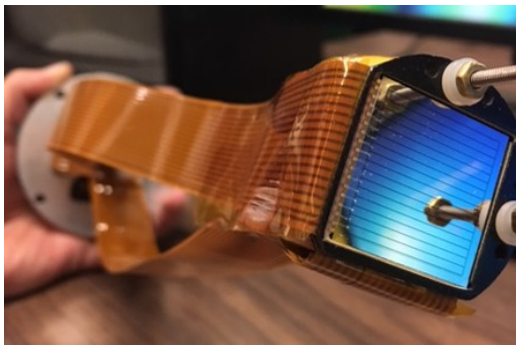

Figure 2.5: A picture of the DSSD used for experiment e14505.

2.2 Isolation of ^{83}As β decay

Ions of ^{83}As, ^{84}Se and ^{85}Se were delivered to the experimental end station. These three isotopes are labeled in the particle identification (PID) plot, which is a plot of particle time-of-flight versus energy loss as described in Section 2.1, shown in Figure 2.8. Conventionally, the β decay of the isotope of interest would be identified by correlating to implanted ions, which are identified via the PID. In software, a correlation timing window is defined. Once a decay is observed, the correlation is performed by opening the timing window and looking backwards in time to identify an ion that arrived within the specified timing window. The correlated ion must also have arrived in the same DSSD pixel the β decay is observed in. The correlation timing window is generally chosen based on the half-life of the isotope of interest, and needs to be long enough that the decay will be seen, but not too long that there is a chance for another ion to be implanted in the same time window. In the present

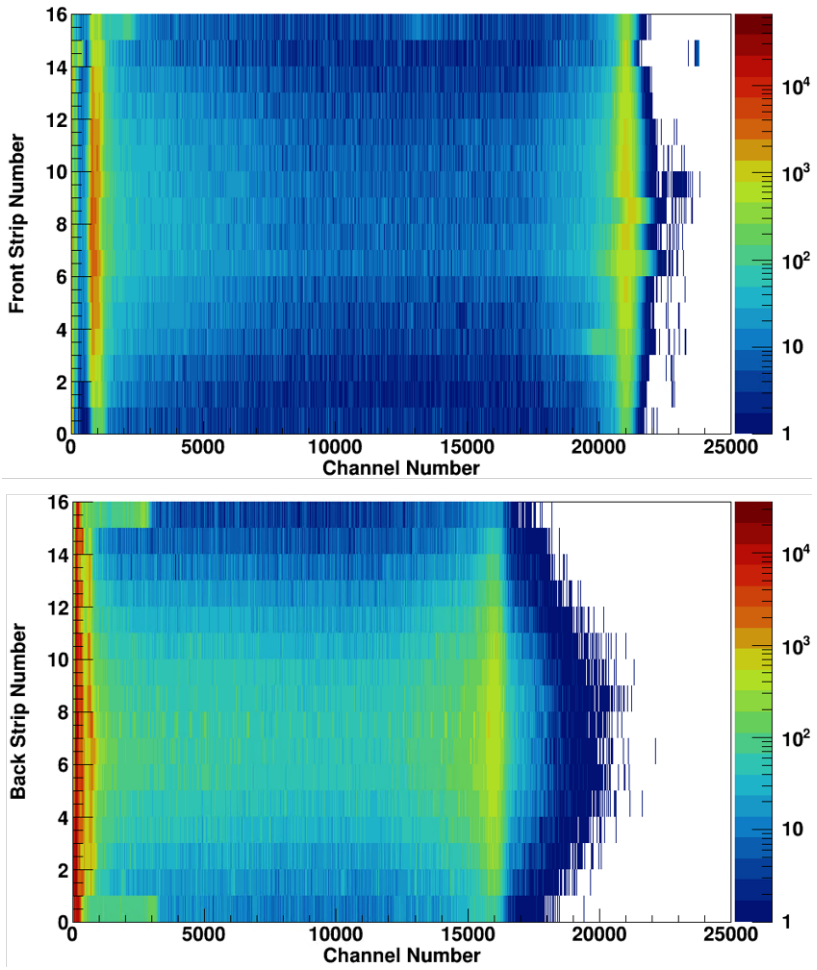

Figure 2.6: Gain matched energy spectra for the DSSD low gain setting. The front (top) and back (bottom) strip numbers are shown as a function of channel number.

experiment, the implanted isotopes and their decay products have half-lives on the order of seconds to hours (summarized in Table 2.4), which would require long correlation time windows. Along with a high implantation rate, the preferred method of correlation would be too difficult to successfully identify the decay of ^{83}As. Due to this, another method of isolating the β decay of ^{83}As needed to be used.

The beam delivered to the experimental end station was pulsed in an eight minutes on, eight minutes off cycle for seven hours, after which the beam was turned off for eight hours. The pulsed setting was chosen based on the half-lives of the species involved, to obtain a

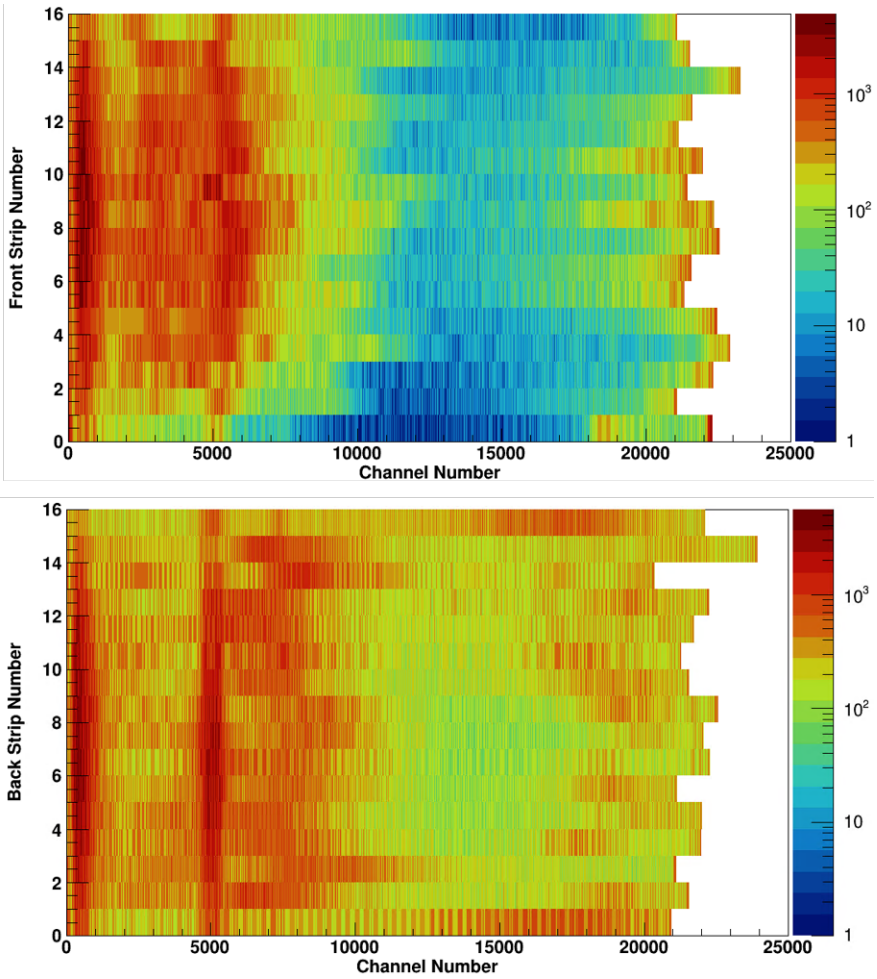

Figure 2.7: Gain matched energy spectra for the DSSD hi gain setting, using a ^{228}Th source. The front (top) and back (bottom) strip numbers are shown as a function of channel number.

cleaner spectrum associated with the decay of individual isotopes. Shown in Figure 2.9 is the total absorption (or summed) spectra corresponding to the decay of all isotopes and their daughters and granddaughters as a function of time. There are several strongly populated states in the decay of some of the isotopes that appear here as the horizontal bands. Longer lived isotopes can be identified based on the bands extending into the long beam-off period starting around 25000 seconds. The projection of any excitation energy region onto the x-axis would yield the decay profile of that excitation energy which may have a contribution from multiple decaying species.

Table 2.3: Scaling factors used for gain matching the front and back strips of the DSSD.

Front Strip Number	Low Gain Matching Factor	High Gain Matching Factor	Back Strip Number	Low Gain Matching Factor	High Gain Matching Factor
0	0.990	0.680	0	0.978	0.639
1	1.075	0.643	1	0.939	0.657
2	0.998	0.681	2	0.935	0.644
3	1.130	0.698	3	0.953	0.670
4	1.027	0.685	4	0.965	0.671
5	1.004	0.650	5	1.036	0.645
6	1.203	0.658	6	0.974	0.680
7	0.973	0.687	7	0.914	0.673
8	0.973	0.682	8	0.953	0.688
9	0.998	0.654	9	1.005	0.657
10	0.995	0.669	10	0.949	0.649
11	1.042	0.644	11	0.995	0.663
12	0.990	0.658	12	1.010	0.678
13	1.036	0.710	13	0.950	0.621
14	0.726	0.656	14	0.974	0.729
15	1.054	0.642	15	0.939	0.674

Using the half-lives and implantation rates of all present species (shown as a function of time for ^{83}As and ^{84}Se in Figure 2.10), their individual contributions to this total decay profile were modeled using the Bateman equations, which describe the growth and decay of activities of a decay chain [72]. The contribution of ^{85}Se to the total decay profile was determined to be on the order of 1%, and is therefore ignored in the subsequent analysis. The general solution of the Bateman equations for a decay chain $Q_1 \rightarrow Q_2 \rightarrow Q_3 \rightarrow ... \rightarrow$

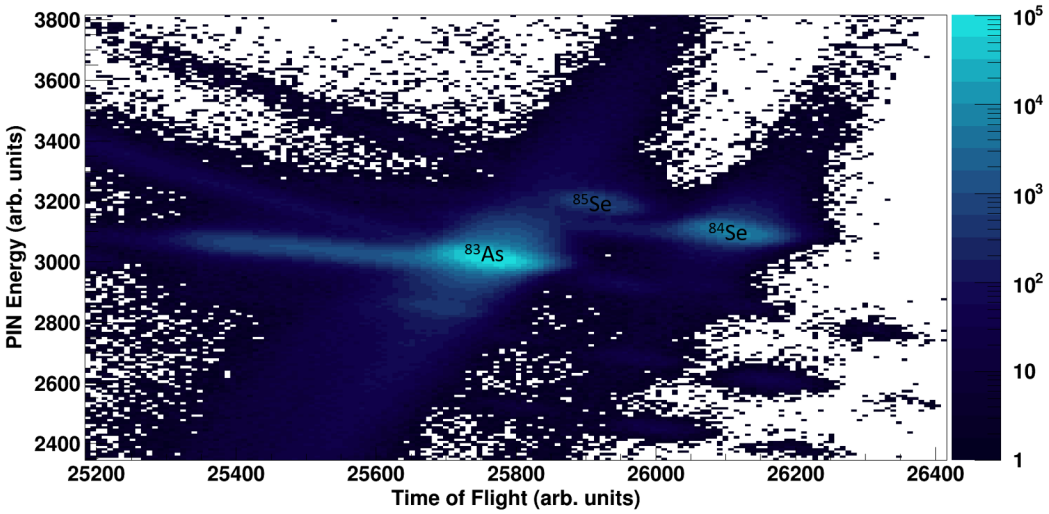

Figure 2.8: Particle Identification plot. PIN Energy is from the first PIN detector located upstream of SuN. TOF is determined from the timing between the PIN detector and the focal plane scintillator located in the A1900 fragment separator.

Table 2.4: Half-lives of implanted isotopes and their decay products.

Parent	$t_{1/2}$	Daughter	$t_{1/2}$	Granddaughter	$t_{1/2}$
^{83}As	13.4 s	^{83}Se	22.25 m, 70.1 s	^{83}Br	2.374 h
^{84}Se	3.26 m	^{84}Br	31.76 m	^{84}Kr	stable
^{85}Se	32.9 s	^{85}Br	2.90 m	^{85}Kr	4.480 h

Q_n, where there is also an external source of production, S_i, is shown in Equation 2.1.

$$Q_n(t) = \sum_{i=1}^{n} \left[\prod_{j=i}^{n-1} \lambda_{j,j+1} \times \sum_{j=i}^{n} \left(\frac{Q_i(0)e^{-\lambda_j t}}{\prod_{\substack{p=i \\ p\neq j}}^{n} (\lambda_p - \lambda_j)} + \frac{S_i(1-e^{-\lambda_j t})}{k_j \prod_{\substack{p=i \\ p\neq j}}^{n} (\lambda_p - \lambda_j)} \right) \right] \tag{2.1}$$

Here, Q_n is the number of atoms of a species present at time t, λ_n is the decay constant for species n, and $\lambda_{n,n+1}$ is the partial decay constant, which takes into account the branching ratio, as shown in Equation 2.2.

$$\lambda_{n,n+1} = BR_{n,n+1} \times \lambda_n \tag{2.2}$$

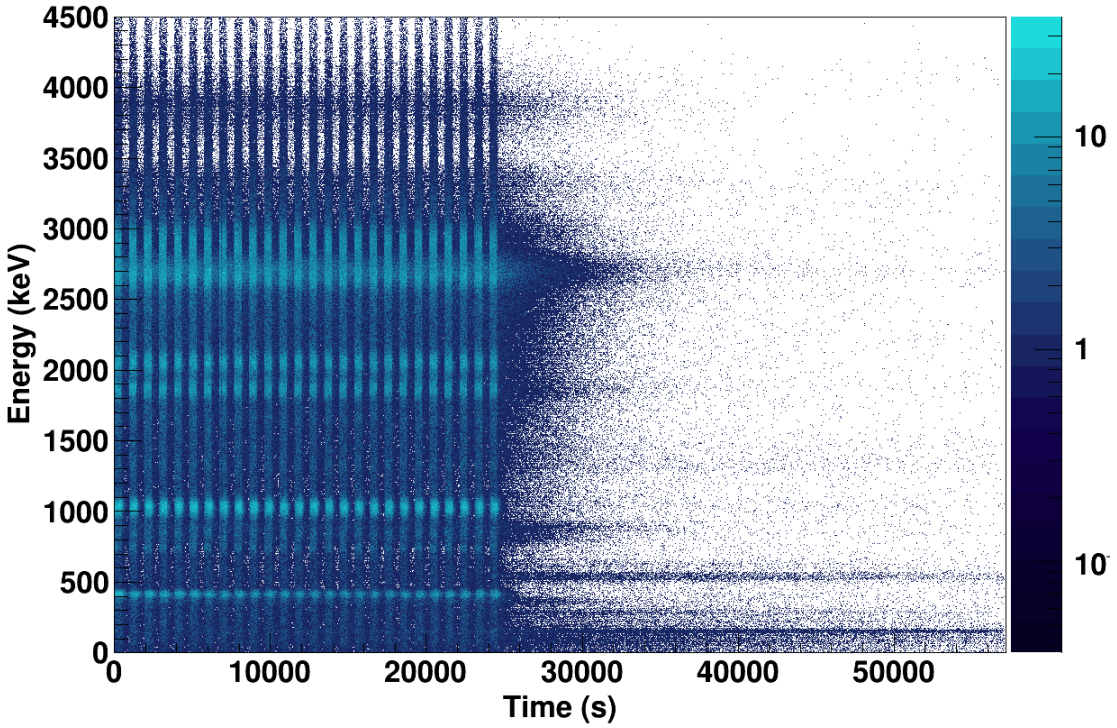

Figure 2.9: SuN total absorption spectrum as a function of time.

To ensure the activity profiles produced using the Bateman equations were accurate representations of the experimental data, energy cuts were taken for excitation energy peaks in the 2-dimensional spectrum, shown in Figure 2.9, that could be attributed to the decay of a single isotope or a decay chain. Each cut was projected onto the x-axis to obtain the decay profile associated with that isotope or decay chain. This was then compared to the decay profile produced using the Bateman equations. The first activity profile compared was one attributed to the 408.2 keV level in ^{84}Br, which is populated through the β decay of ^{84}Se and decays directly to the ground state. The decay scheme of ^{84}Br is shown in Figure 2.11. The Bateman equations for the mass 84 chain were scaled according to the efficiency of SuN (70% at 400 keV) and β-feeding values (100% for the 408.2-keV energy level). The calculated activity profile was overlaid on the activity profile produced by gating on the 408.2-keV peak

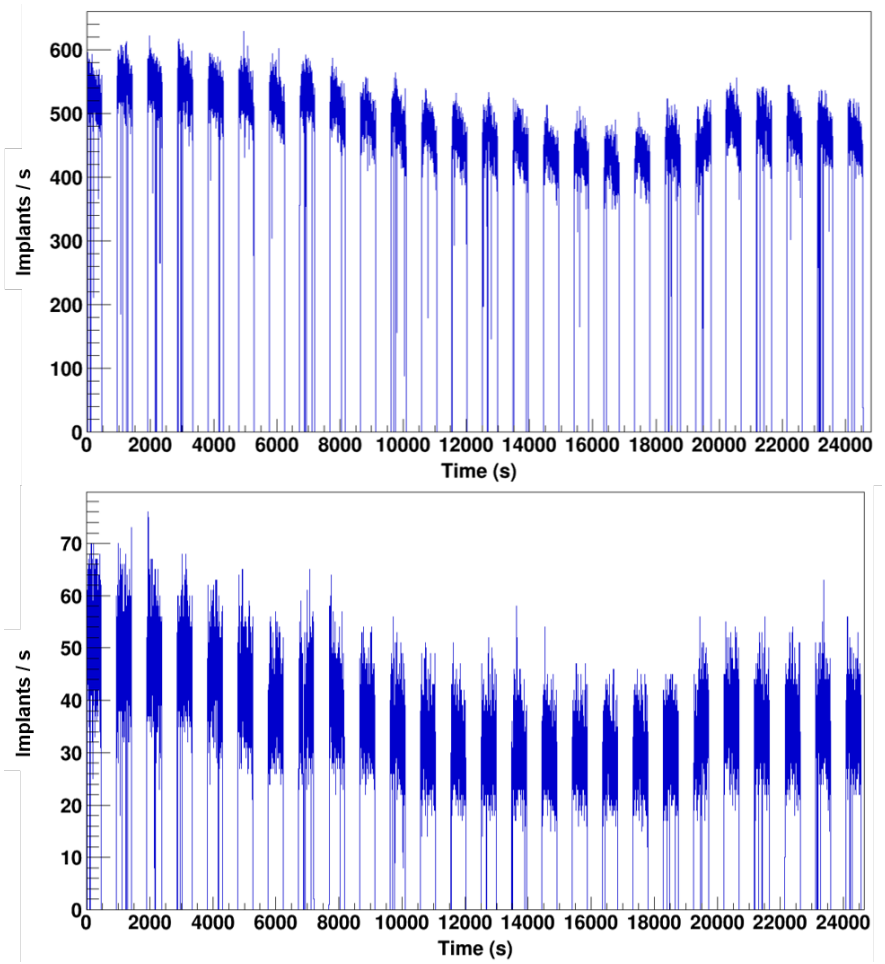

Figure 2.10: (Top) Implantation rate of ^{83}As ions in the DSSD. (Bottom) Implantation rate of ^{84}Se ions in the DSSD.

in the TAS as a function of time spectrum. The result is shown in the top panel of Fig. 2.12. The second activity profile reproduced was one attributed to two decays within the same decay chain. The peak at approximately 2050 keV in the excitation energy spectrum has contributions from the β decay of ^{83}As populating a 2076.84-keV level in ^{83}Se and the β decay of ^{83}Se populating a 2051.45-keV level in ^{83}Br. Due to the poor energy resolution of SuN, these levels could not be resolved. Both states de-excite via cascades of multiple γ rays to the ground state. The detector efficiency, β-feeding values, and relative γ-ray intensities (obtained from ENSDF [73]) of each cascade were used to scale the calculated decay profiles.

The calculated decay profiles were compared to the activity profile obtained by gating on the 2050-keV peak in the TAS as a function of time spectrum. The result is shown in the bottom panel of Fig. 2.12.

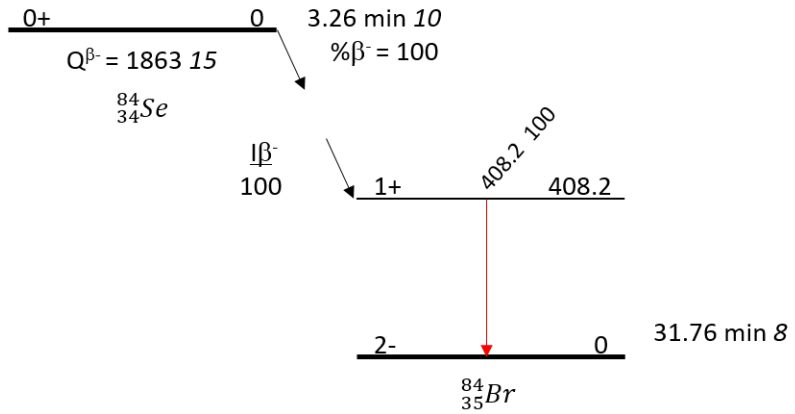

Figure 2.11: Complete level scheme of the decay of ^{84}Se into ^{84}Br from ENSDF. Absolute γ-ray intensities per 100 decays listed next to γ-ray energies. [73]

Once the calculated decay profiles were confirmed to represent the actual decay profiles, all decay profiles contributing to the total activity were calculated via the Bateman equations. All activities over the full time scale are shown in Fig. 2.13. Regions of the pulsed beam setting and the long decay period are shown in Figures 2.14 and 2.15, respectively. The decay profiles of individual isotopes were then used to identify time regions in which selected isotopes could be isolated in order to subtract them from the total activity profile. The subtractions are done with 2D matrices of the excitation energy (E_x) as a function of individual γ-ray energies (E_γ), since this is the starting point for the β-Oslo method (which will be discussed in the next chapter). The total E_x, E_γ matrix is shown in Figure 2.16.

From approximately 26000 seconds to the end of the run, the only activities expected to be present are from ^{83}Se $\rightarrow$ ^{83}Br and ^{83}Br $\rightarrow$ ^{83}Kr, as shown in Figure 2.15. The 2D E_x, E_γ matrix gated on this time region is shown in Fig. 2.17. Based on the results of the Bateman equations, there should be more ^{83}Br than ^{83}Se decay at later times. However, only 1.4%

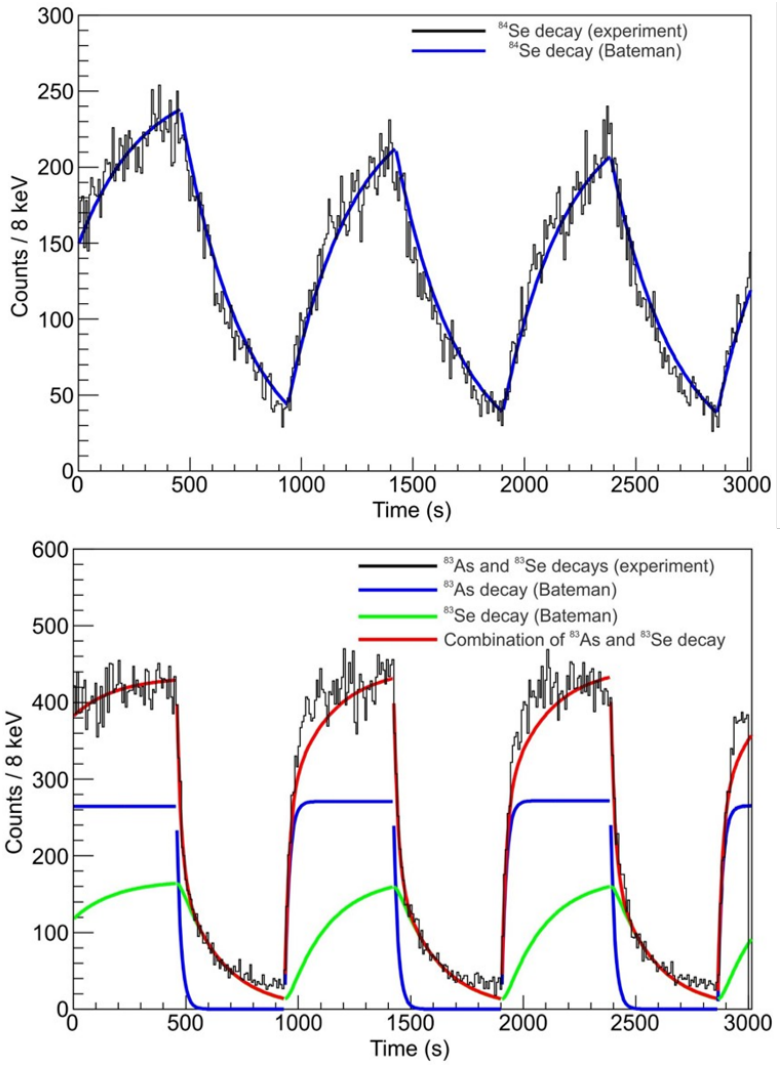

Figure 2.12: (Top) TAS spectrum as a function of time gated on the 408 keV peak corresponding to ^{84}Br (only first three beam cycles shown) with the decay profile modeled via the Bateman equations overlaid. (Bottom) TAS spectrum as a function of time gated on the 2053 keV peak that has contributions from the decay chain of ^{83}As $\rightarrow$ ^{83}Se $\rightarrow$ ^{83}Br (only first three beam cycles shown) with the decay profile of each decay, as well as the total, modeled via the Bateman equations overlaid.

of the β decays from ^{83}Br into ^{83}Kr populate observable excited states above the threshold of SuN (see level scheme in Fig. 2.18), leading to a 2D E_x, E_γ matrix that has comparable contributions from the decays of ^{83}Br and ^{83}Se. In order to independently isolate these two decays, the decay of ^{83}Br $\rightarrow$ ^{83}Kr was simulated in Geant4 and is shown in Figure 2.19. The

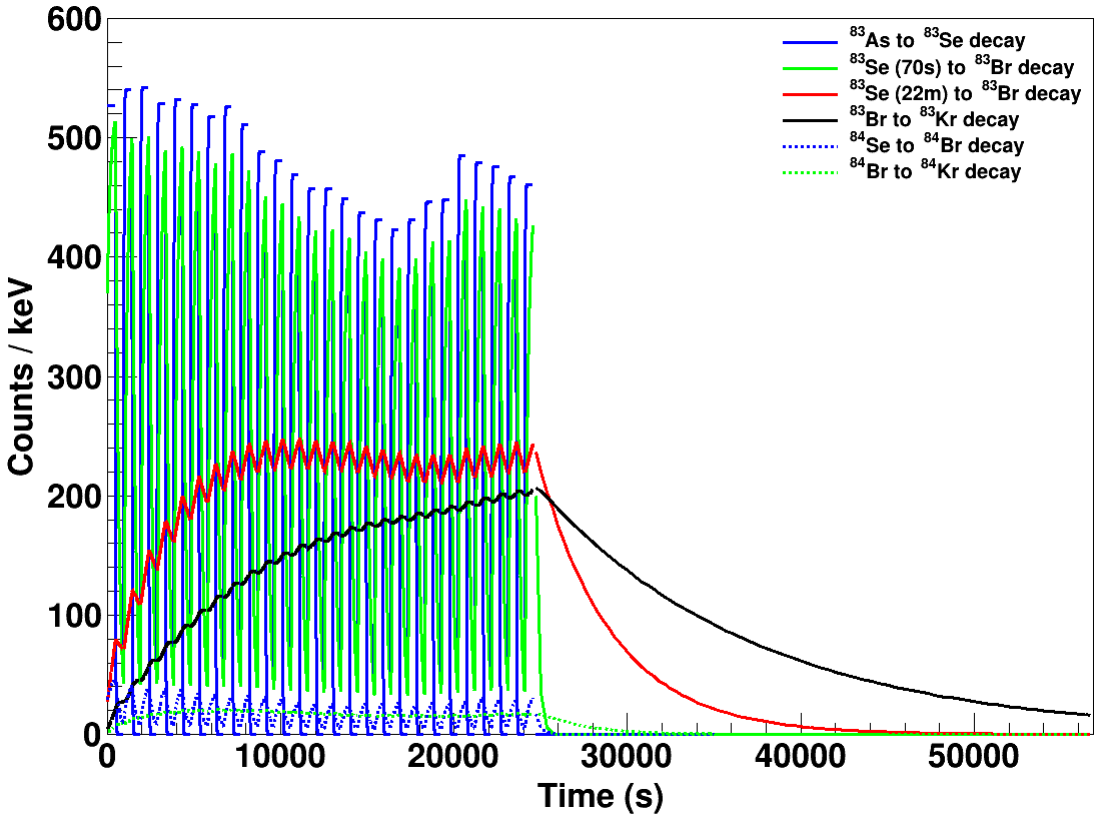

Figure 2.13: Activity profiles of all decaying species modeled with the Bateman equations, shown over the full time range.

number of decays simulated was determined by integrating the calculated activity profile from 26000 seconds to the end of the run.

The ^{83}Br $\rightarrow$ ^{83}Kr matrix was subtracted from the matrix shown in Fig. 2.17 to isolate a matrix of only ^{83}Se $\rightarrow$ ^{83}Br, shown in Fig. 2.20. A decay scheme of ^{83}Se $\rightarrow$ ^{83}Br with selected levels and γ-ray transitions is shown in Fig. 2.21. Here, the majority of the β feeding goes to a series of levels between 2600 and 2800 keV and eventually decays through cascades that have several lower energy, high intensity γ rays. This can be seen in the the E_x, E_γ matrix as well, providing confirmation that ^{83}Br was isolated. The simple decay of ^{84}Se $\rightarrow$ ^{84}Br (decay scheme shown in Fig. 2.11), consists of a single excited state fed in β decay that results in a single γ-ray transition to the ground state. The decay of ^{84}Se was

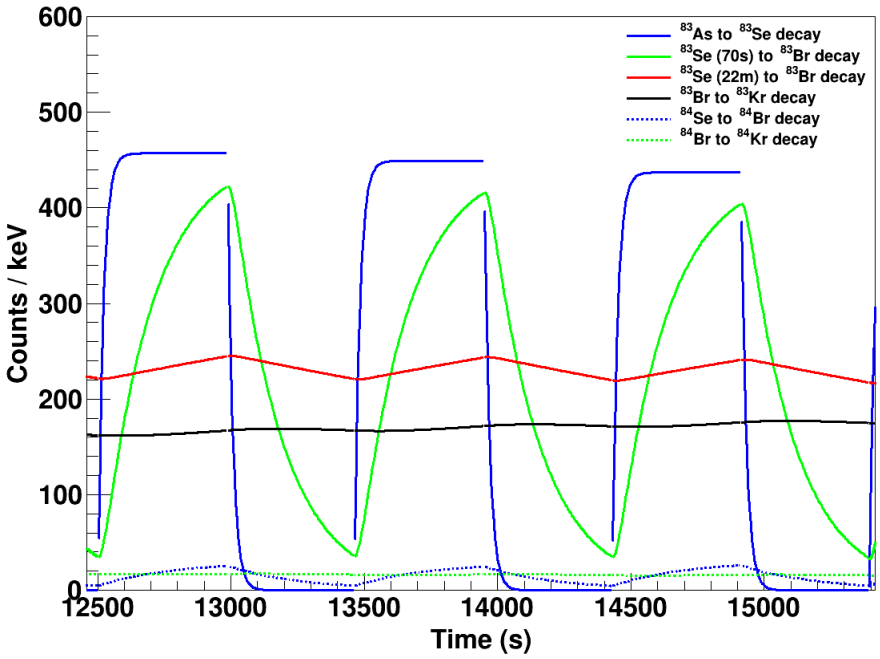

Figure 2.14: Regions of production and decay during the pulsed beam setting.

also simulated using Geant4. The resulting simulated E_x, E_γ matrix is shown in Fig. 2.22.

The two remaining decays, an isomeric state of ^{83}Se ($Q_{\beta-} = 3673(5)$ keV) decaying to ^{83}Br and the decay of ^{84}Br ($Q_{\beta-} = 4660(3)$ keV) to ^{84}Kr could not be independently isolated nor could they reliably be simulated, due to their larger $Q_{\beta-}$ values. After each beam on period, ^{83}As ($t_{1/2} = 13.4$ s) decayed away, and the E_x, E_γ spectrum from 102 seconds after the beginning of the beam off period to 19 seconds before the beginning of the next beam on cycle, was obtained. This time period included contributions from the decay of ^{83}Se, ^{83m}Se, ^{83}Br, ^{84}Se, and ^{84}Br, as can be seen in Figure 2.14. The isolated spectra of the decays of ^{83}Se, ^{83}Br, and ^{84}Se were all scaled and removed, leading to a 2D E_x, E_γ matrix with the decays of ^{83m}Se and ^{84}Br in a 9 to 1 ratio. This matrix is shown in Fig. 2.23. The decay schemes of ^{83m}Se $\rightarrow$ ^{83}Br and ^{84}Br $\rightarrow$ ^{84}Kr are shown in Figures 2.24 and 2.25. Many of the strongly fed levels and high intensity γ rays can be observed in the 2D matrix.

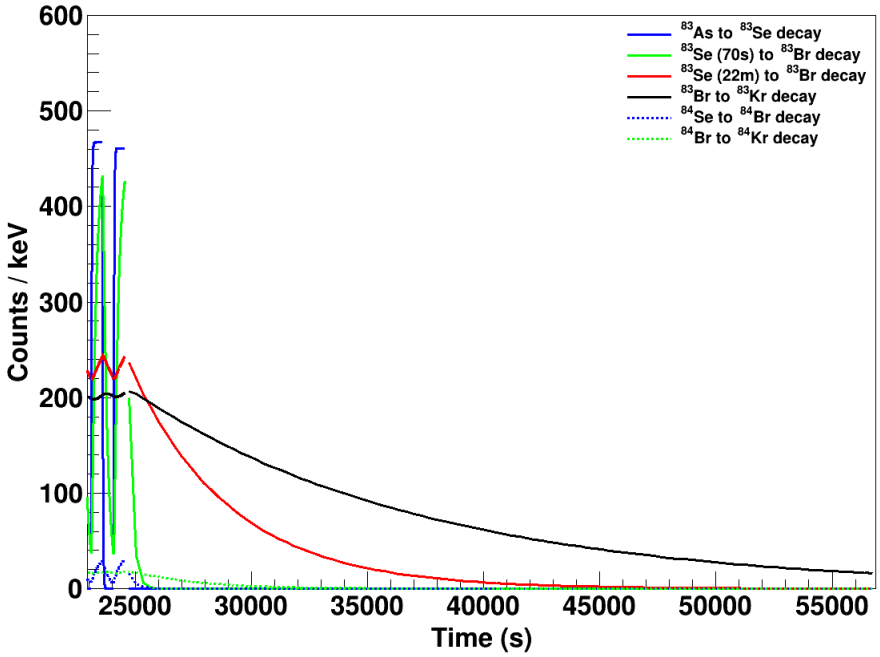

Figure 2.15: Plot of the long decay period during which the beam was not being delivered to the experimental end station.

Each of the isolated matrices were then scaled and subtracted from the portion of the beam-on periods with the same ratio of ^{83m}Se and ^{84}Br decays to obtain the final, isolated ^{83}As $\rightarrow$ ^{83}Se matrix, shown in Fig. 2.26. This 2D matrix is used as the starting point for the β-Oslo method, which will discussed in the following chapter. The spectra of γ-ray energy (E_γ) and excitation energy (E_x) measured in SuN for the β decay of ^{83}As to ^{83}Se (projections from the E_x, E_γ matrix) are shown in Figure 2.27. A decay scheme with select levels and transitions of ^{83}As $\rightarrow$ ^{83}Se is shown in Fig. 2.28. Both spectra are consistent with literature of known levels and γ-ray transitions of ^{83}Se. In the E_γ spectra, the strongest γ-ray transition with energy 734.9 keV is evident, as well as the second strongest transition with energy 1113.4 keV (I_γ = 36.1(11)% relative to the 734.9 keV transition [74]). While there are no β-feeding intensities reported in literature, a strongly fed level with energy

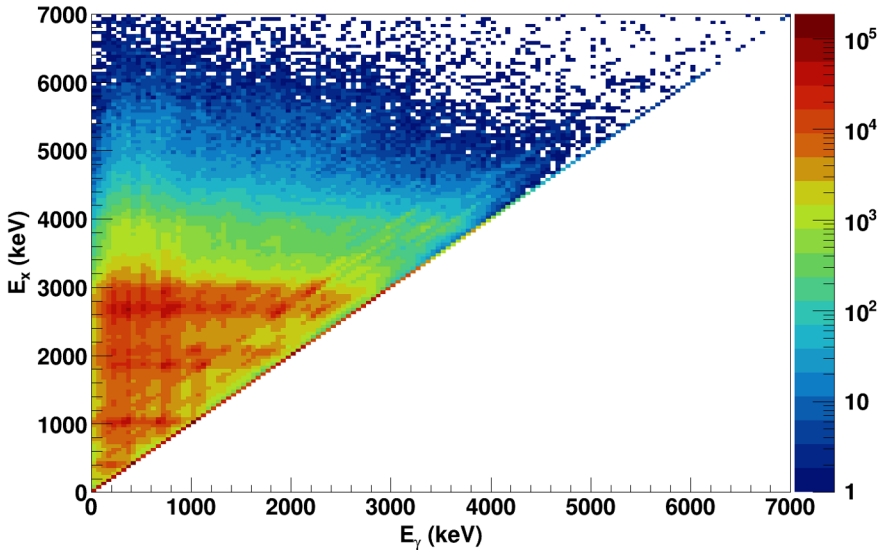

Figure 2.16: Excitation energy (E_x) as a function of γ-ray energy (E_γ), ungated, with all events.

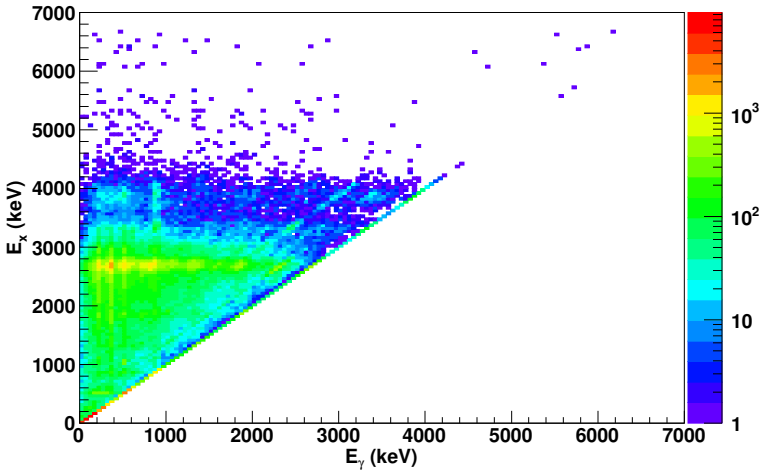

Figure 2.17: E_x, E_γ matrix with 50 keV binning, for a time gate of 26000 seconds to the end of the run.

1062.89(7) keV is clear, as well as strongly fed levels in the energy range of approximately 1800 - 2200 keV and 2500 - 3100 keV.

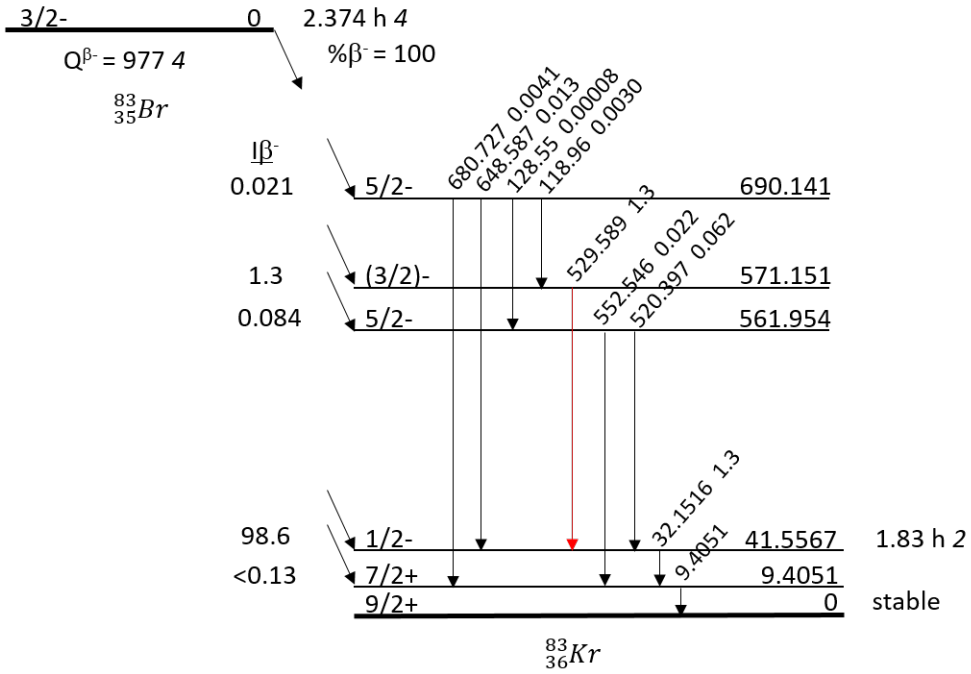

Figure 2.18: Decay scheme of ^{83}Br $\rightarrow$ ^{83}Kr. Absolute γ-ray intensities per 100 decays listed next to γ-ray energies. [74]

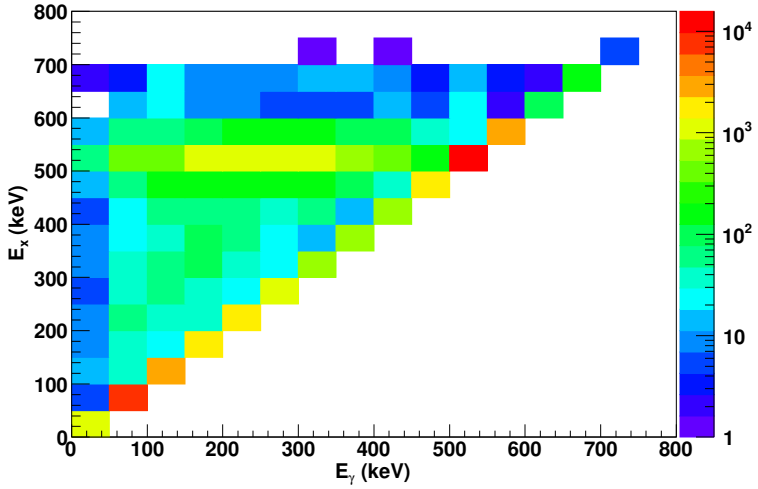

Figure 2.19: E$_x$, E$_\gamma$ matrix with 50 keV binning, for the decay of ^{83}Br $\rightarrow$ ^{83}Kr simulated in Geant4.

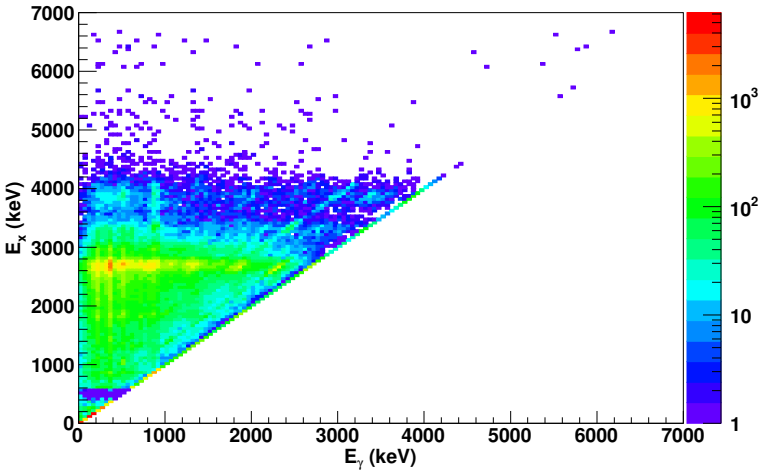

Figure 2.20: E_x, E_γ matrix with 50 keV binning, for the decay of ^{83}Se $\rightarrow$ ^{83}Br.

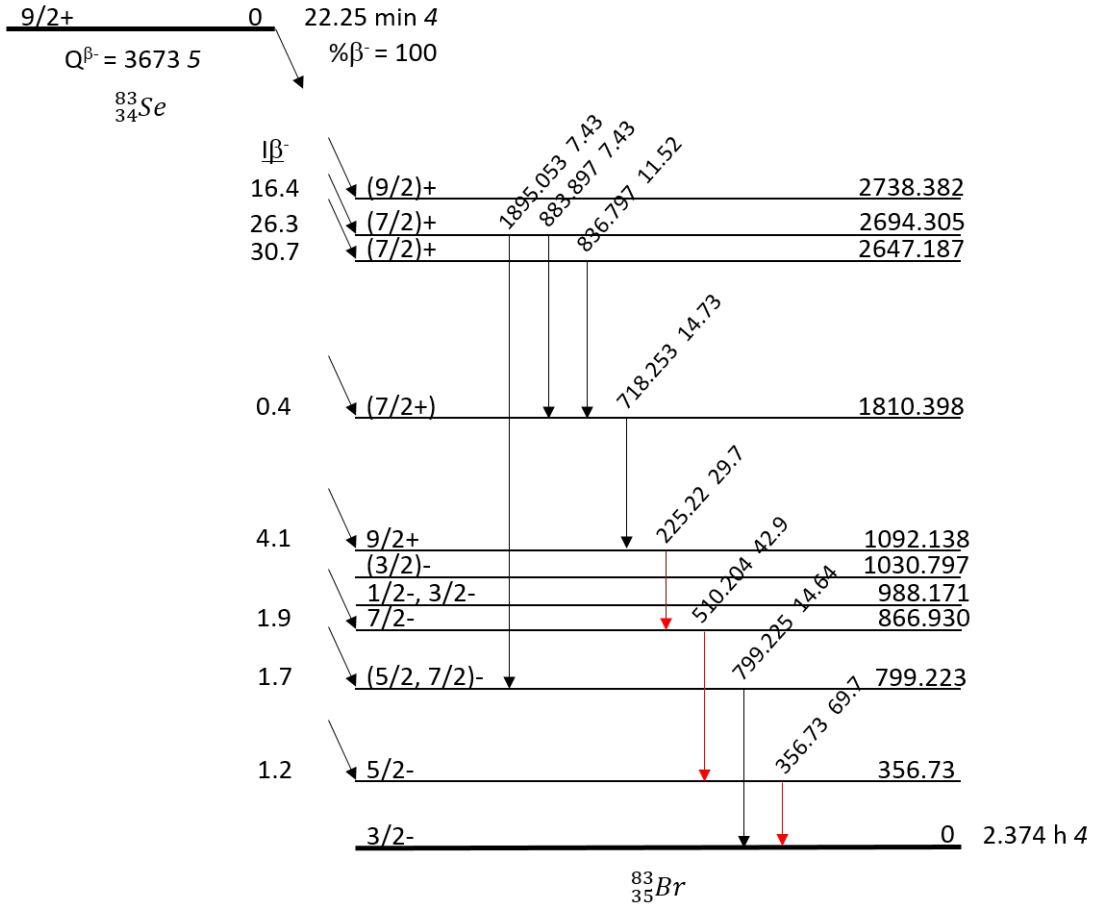

Figure 2.21: Decay scheme of ^{83}Se $\rightarrow$ ^{83}Br with selected levels and γ-ray transitions. Absolute γ-ray intensities per 100 decays listed next to γ-ray energies. [74]

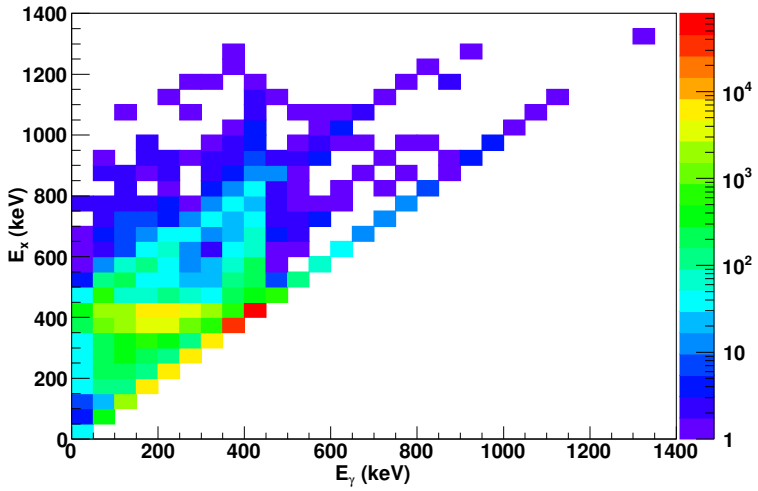

Figure 2.22: E_x, E_γ matrix with 50 keV binning, for the decay of ^{84}Se $\rightarrow$ ^{84}Br simulated in Geant4.

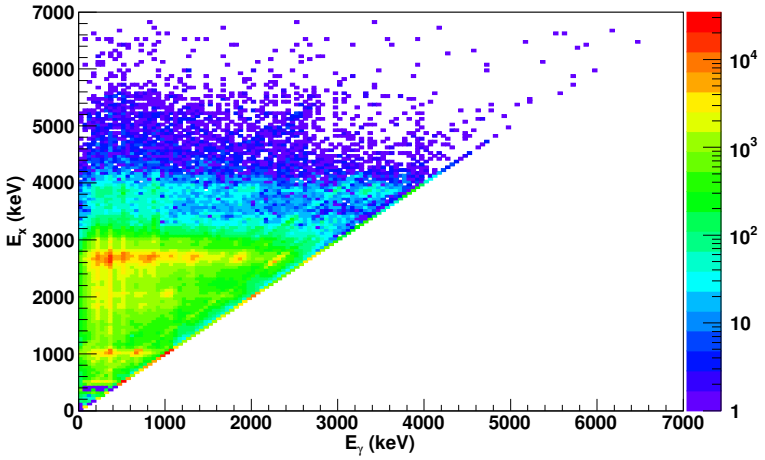

Figure 2.23: E_x, E_γ matrix with 50 keV binning, for the decays of the isomeric state of ^{83}Se $\rightarrow$ ^{83}Br and ^{84}Br $\rightarrow$ ^{84}Kr.

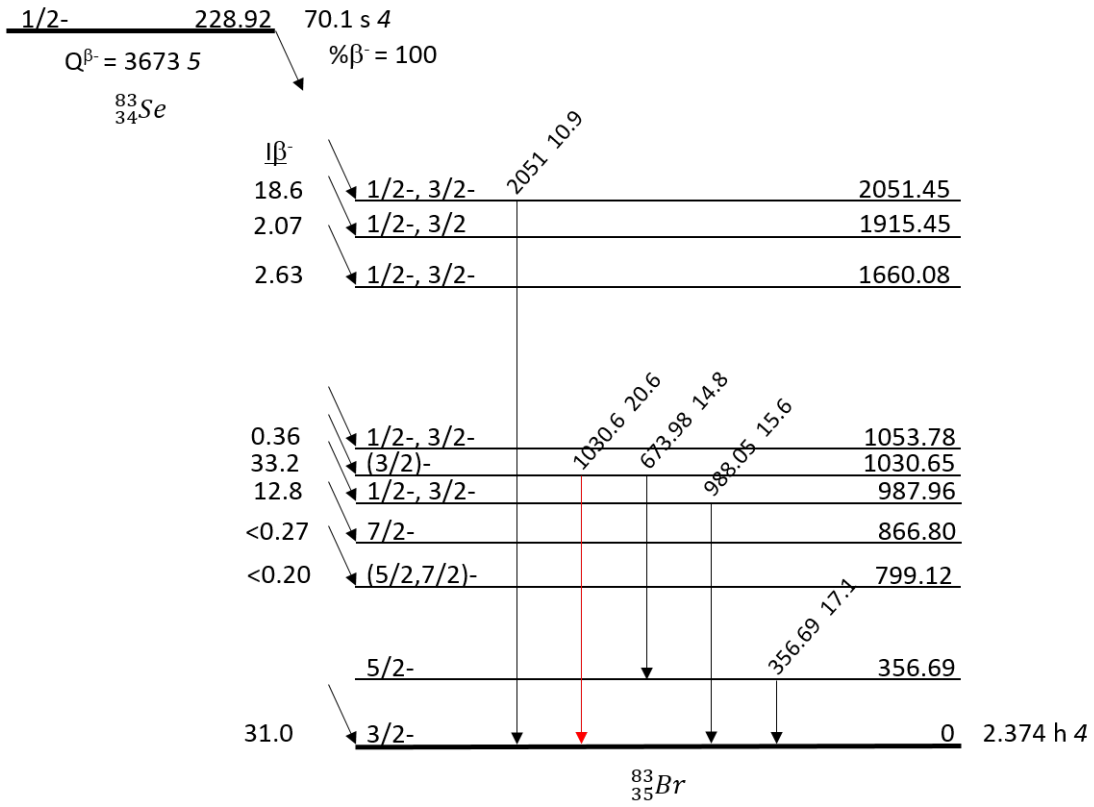

Figure 2.24: Decay scheme of the isomeric state of ^{83}Se $\rightarrow$ ^{83}Br with selected levels and γ-ray transitions. Absolute γ-ray intensities per 100 decays listed next to γ-ray energies. [74]

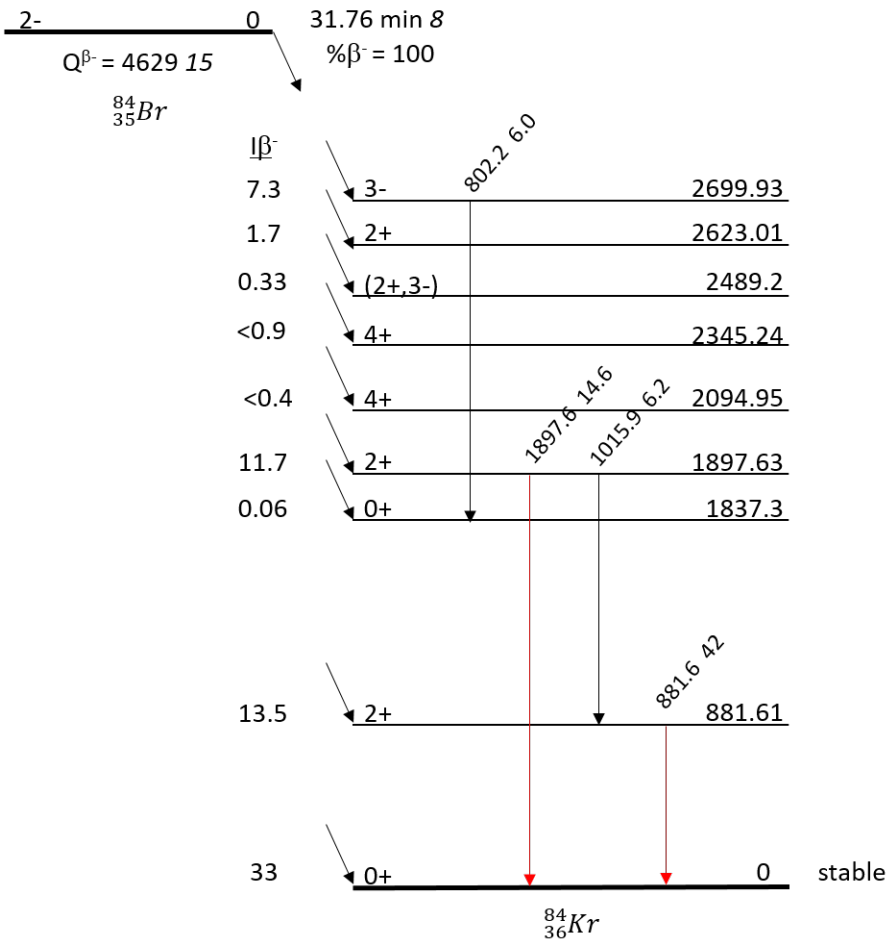

Figure 2.25: Decay scheme of ^{84}Br $\rightarrow$ ^{84}Kr with selected levels and γ-ray transitions. Absolute γ-ray intensities per 100 decays listed next to γ-ray energies. [73]

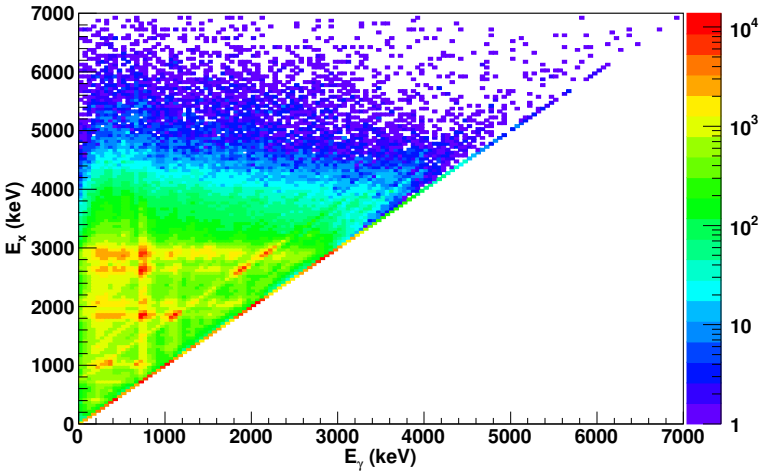

Figure 2.26: E$_x$, E$_\gamma$ matrix with 50 keV binning, for the decay of ^{83}As $\rightarrow$ ^{83}Se.

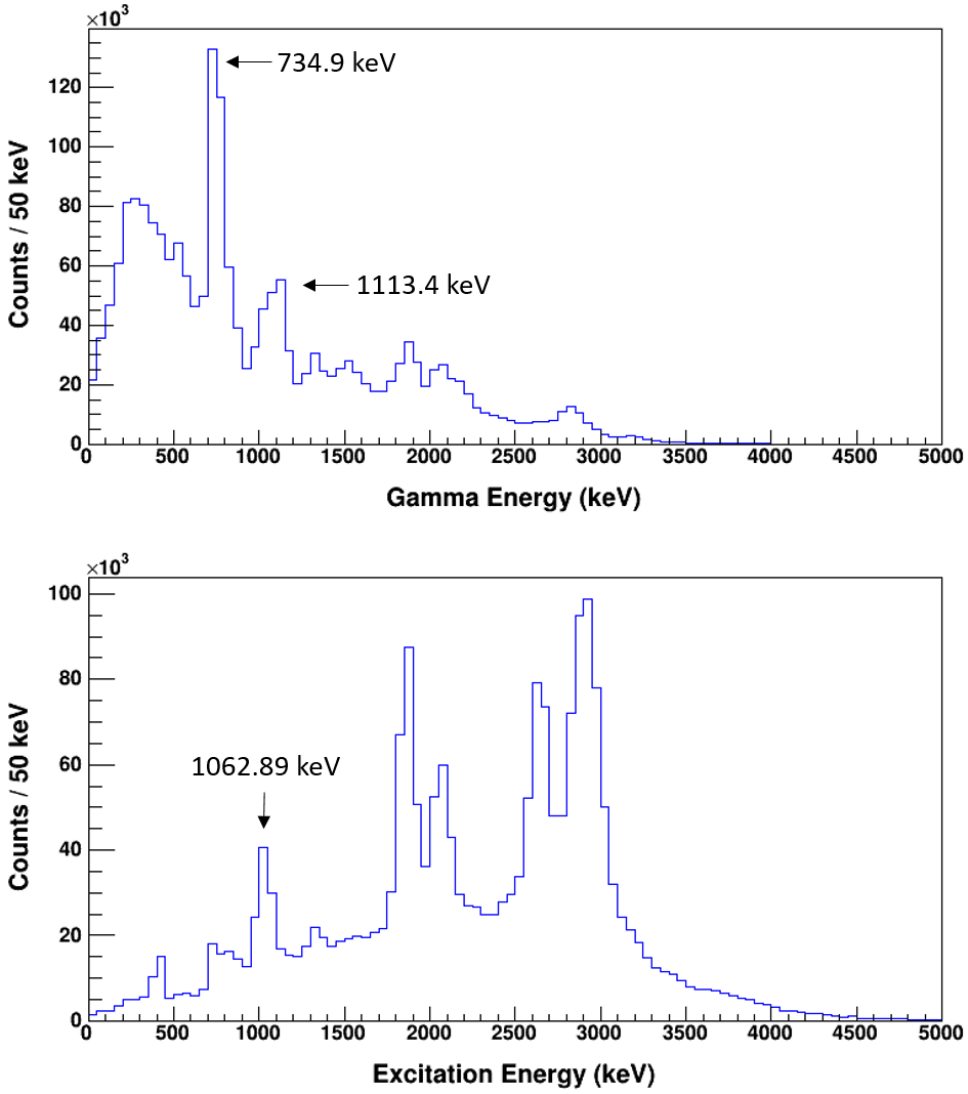

Figure 2.27: (Top) γ-ray energy spectrum of ^{83}Se. (Bottom) Excitation energy spectrum of ^{83}Se.

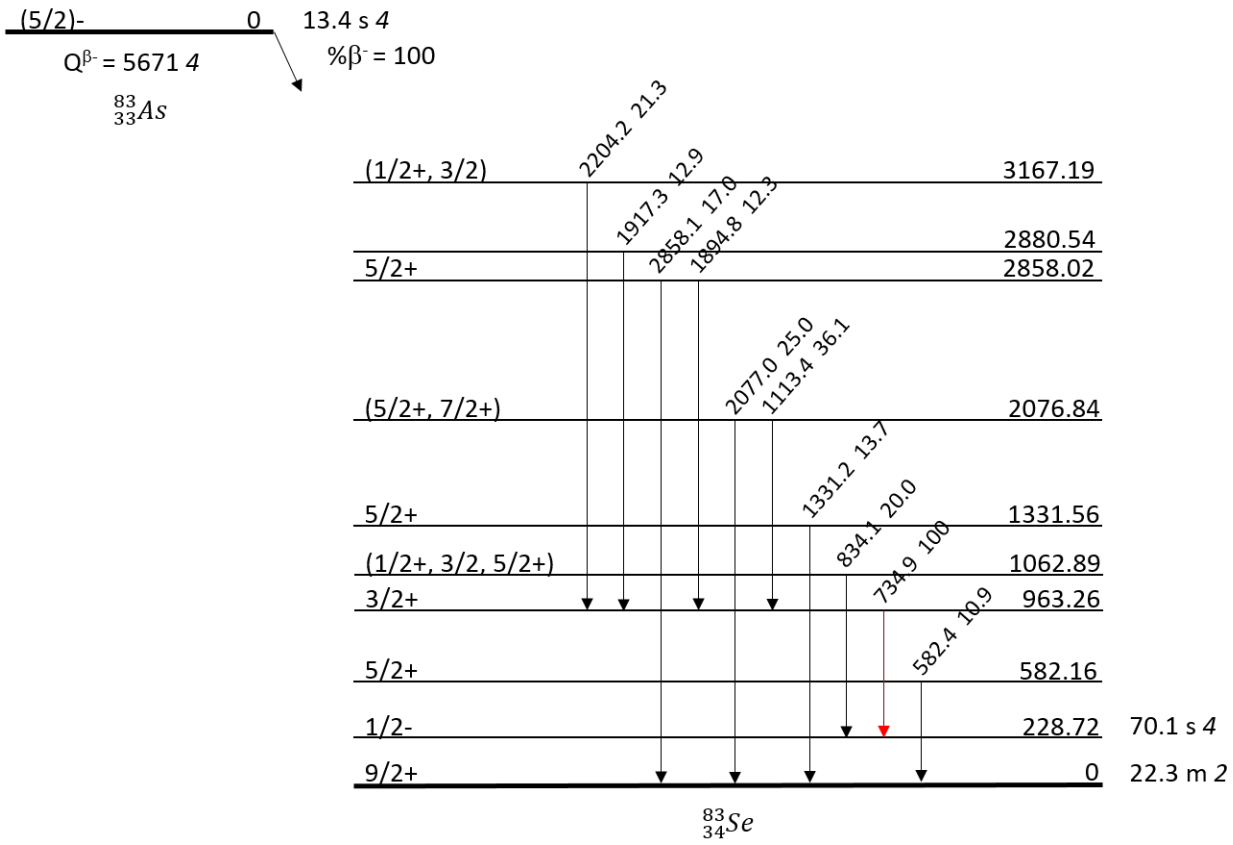

Figure 2.28: Decay scheme of ^{83}As $\rightarrow$ ^{83}Se with selected levels and γ-ray transitions. γ-ray intensities relative to the 734.9 keV transition listed next to γ-ray energies. [74]

Chapter 3

β-Oslo Method

The β-Oslo method [63] is based on the established Oslo method [59–62] for extracting the nuclear level density (NLD) and γ-ray strength function (γSF) of a nucleus. These statistical properties are extracted from data obtained by populating highly excited states in the nucleus of interest and observing the subsequent emission of γ rays as the nucleus de-excites. While the Oslo method uses charged particle reactions to accomplish the population of highly-excited states in the nucleus, the β-Oslo method utilizes β decay of neutron-rich nuclei. The use of β decay gives the β-Oslo method the advantage to experimentally constrain the NLD and γSF of nuclei further from stability than the Oslo method or other reaction-based techniques. However, this method has limitations based on β-decay selection rules and is restricted to nuclei that have large β-decay Q values and a high NLD at the neutron separation energy (S_n), to ensure that the statistical region of the nucleus is being populated. The experimental information extracted from the application of the β-Oslo method is then used to constrain a neutron-capture cross section using the Hauser-Feshbach model for neutron capture as is explained in the Introduction. The β-Oslo method is comprised of four main steps:

1. Unfolding the spectra of γ rays observed, for each excitation energy [59].

2. Isolation of the primary γ rays. These are the first γ rays emitted from each excited state in cascades to the ground state [60].

3. Extraction of the functional forms of the NLD and the transmission coefficient ($T(E_\gamma)$) (See Section 3.4 for conversion of $T(E_\gamma)$ to γSF) [61].

4. Normalization of the NLD and γSF [61, 62].

Each of these four steps will be covered in more detail in the following sections, along with the results of the β-Oslo method being utilized to constrain the ^{82}Se(n,γ)^{83}Se cross section. The level density and γ-ray strength function of ^{83}Se are determined from the β decay of ^{83}As $\rightarrow$ ^{83}Se (see Chapter 2 for experimental details). A flow chart of the various steps, programs, and inputs that are used for a β-Oslo analysis is shown in Figure 3.1. The MAtrix MAnipulation (MAMA) program [76] is used for the first two steps of the analysis: the unfolding of the spectra, and the isolation of primary γ rays. A suite of other programs (shown in bold in Figure 3.1) are used for determination of several input parameters, and for the remaining steps of the Oslo analysis.

3.1 Population of highly excited states in ^{83}Se

The starting point of the β-Oslo method is a 2D matrix of the excitation levels and γ rays emitted in the nucleus of interest (the product of the neutron-capture reaction being constrained). For the case of constraining the cross section of ^{82}Se(n,γ)^{83}Se, the highly excited states of ^{83}Se were populated via the β decay of ^{83}As. This reaction is shown schematically, along with the corresponding neutron-capture reaction, in Figure 3.2. To ensure that the statistical region of the nucleus is being populated, a $Q_{\beta-}$ value above 4 MeV is preferred [77]; ^{83}As has a $Q_{\beta-}$ value of 5.671 MeV. It is also preferred that the $Q_{\beta-}$ value be close to the neutron separation energy (^{83}Se S_n = 5.818 MeV), to cover the majority of the energy range of γ rays emitted after neutron capture.

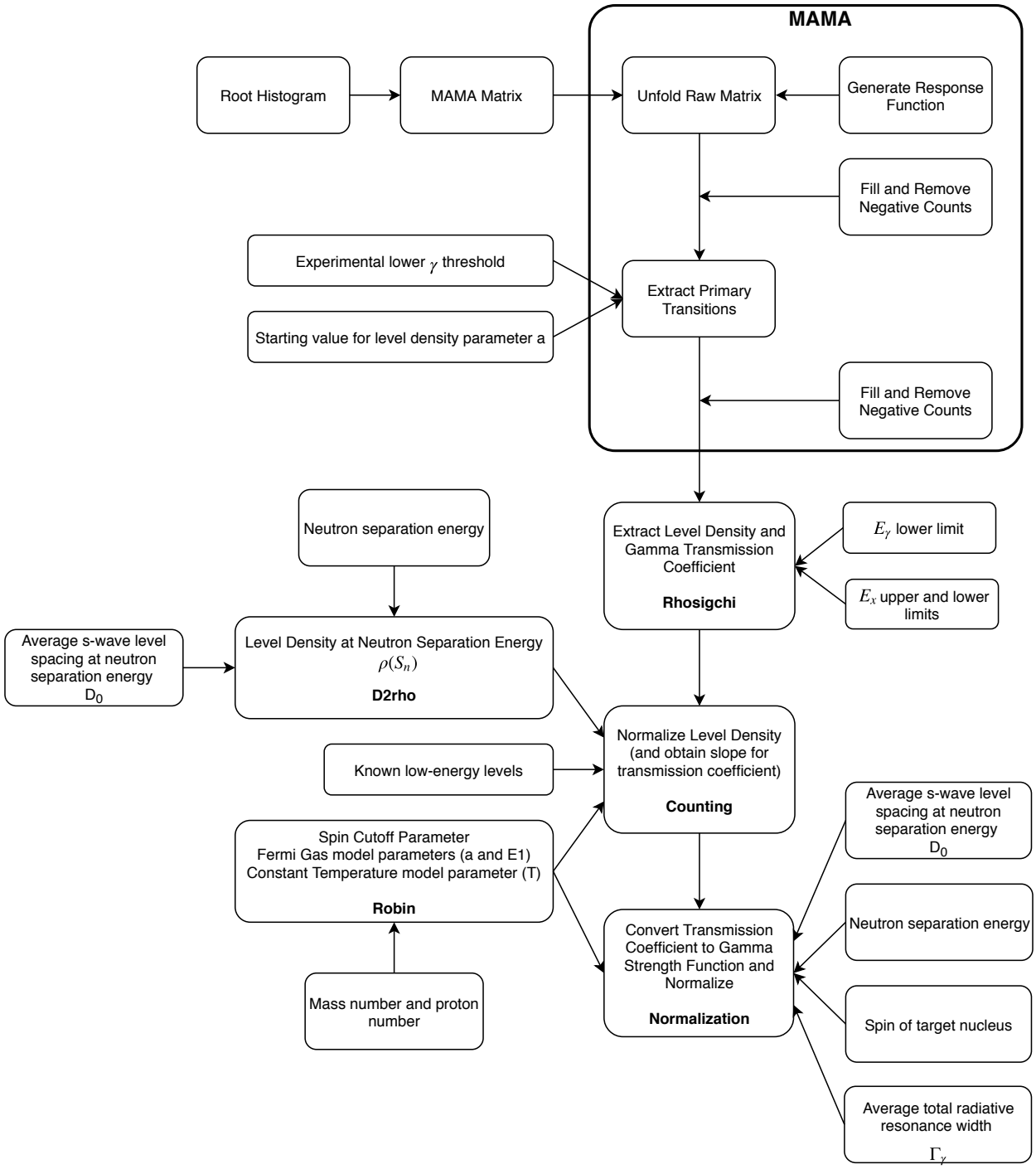

Figure 3.1: Flow chart of Oslo method. Bold items are programs used for the respective steps in the flow chart. Figure from [75].

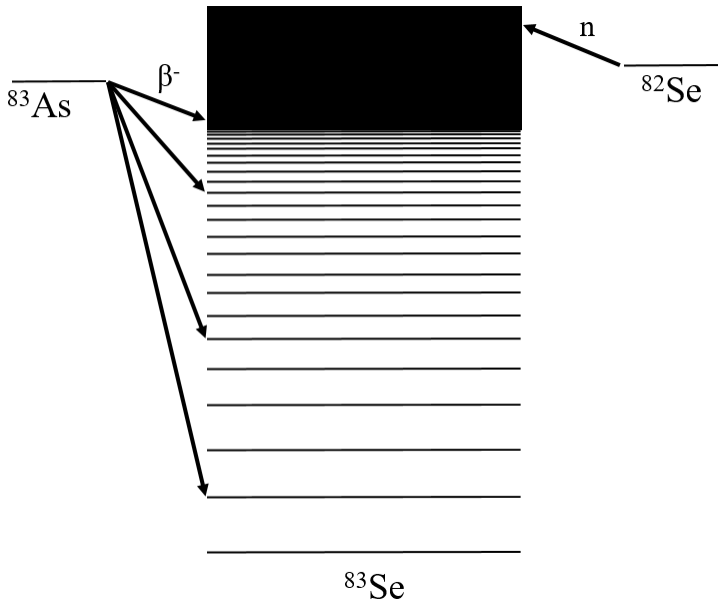

Figure 3.2: Schematic of the population of states in ^{83}Se through the β decay of ^{83}As and neutron capture on ^{82}Se.

3.2 Unfolding

As previously discussed in Chapter 2, the spectra of γ-ray energies deposited in SuN is obtained via the summation of the spectra of each individual segment. While SuN has a high efficiency for detecting the total energy of a single γ ray within the full detector volume (above 80% for a 1 MeV γ ray), the efficiency of an individual segment detecting the full energy of a γ ray is much lower, around 40%. This is mainly due to the various interactions through which the energy of γ rays is deposited in the segments of SuN. While the full energy of a γ ray interacting through photoelectric absorption will be deposited in one interaction, there is a chance that some γ rays will lose energy through pair production or be Compton scattered to another segment, in which case only part of the full energy would be deposited in a given segment. These types of γ ray interactions lead to incomplete energy sums in the γ-ray energy spectra, which is what the method of unfolding addresses.

In order to determine the full γ-ray energies expected from the raw data, an iterative procedure was used to unfold the response function of the detector [59]. This response function, which represents the response of the detector to a range of γ-ray energies, was simulated using Geant4 [78]. The goal of this method is to determine a "unfolded" γ-ray spectrum that, when combined with the response function, will match the experimental data. The "folded" spectrum f can be represented by:

$$f = \mathbf{R}u \tag{3.1}$$

where f is the folded spectrum, $\mathbf{R}$ is the response function matrix, and u is the unfolded spectrum. The iteration method is applied as follows:

1. An initial trial unfolded function is defined as:

$$u^0 = r \tag{3.2}$$

   where r is the observed experimental γ-ray spectra.

2. The first folded spectrum, f^0, is calculated using the response function matrix $\mathbf{R}$ and the first trial unfolded function u^0:

$$f^0 = \mathbf{R}u^0 \tag{3.3}$$

3. The next trial unfolded function, u^1, is determined by applying the difference of the folded spectrum, f^0, and the observed spectrum r to the original trial unfolded function

u^0 as a correction factor:

$$u^1 = u^0 + (r - f^0) \tag{3.4}$$

4. The new trial unfolded function is folded to determine the next folded spectrum, f^1, which is then used to calculate the next trial unfolded function:

$$f^1 = \mathbf{R}u^1 \tag{3.5}$$

$$u^2 = u^1 + (r - f^1) \tag{3.6}$$

Step 4 is repeated until the folded spectrum matches the experimental spectrum within uncertainties ($f^i \approx r$). Typically, around 30 iterations are performed.

The unfolding procedure used in the traditional Oslo and β-Oslo methods previously focused only on unfolding the E_γ axis of the 2D matrix shown in Figure 2.26. A recent development to the β-Oslo method is to also unfold the E_x axis [79]. Since the determination of the excitation energy is directly linked to the measurement of γ-ray energies, the excitation energy is also effected by incomplete summing of γ-ray cascades. There is also the chance of additional background from β-decay electrons also interacting with SuN. The response function is dependent on the initial excitation energy (E_x), the γ-ray multiplicity (M_γ) at the excitation energy, and the Q_β value of the decay being measured. Response functions covering the possible combinations of E_x, M_γ, and Q_β values have been simulated in Geant4. The rest of the unfolding proceeds in the same method described above. The unfolded 2D matrix for ^{83}Se obtained by applying this method to both the E_γ and E_x axis of the original raw 2D matrix for ^{83}Se is shown in Figure 3.3.

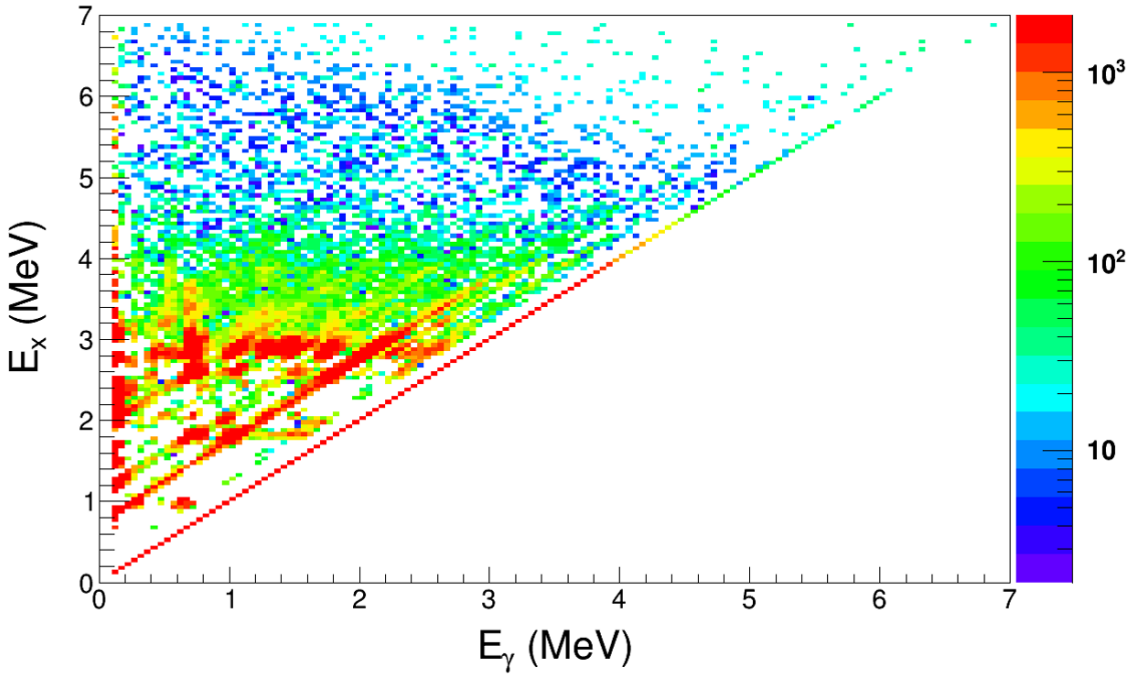

Figure 3.3: Unfolded E_x, E_γ matrix for ^{83}Se, with 50 keV binning.

3.3 Extraction of primary γ rays

To extract the functional forms of the nuclear level density and γ-ray strength function, the E_x, E_γ matrix needs to contain only the primary, or first, γ rays emitted in cascades from each excited state. The first generation method was developed to extract these primary γ rays for each excitation energy bin [60]. The first generation method is based on the assumption that the γ-ray emission from any excited state is independent of how that excited state was populated. For each excitation energy bin i (here, 200 keV wide) of the unfolded matrix, the γ-ray spectrum, f_i, contains γ rays from all cascades that are possible from excited states within that excitation energy bin. Therefore, γ-ray spectra $f_{j<i}$, where j represents excitation energy bins below i, contain the same γ-ray transitions as f_i except for the first γ rays emitted from excited states within bin i. The first generation, or primary γ ray,

spectrum h_i of excitation energy bin i can then be found by

$$h_i = f_i - g_i \tag{3.7}$$

where g_i is a sum of all spectra.

$$g_i = \sum_j n_{ij} w_{ij} f_i \tag{3.8}$$

g_i is weighted by a coefficient w_{ij}, which represents the probability of a γ-ray transition from bin i to excited states in bin j and is normalized so that $\sum_j w_{ij} = 1$. The coefficient n_{ij} accounts for the different probabilities of populating excited states in bin i and the lower energy states in bin j, and is calculated using information about the average γ-ray multiplicity $\langle M \rangle$ of each bin and the total number of counts in the spectrum f_i, $A(f)$,

$$n_{ij} = \frac{\langle M_j \rangle A(f_i)}{\langle M_i \rangle A(f_j)}. \tag{3.9}$$

This procedure of subtracting the γ-ray spectra of lower excitation energy bins from the higher excitation energy bin of interest is done for each bin in the E_x, E_γ matrix, until only the primary γ rays remain. The primary matrix obtained for ^{83}Se is shown in Figure 3.4.

3.4 Extraction of the functional forms of the NLD and γSF

The assumption that the probability of a decay to a specific energy state is independent of the means of formation has been shown to be valid for compound reactions. Therefore, the probability $P(E, E_\gamma)$ of a γ-ray of energy E_γ being emitted from a specific excitation

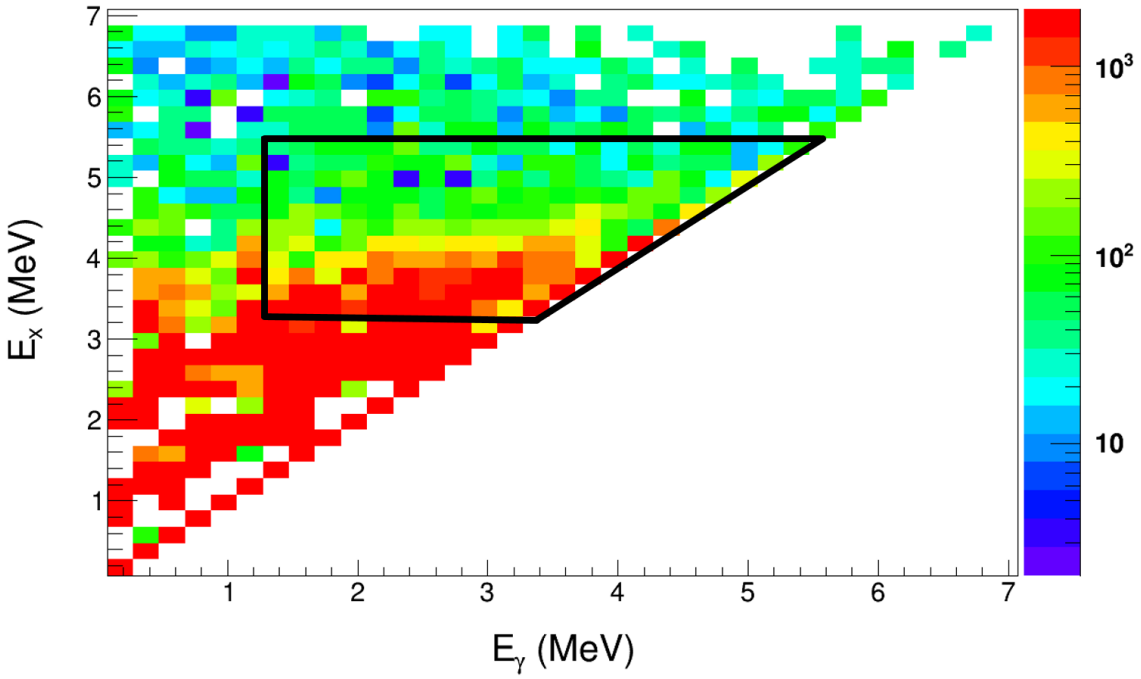

Figure 3.4: Primary E_x, E_γ matrix for ^{83}Se, with 200 keV binning.

energy E_x, is proportional to the level density at the final excitation energy, $\rho(E_f)$ (where $E_f = E_x - E_\gamma$), and the γ-ray transmission coefficient $\mathcal{T}(E_\gamma)$,

$$P(E, E_\gamma) \propto \rho(E - E_\gamma)\mathcal{T}(E_\gamma). \tag{3.10}$$

Ultimately, $\mathcal{T}(E_\gamma)$ will be converted to the γ-ray strength function (γSF), assuming the γ-ray transitions are dipoles, via

$$\gamma SF = \frac{1}{2\pi}\frac{\mathcal{T}(E_\gamma)}{E_\gamma^3} \tag{3.11}$$

The relationship in Equation 3.11 relies on the assumption that the γ-ray transmission coefficient is independent of the excitation energy, which has been shown to be valid in a study of ^{238}Np [77]. Based on this, the functional forms of the nuclear level density (NLD)

and γ-ray transmission coefficient can be simultaneously extracted from the primary E_x, E_γ matrix [61]. First, though, the primary matrix must be normalized so that for every excitation energy bin the sum of all γ-ray energies is unity:

$$\sum_{E_\gamma=E_\gamma^{min}}^{E_\gamma^{max}} P(E, E_\gamma) = 1. \tag{3.12}$$

The limits of the region of the primary matrix used for the extraction are shown in black in Figure 3.4. These limits are chosen to ensure that the data are from the statistical energy region. The lower limit of E_γ is 1275 keV. The lower limit of E_x is 3275 keV, and the upper limit is 5475 keV. These limits are specified in the *rhosigchi* program, which performs the extraction. The extracted NLD and $\mathcal{T}(E_\gamma)$ are functional forms, described by the following equations:

$$\rho(E, E_\gamma) = Ae^{\alpha(E-E_\gamma)} \tag{3.13}$$

$$\mathcal{T}(E_\gamma) = Be^{\alpha E_\gamma}, \tag{3.14}$$

where α is the slope, and A and B are scaling factors. To determine the physical solutions of the NLD and $\mathcal{T}(E_\gamma)$, the A, B, and α parameters must be found through normalization, which will be discussed in the following section.

3.5 Normalization of the NLD and γSF

There are three pieces of information needed to normalize the functional forms of the NLD and γSF. Parameters A and α from Eq. 3.13 and 3.14 are determined from known discreet levels at low excitation energies and the level density at the neutron separation energy

($\rho(S_n)$). Known levels are obtained from β-decay experiments, while $\rho(S_n)$ is calculated using the average level spacing for s-wave neutrons at the neutron separation energy (D_0). D_0 is the inverse of the NLD, for levels that would be populated through a neutron-capture reaction and can be measured by neutron-capture experiments. Parameter B of Eq. 3.14, which represents the magnitude of the γSF, is calculated using the average radiative width at the neutron separation energy, Γ_γ, which can also be obtained through neutron-capture experiments.

It is worth noting, much of this experimental information discussed above is limited for many of the nuclei of interest for r-process calculations, due to short half-lives. Therefore, theoretical calculations can be used in place of experimentally-determined values, or these normalization parameters can be determined through extrapolations using information of nearby nuclei. In this work, the NLD was normalized using known levels in ^{83}Se from β decay, and a D_0 value reported in literature. The γSF was normalized using a Γ_γ value determine from a fit to extrapolated GDR data from nearby nuclei, to test the method generally used when experimental Γ_γ values are not available. The Γ_γ value determined through this method was later compared to one reported in literature from neutron-capture data, which is currently the best data available for ^{83}Se.

3.5.1 NLD

The nuclear level density of ^{83}Se determined via the β-Oslo method is shown in Figure 3.5. The known discreet levels shown in this figure were used to normalize the NLD at low energies, between 675 keV and 1675 keV. The NLD at higher energies was normalized using $\rho(S_n)$, which was determined using the program *D2rho*, which calculates the level density at the neutron separation energy from the average level spacing parameter (D_0). A D_0 value of

5000 ± 2500 eV [80] results in a $\rho(S_n)$ value of 5907 ± 3193 MeV^{-1}. Since the experimental data does not reach all the way up to the neutron separation energy, the Constant Temperature model is used to determine an extrapolation of the level density between the higher energy levels of the level density and $\rho(S_n)$. For the CT model, a temperature parameter of 0.84 was used, as reported by von Egidy and Bucurescu [29]. If using the BSFG model for the extrapolation of the level density, the level density parameter a, from Equation 1.8, is reported by von Egidy and Bucurescu to be 9.44 [29]. The normalization was performed through a simultaneous fit of the experimental data to the low energy known levels and the CT model extrapolation. The upper and lower limits of the NLD shown in Figure 3.5 were determined from a systematic study based on the uncertainty of the D_0 value used. The upper value of $\rho(S_n)$ was determined to be 13350 ± 7158 MeV^{-1}, while the lower value was determined to be 3459 ± 1888 MeV^{-1}. From Equation 3.13, the A parameter was determined to be 4.51, and the α parameter was determined to be 0.85.

3.5.2 Limited spin population

One thing that needs to be taken into account is the limited range of spins that are populated based on the restrictions of β decay. The ground state of ^{83}As is $\frac{5}{2}-$. By taking into account one allowed β-decay transition and one γ-ray transition, the range of spins that is expected to be populated in ^{83}Se is $\frac{1}{2}\pm$ to $\frac{9}{2}\pm$. Therefore, the primary γ rays observed in this experiment are restricted to that spin range. Since the α parameter (of Equations 3.13 and 3.14) determined in the normalization of the NLD is also used for the normalization of the γSF, the NLD needs to be reduced to account for this restricted spin range. To determine a reduction factor, a theoretical calculation of the NLD from Goriely [37] was used. For each spin, the percentage of the total level density was calculated, and is shown in Figure 3.6.

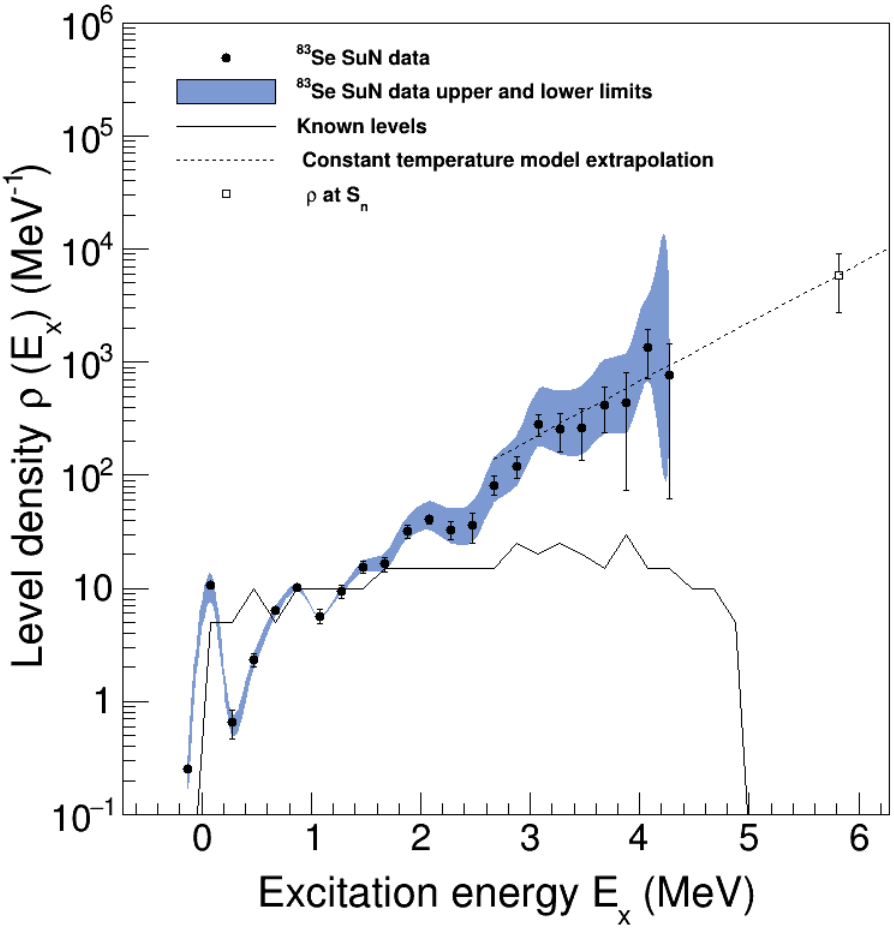

Figure 3.5: Nuclear level density for ^{83}Se, with the experimental data (black circles) as well as the upper and lower limits (blue band). Known levels are indicated by the solid black line, the level density at the neutron separation energy, $\rho(S_n)$, is indicated by the white square, and the Constant Temperature model extrapolation is shown as the dashed black line.

For ^{83}Se, it was determined that 52.3 % of the level density fell within the spin range of $\frac{1}{2}\pm$ to $\frac{9}{2}\pm$. Using this reduction factor, $\rho(S_n)$ values of 2326.8 MeV^{-1}, 3490.5 MeV^{-1}, and 6982 MeV^{-1} were calculated and used to determine the α parameter.

3.5.3 γSF

The normalized γSF of ^{83}Se is shown in Figure 3.7. To determine parameter B of equation 3.14, the average radiative width, Γ_γ, needs to be calculated. A systematic approach was used, by studying the γSF of nearby nuclei. Photoabsorption cross section data for ^{75}As,

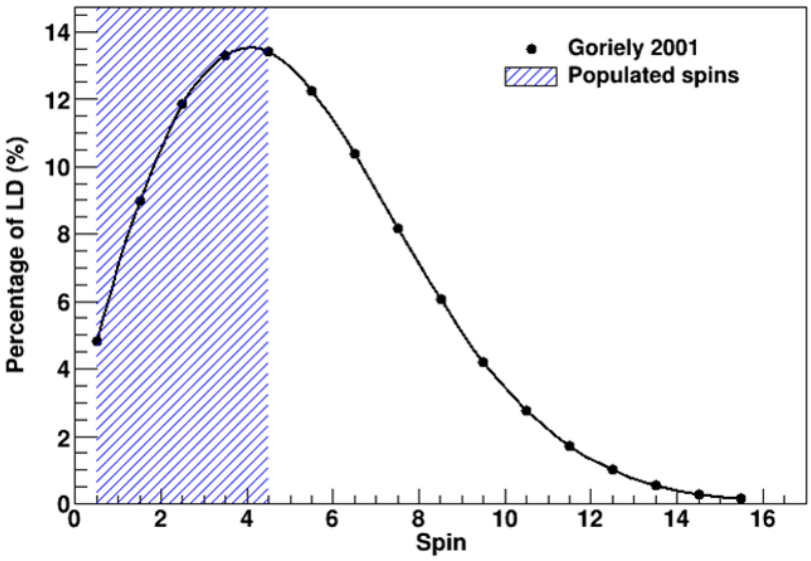

Figure 3.6: Percentage of the total level density of ^{83}Se determined from Ref. [37] as a function of the spin. Spin range highlighted in blue represents the spin range populated following an allowed β decay and one dipole transition.

^{80}Se, and ^{82}Se were obtained from [81], and the γ,n cross section, σ_γ, of each was converted to a γSF using the equation

$$\gamma SF(MeV^{-3}) = \frac{\sigma_\gamma^2}{(3\pi\hbar)^2}. \tag{3.15}$$

These γSFs are also shown in Figure 3.7. Photoabsorption cross sections are usually measured above the neutron separation energy, while the data obtained from β-Oslo measurements is extracted below the neutron separation energy. Therefore, the γSF of each set of data must be extrapolated to lower energies. The shape of the γSF is described very well at higher energies by a Generalized Lorentzian (GLO) function, and the GLO has also been used to estimate the shape of the γSF at lower energies as well. Each γSF calculated from γ,n data was fitted to the GLO function, and the average value of each parameter was used to determine an average GLO function that was extrapolated to lower energies. The average parameter values are summarized in Table 3.1. A χ^2 minimization (shown in Figure 3.8) was then performed on the fit of the experimental γSF data to the average GDR extrapolation

from 3.5 to 5.5 MeV to determine Γ_γ. For ^{83}Se, Γ_γ was determined to be 74.09(3.68) meV. This Γ_γ does not agree with reported value of 126(15) meV from [82]. It is presently unknown as to why there is a discrepancy. The upper and lower limits of the γSF, determined from the uncertainty on Γ_γ and the NLD, is represented by the blue band in Figure 3.7.

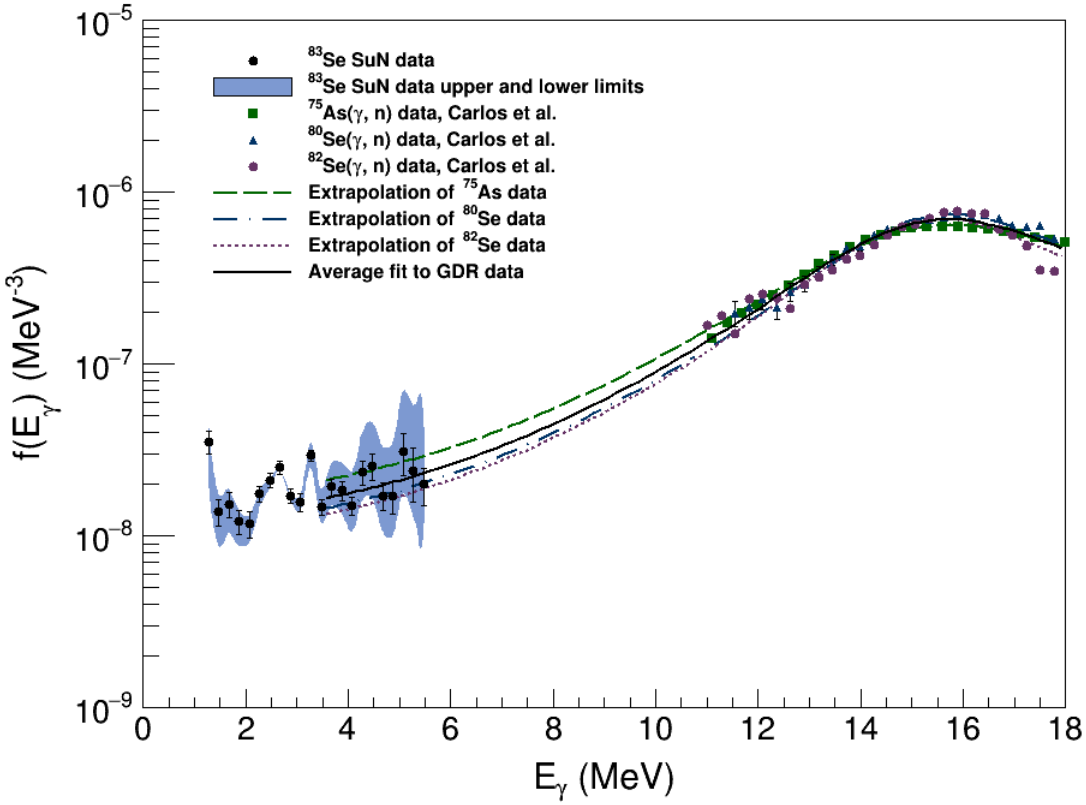

Figure 3.7: Gamma strength function for ^{83}Se (black circles) with the upper and lower limits based on systematic uncertainty are indicated by the blue band. Photoabsorption cross section data from [81] (green squares, blue triangles, purple circles) and the corresponding fit of the GLO function to the data and an average fit are also shown.

3.6 Constraint of ^{82}Se(n,γ)^{83}Se via the β-Oslo Method

The NLD and γSF detailed above were then used as input in a Hauser-Feshbach reaction code to obtain the neutron-capture cross section. The TALYS reaction code (version 1.95) was used [12]. The NLD was read in to TALYS in tabular form, which was generated using

Table 3.1: GDR parameters determined from the fit of a GLO function to photoabsorption cross section data.

Nucleus	E_{E1} (MeV)	σ_{E1} (mb)	Γ_{E1} (MeV)
^{75}As	16.96	127.62	7.86
^{80}Se	16.46	152.55	5.51
^{82}Se	16.20	141.57	5.24
Average	16.54	140.58	6.20

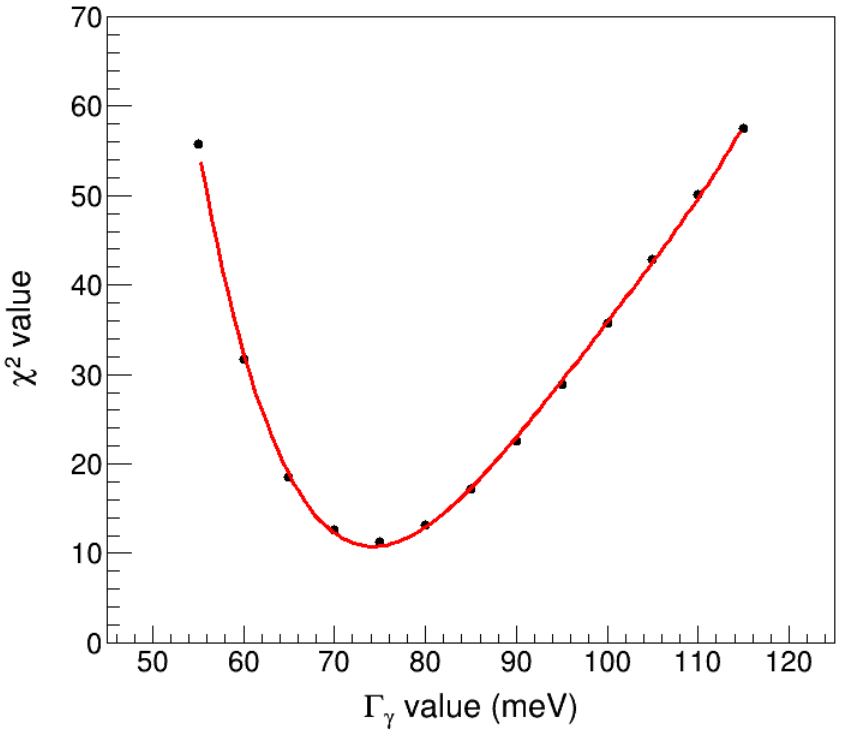

Figure 3.8: A plot of χ^2 values versus a range of Γ_γ values, obtained from fitting the average GDR resonance parameters to the experimental γSF to determine the best Γ_γ for the data set.

a fit of the CT model to the experimental data. The experimental γSF was fitted with a E1 GLO function combined with an exponential function to represent the upbend. These fits were used to generate a tabular form of the γSF, which were then be read into TALYS. The resulting ^{82}Se$(n,\gamma)^{83}$Se reaction cross section is shown in Figure. 3.9. The light blue lines indicate the systematic uncertainty of the cross section calculation, based on the upper and

lower limits of the properties constrained in the β-Oslo method. Along with the constrained cross section, a band representing cross sections calculated with all possible combinations of the NLD and γSF models available in TALYS version 1.95 (summarized in Table 3.2) is also shown. Ultimately, this cross section will be compared to a cross section determined in a direct measurement of the ^{82}Se(n,γ)^{83}Se reaction, which is covered in the next chapter.

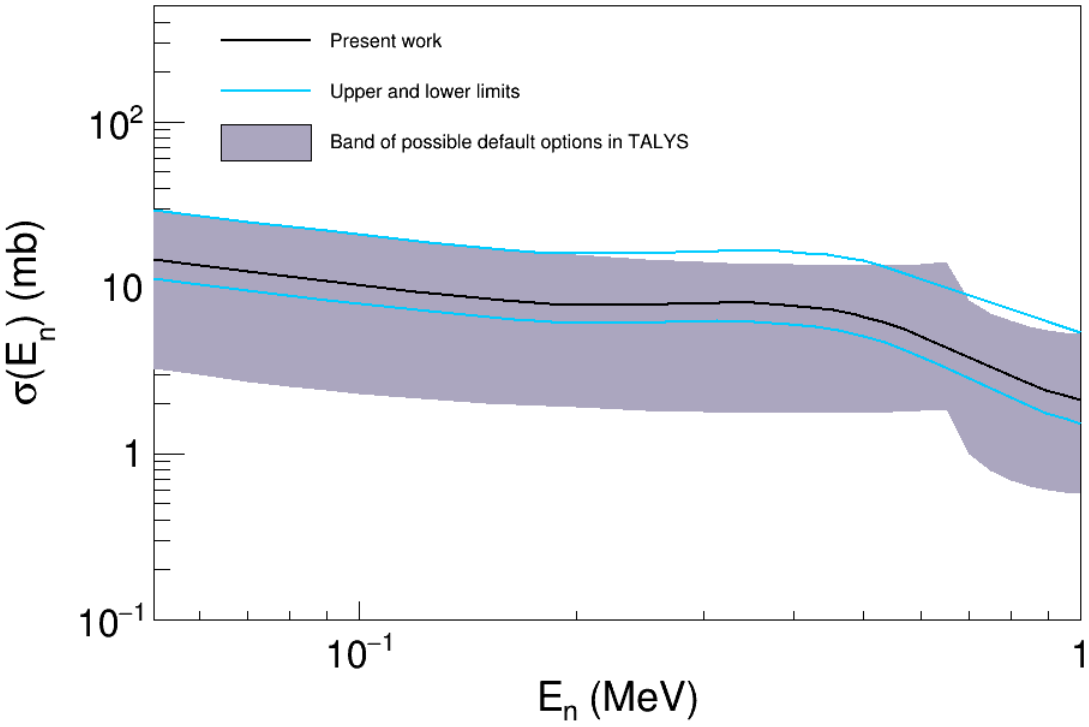

Figure 3.9: Cross section of the ^{82}Se(n,γ)^{83}Se reaction calculated using TALYS (black). The upper and lower limits (light blue) are based on the uncertainty of the experimental NLD and γSF. The grey band shows the range of cross sections resulting from combinations of all available NLD and γSF models.

Table 3.2: NLD and γSF models available in TALYS.

NLD Models	γSF Models
CT + BSFG [34]	Kopecky-Uhl generalized Lorentzian [42]
BSFG [31, 34]	Brink-Axel Lorentzian [40, 41]
Generalized superfluid [83]	Hartree-Fock BCS tables [84]
Microscopic level densities (Skyrme force) from Goriely [36]	HFB tables [84]
Microscopic level densities (Skyrme force) from Hilaire combinatorial tables [37]	Goriely's hybrid model [85]
Microscopic level densities (HFB, Gogny force) from Hilaire combinatorial tables [38]	Goriely T-dependent HFB
	T-dependent RMF
	Gogny D1M HFB+QRPA

Chapter 4

Direct Measurement of ^{82}Se(n,γ)^{83}Se

A direct measurement of neutron capture on ^{82}Se was performed at Los Alamos National Laboratory in Los Alamos, New Mexico. This experiment was performed with the Detector for Advanced Neutron Capture Experiments (DANCE) [86–88], which is positioned on a dedicated neutron flight path at the Lujan Neutron Scattering Center of LANSCE, the Los Alamos Neutron Science Center. At LANSCE, a linear accelerator produces an 800 MeV high intensity proton beam that is bunched in pulses that are 250 ns wide at the base of the pulse shape. This proton beam is impinged onto a tungsten production target, producing a white neutron source via spallation reactions [89]. The neutrons are then partially moderated by a room-temperature water moderator surrounding the tungsten target until ultimately a neutron beam ranging in energy from a few meV to a few MeV travels down flight path 14 to the experimental setup.

4.1 DANCE: The Detector for Advanced Neutron Capture Experiments

DANCE is a large volume γ-ray calorimeter based on a 162 element close-packed spherical-shell geometry around the target position [90]. Each BaF_2 detector crystal is 734 cm^3 in volume and connected to a photomultiplier tube (PMT). The face of each crystal is located

at a distance of approximately 19 cm from the target position. All detector crystals view the same solid angle, and with all 162 crystals in place, 4π coverage is achieved. However, two crystals are excluded from the array to account for the neutron beam traveling through the device. With two crystals removed, the crystals cover a total solid angle of approximately 3.5 π steradians. DANCE has a high efficiency for detecting γ rays, with an efficiency of approximately 87% for a single 1 MeV γ ray [91]. Inside of DANCE, a 6 cm thick shell of ^{6}LiH surrounds the target position to reduce the background produced by scattered neutrons capturing in the BaF_2 crystals [92]. A schematic of DANCE is shown in Figure 4.1. BaF_2 has

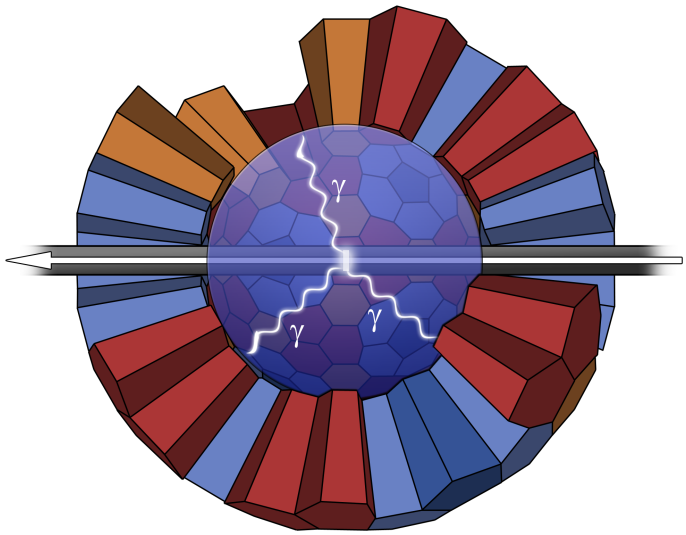

Figure 4.1: Schematic representation of the DANCE detector geometry, including the beamline, and LiH sphere.

the distinction of being the fastest known inorganic scintillator. There are two components to its light emission spectrum, a fast component with a 220 nm wavelength and 0.6 ns decay time, and a slow component with a 310 nm wavelength and a 600 ns decay time [93]. The subnanosecond decay time of the fast component provides the ability for a precise determination of timing.

The fast and slow components are also utilized to differentiate γ-ray signals and signals originating from α decay which is intrinsic to BaF_2 detectors. Barium is chemically analogous to radium, so it is difficult to produce pure barium without any radium impurities. Therefore, the BaF_2 crystals have some internal background from isotopes along the radium decay chain. The main decays observed from the radium background are alpha decays from ^{226}Ra (4.78 MeV), ^{222}Rn (5.49 MeV), ^{218}Po (6.0 MeV), and ^{214}Po (7.69 MeV). The amplitude of the components of the BaF_2 light spectrum depends on the energy, mass, and charge of the interacting particles and will therefore be different for γ rays and alpha particles. An example of the signals obtained from the interaction of a γ ray versus an alpha particle is shown in Figure 4.2. To separate the alpha particles from the spectra, signals are integrated

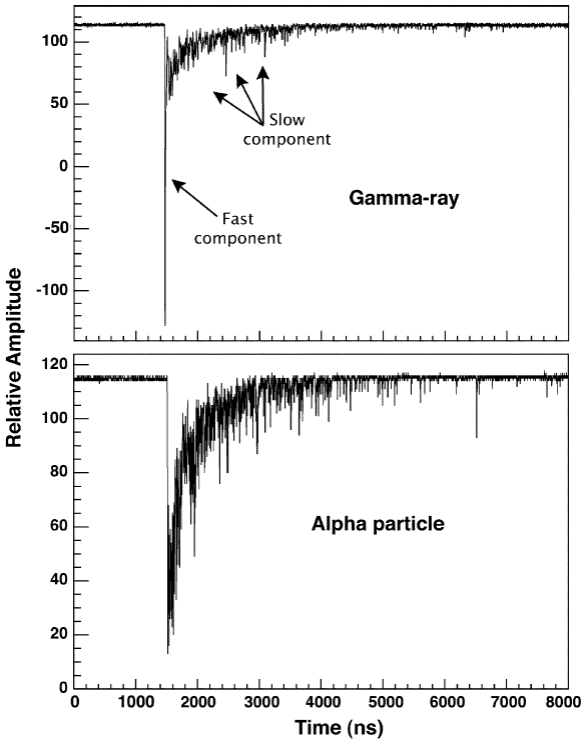

Figure 4.2: Example of signals from a γ ray and an alpha particle, from a single BaF_2 crystal. © 2006 IEEE Reprinted, with permission, from [94].

with two different integration times (short - first 64 ns and long - next 1 μs) and the plot of

the short integral versus the long integral (shown in Figure 4.3) is used to distinguish alpha particle signals from gamma ray signals. A gate is applied around the signals from alpha particles in software, as they are used for calibrations that will be discussed in Section 4.3, and then ignored in the analysis.

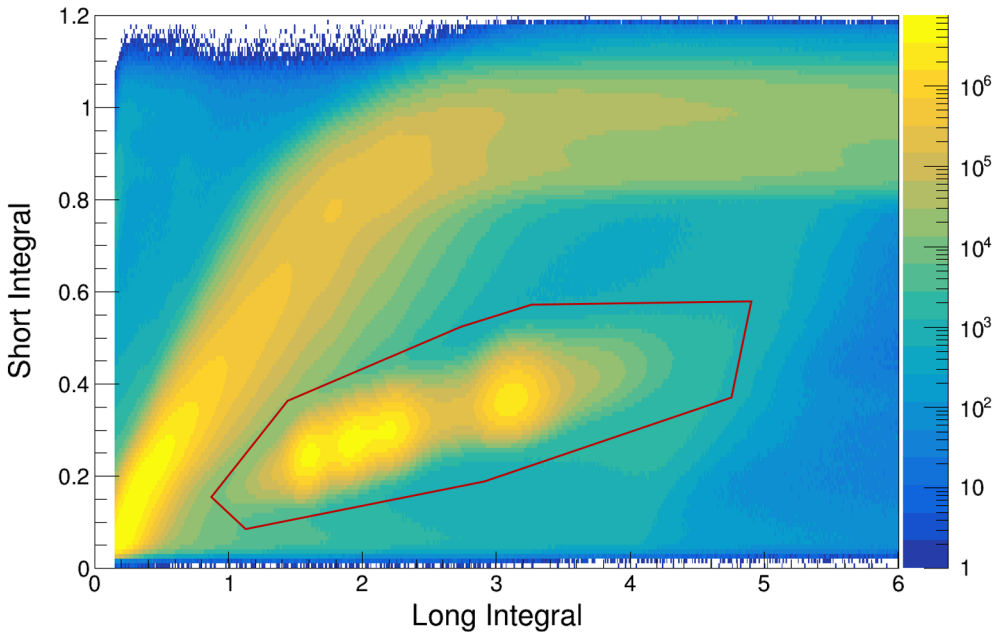

Figure 4.3: Short integral of the detector signal versus the long integral of detector signal from the data taken with the ^{82}Se target. Gate used to separate alpha signals shown in red.

After the alpha signals have been gated out, the remaining signals are used to obtain calorimetric information about the cascades of γ rays emitted following neutron capture. Based on the timestamps of signals, an event is created by grouping all signals identified as γ rays within a 10 ns coincidence window (this is user-selectable and can be optimized during the analysis). The energy deposited in each crystal, E_{Cr}, is determined by subtracting the short integral of the signal from the long integral. The energy of all γ rays identified within a particular event are summed and recorded as E_{Sum}. The number of crystals (multiplicity) identified as participating in the event is denoted as M_{Cr}. However, there is the possibility for a single γ ray to Compton scatter and be detected by another crystal. In such a case, the

M_{Cr} would be recorded as 2 instead of 1. To account for this, a cluster of crystals is defined by the nearest neighboring crystals to the crystal where the initial photon interaction was believed to occur. In the case of a γ ray depositing energy into a crystal and then Compton scattering into a neighboring crystal, the cluster multiplicity, M_{Cl}, would be denoted as 1 and M_{Cr} would equal n+1. The sum of energy deposited within a cluster is recorded as E_{Cl}. M_{Cl} and E_{Cl} are a better representation of the true cascade multiplicity and individual γ-ray energies for typical multiplicities and energies produced in neutron capture due to the possibility of γ rays scattering and depositing energy in multiple crystals [91]. The total energy observed by DANCE, E_{Sum}, corresponds to the Q-value of the neutron capture reaction that is occurring, which provides the ability to cleanly identify neutron capture on different isotopes.

Another important quantity is the neutron energy, which is determined via time-of-flight measurements. The time-of-flight is measured between the timing of the initial γ-ray interaction of the event in DANCE and the reference signal of the proton pulse immediately before it interacts with the tungsten target. The neutron energy is then deduced using the non-relativistic (since the maximum neutron energy considered here is 1 MeV, which is approximately 5% of the speed of light) kinematic energy equation (Equation 4.1) using time-of-flight, t_{TOF}, the length of the flightpath, $l_{FP} = 20.25$ m, and the neutron mass, $m_n = 939.57 \ \frac{MeV}{c^2}$.

$$E_n = \frac{1}{2} m_n \frac{l_{FP}^2}{t_{TOF}^2} \tag{4.1}$$

4.2 Targets

An enriched ^{82}Se metal was obtained from Trace Sciences [95] and was pressed into two pellets that were glued together to form a 176.6 mg, 5 mm target. The target was attached to an aluminum target holder with kapton tape. Pictures of the target are shown in Figure 4.4. A summary of the isotopic composition of the target is provided in Table 4.1. In addition to the ^{82}Se target, several other targets were utilized for this experiment as well. A measurement of neutron capture on a 4-mm ^{197}Au target was used to determine the normalization for the neutron fluence measured by the neutron beam monitors downstream of DANCE (see Section 4.4 for more information). A 97.4-mg ^{208}Pb target, which has a large neutron scattering cross section relative to the neutron capture cross section, was used to characterize the background of neutrons scattering off of the target and interacting with the BaF_2 crystals, creating signatures of neutron capture on barium (See Section 4.5.1.1 for more information). Two γ-ray sources, ^{88}Y and ^{22}Na, were also used for energy calibrations.

Table 4.1: Composition of the enriched ^{82}Se target and the Q-value of neutron capture on each isotope.

Isotope	Enrichment (%)	(n, γ) Q-value (MeV)
^{74}Se	<0.01	8.03
^{76}Se	<0.01	7.42
^{77}Se	<0.01	10.5
^{78}Se	<0.01	6.96
^{80}Se	3.77	6.70
^{82}Se	**96.20**	**5.82**

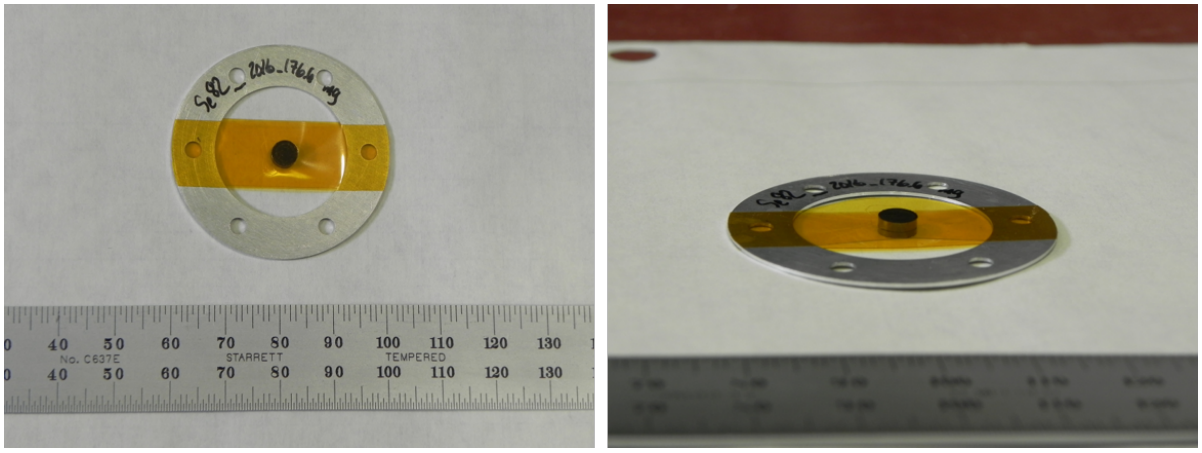

Figure 4.4: Photographs of ^{82}Se target and target holder from a top down view (left) and a side view (right).

4.3 Calibrations

The response of the BaF_2 crystals have been observed to drift over time due to temperature sensitivity, so the energy calibration of DANCE is performed using a combination of standard gamma sources to create a calibration template and intrinsic alpha signals to perform a run-by-run calibration. The initial energy calibration for each crystal was performed using ^{88}Y and ^{22}Na. An example of the fit to ^{22}Na data and the calibrated energy spectrum for one crystal are shown in Figure 4.5. This initial calibration is applied to the raw BaF_2 spectra and then saved as a template. Each subsequent data run is then calibrated on a run-by-run basis using the signals from alpha particles that are intrinsic to the BaF_2 crystals as discussed above. An example of the alpha calibration spectra and fit used to extract the energy calibration for one crystal is shown in Figure 4.6.

The timing between crystals is also calibrated on a run-by-run basis. This calibration is performed by utilizing Compton scatter events. For each run, time offsets for pairs of crystals are adjusted so that Compton scatter events in adjacent crystals have the same timing.

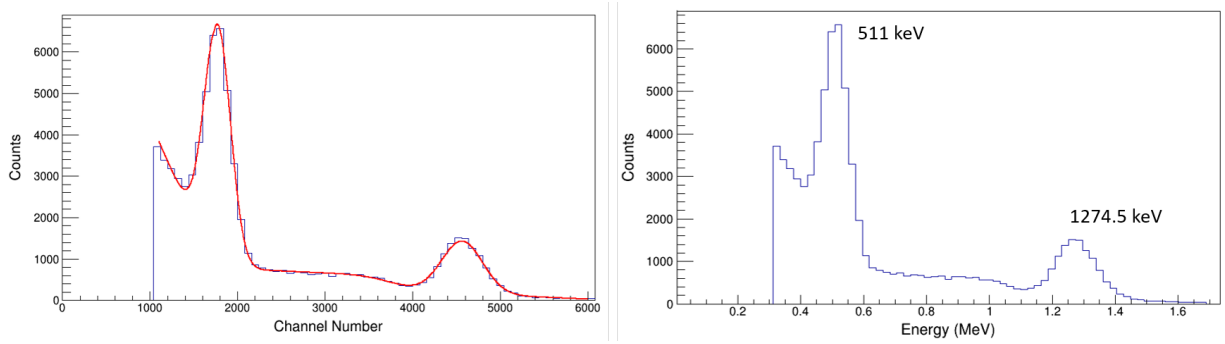

Figure 4.5: (Left) Representation of fit used for calibration with a ^{22}Na source. (Right) Calibrated ^{22}Na spectrum.

4.4 Neutron Fluence Characterization

Another important piece of information for the determination of a cross section is the neutron fluence, or the number of neutrons per unit of area. The fluence is characterized using a series of neutron beam monitors located downstream of DANCE. The beam monitors provide a neutron fluence measurement that is proportional to that at the target position in the center of DANCE. One of these beam monitors was a silicon detector viewing a ^{6}LiF converter foil that utilizes the ^{6}Li(n, α)^{3}H reaction. The first beam monitor is located at 22.632 meters on the flightpath. The second beam monitor used was a gas-filled ion chamber that detects fragments from neutron-induced fission on a ^{235}U foil. The second beam monitor is located at 22.794 meters on the flightpath.

The information recorded from each of the two beam monitors is the yield, or the number of recorded reactions, per neutron energy bin, $Y_{BM}(E_n)$. The fluence, Φ_{BM}, measured at the beam monitor position, can be deduced from Equation 4.2, where σ_{BM} is the known cross section of the reaction utilized by each beam monitor

$$\Phi_{BM}(E_n) \propto \frac{Y_{BM}(E_n)}{\sigma_{BM}(E_n)}. \tag{4.2}$$

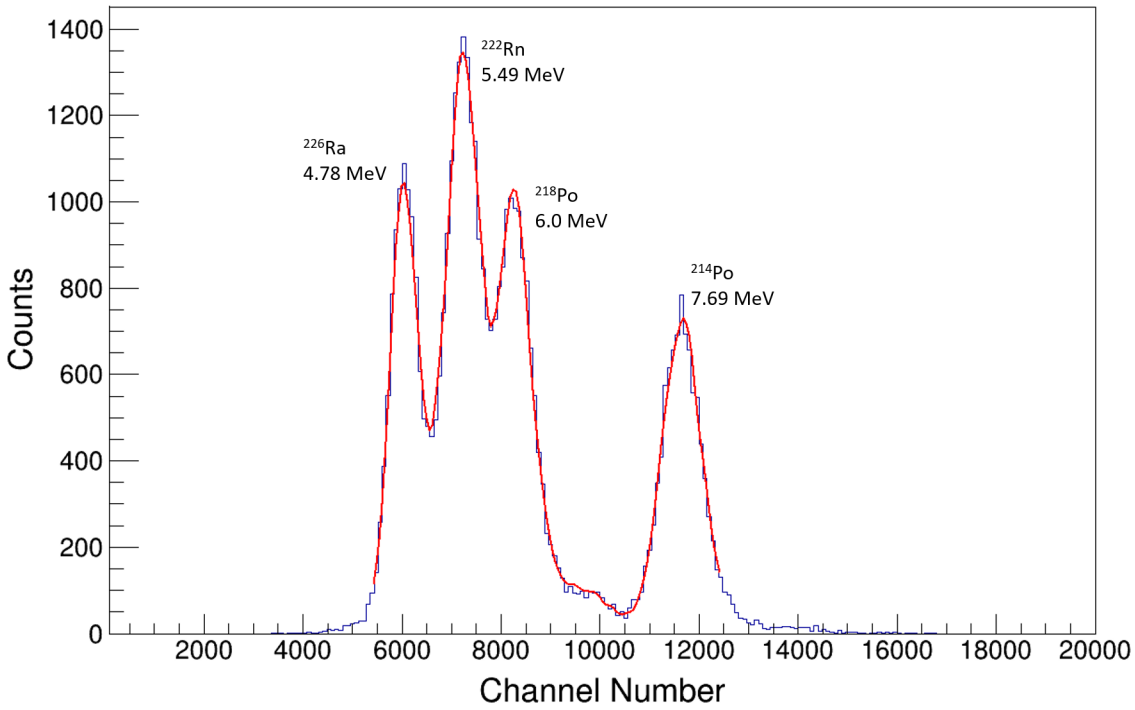

Figure 4.6: Alpha decay spectra of one crystal and representation of the fit used for crystal-by-crystal calibration.

The measured neutron yield from the silicon beam monitor and the cross section of ^{6}Li(n, α)^{3}H are shown in Figure 4.7. For each neutron energy bin, the yield measured by the silicon beam monitor was divided by the ENDF/B-VII.1 evaluated ^{6}Li(n, α)^{3}H cross section to deduce the neutron fluence [96]. The ^{6}Li(n, α)^{3}H cross section is smooth up to a broad, high energy resonance at approximately 240 keV, which can complicate the fluence characterization in that energy region. Therefore, the neutron fluence deduced from the ^{6}Li beam monitor was used to define the full neutron fluence from 1 eV to 5 keV.

The measured neutron yield from the ^{235}U beam monitor and the cross section of ^{235}U(n, f) are shown in Figure 4.8. For each neutron energy bin, the yield measured by the fission chamber was divided by the ENDF/B-VII.1 evaluated ^{235}U(n, f) cross section to deduce the neutron fluence [96]. Since the ^{235}U(n, f) cross section is smoother at higher energies, this calculation was used to define the neutron fluence from 20 keV to 1 MeV. The neutron

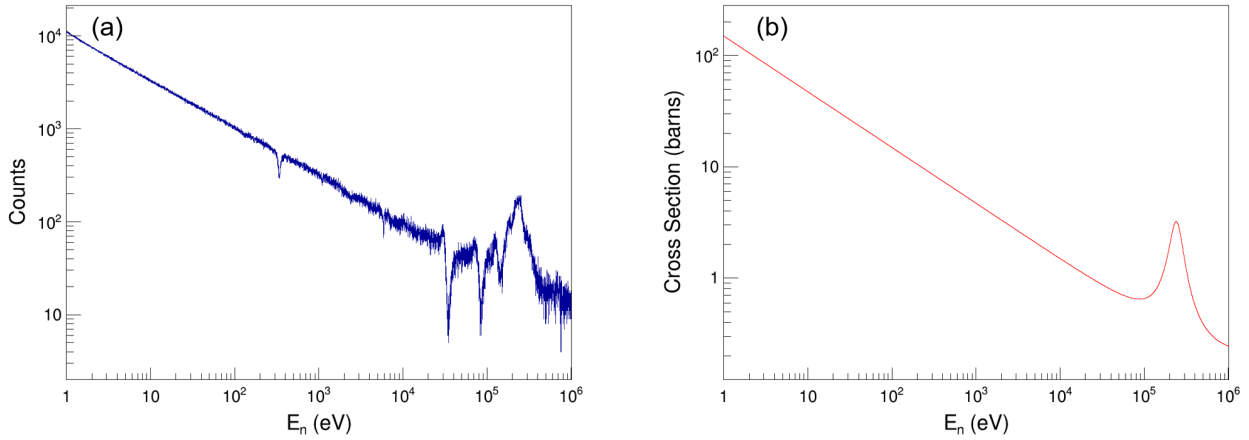

Figure 4.7: (a) Neutron yield measured by the ^{6}Li beam monitor. (b) ENDF/B-VII.1 evaluated cross section of ^{6}Li(n, α)^{3}H used in the neutron fluence determination.

fluences deduced from each beam monitor were then combined together to characterize the neutron fluence over the full energy range. The neutron fluence from the silicon monitor is scaled to the neutron fluence from the fission chamber in the energy region of 5 keV to 20 keV. The neutron fluence in the region of 5 keV to 20 keV is represented by an average of the neutron fluence from each monitor. This fluence is shown in Figure 4.9. The dips that are visible in the neutron fluence are from capture on aluminum and manganese components in the beam line, both of which have a few strong resonances.

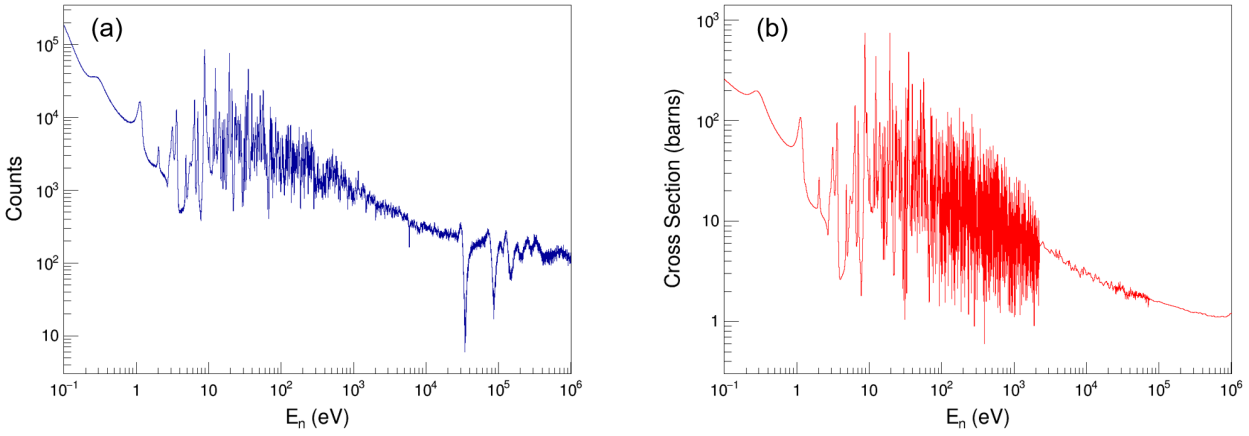

Figure 4.8: (a) Neutron yield measured by the gas-filled ^{235}U fission chamber. (b) ENDF/B-VII.1 evaluated cross section of ^{235}U(n, f) used in the neutron fluence determination.

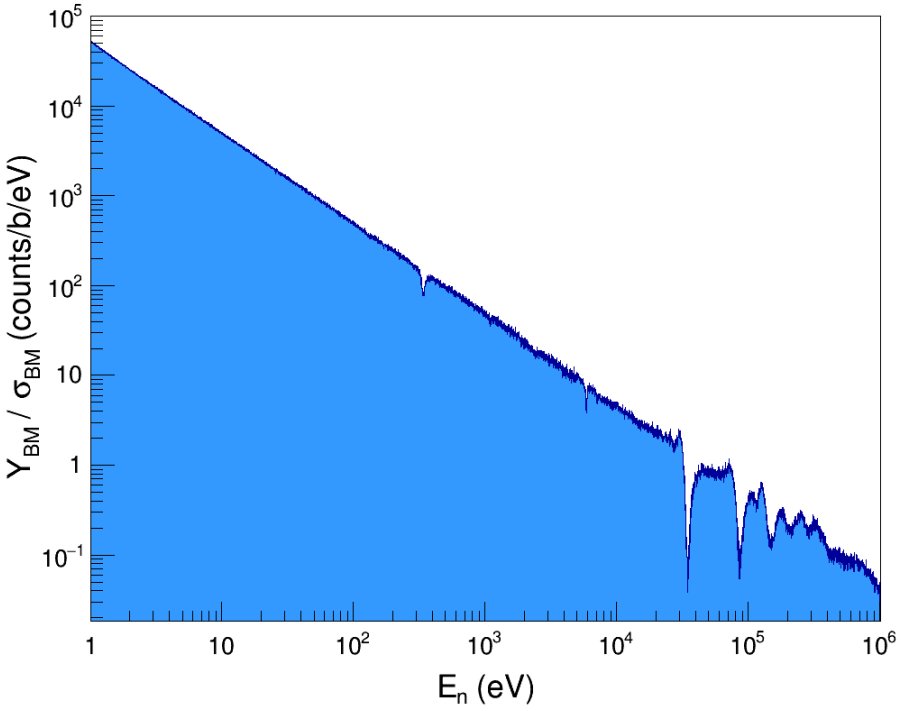

Figure 4.9: Neutron fluence at the beam monitor position as a function of neutron energy.

However, the neutron fluence at the beam monitor position is lower than the fluence at the target positions in the center of DANCE, due to the divergence of the beam. To account for this, a normalization constant, κ, is introduced. This allows for the determination of the neutron fluence at the target position, $\Phi^{(0)}$, from the beam monitor data, as shown in Equation 4.3.

$$\Phi^0(E_n) = \kappa \frac{Y_{BM}(E_n)}{\sigma_{BM}(E_n)} \tag{4.3}$$

The normalization constant κ is determined from the measurement of neutron capture on ^{197}Au, which will be discussed in the following section.

4.4.1 Normalization to ^{197}Au

The well known neutron-capture cross section of ^{197}Au is utilized to normalize the neutron fluence at the beam monitor position for the determination of the neutron fluence expected

at the target position. The nuclide ^{197}Au has a strong neutron capture resonance at 4.89 eV, with a peak cross section of 27 kilobarns. The E_{Sum} vs. E_n spectrum measured by DANCE over this energy region is shown in Figure 4.10. The yield of neutron captures on the ^{197}Au target in a neutron energy bin $Y^{Au}_{n,\gamma}(E_n)$ is related to the ^{197}Au(n,γ) cross section by:

$$Y^{Au}_{n,\gamma}(E_n) = \Phi(E_n) N_{Au} \sigma^{Au}_{n,\gamma}(E_n) \tag{4.4}$$

where N_{Au} is the number of Au atoms in the target, and $\Phi(E_n)$ is the number of neutrons per barn for that neutron energy bin. The thickness of the ^{197}Au target was determined via Rutherford backscattering and used to determined the number of Au atoms in the target, with a 4% uncertainty. Substituting in Equation 4.3 for $\Phi(E_n)$, and rearranging and solving for $\sigma^{Au}_{n,\gamma}$, the following equation is obtained,

$$\sigma^{Au}_{n,\gamma}(E_n) = \frac{1}{\kappa} \frac{Y^{Au}_{n,\gamma}(E_n)}{N_{Au}} \frac{\sigma_{BM}(E_n)}{Y_{BM}(E_n)}. \tag{4.5}$$

Ultimately, using the known cross section of ^{197}Au(n,γ) from ENDF/B-VII.1 [96], the normalization constant κ can be extracted. However, the proper subtraction of low energy background in the ^{197}Au spectra is needed to ensure that the true number of neutron captures on ^{197}Au is being used.

In the low energy region of the 4.89 eV resonance, not all of the counts are from neutron capture events. There is some contribution to the background from neutrons scattering off the ^{197}Au target. The background is mostly suppressed by the LiH sphere between DANCE and the target position, and thus can be neglected. The dominant background is resulting mainly from the decay of neutron induced reaction products, random coincidences, and the ambient neutron background. This background is assumed to be linear in relation to TOF in

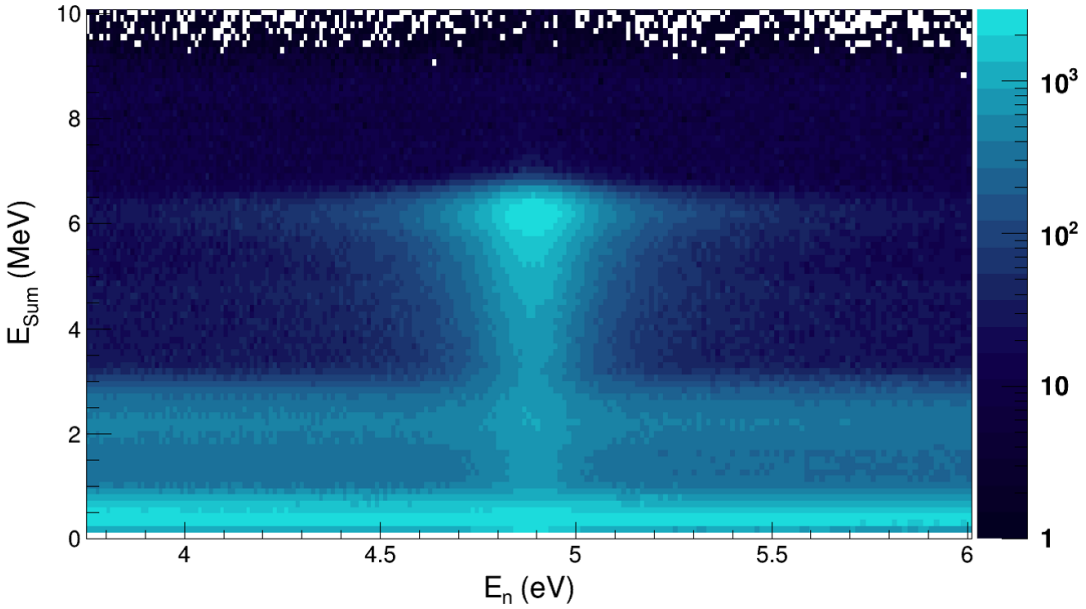

Figure 4.10: 2D plot of E_{Sum} as a function of E_n for the ^{197}Au data, over the 4.89 eV resonance.

the region of the ^{197}Au resonance. Therefore, the background in two off-resonance regions on either side of the resonance were used to determine a linear background, with the slope and offset parameters left as free parameters. The result of this linear background subtraction is shown in Figure 4.11. A diagnostic plot of the E_{Sum} projections of the background region and the region over the resonance, as well as the resulting capture E_{Sum} shape, are shown in Figure 4.12. In this diagnostic plot, it is evident that there is some contribution from neutron capture in the background region, indicated by the small peak around the Q-value of ^{197}Au. However, the effect of this is negligible. The background subtracted time-of-flight yield spectrum was then converted into a neutron energy spectrum via Equation 4.1.

With the yield of neutron capture on ^{197}Au determined, the known cross section is scaled to the experimental cross section, and $\kappa N_{Au} = 0.308$ is extracted as the scaling factor, as shown in Figure 4.13. With the number of Au atoms known, the normalization constant κ can be determined and used in the analysis of the ^{82}Se data. The dominant source of uncertainty

in the determination of κN_{Au} is a 4% systematic uncertainty from the number of gold atoms determined via Rutherford backscattering. Compared to this systematic uncertainty, the statistical uncertainty of κN_{Au} is negligible.

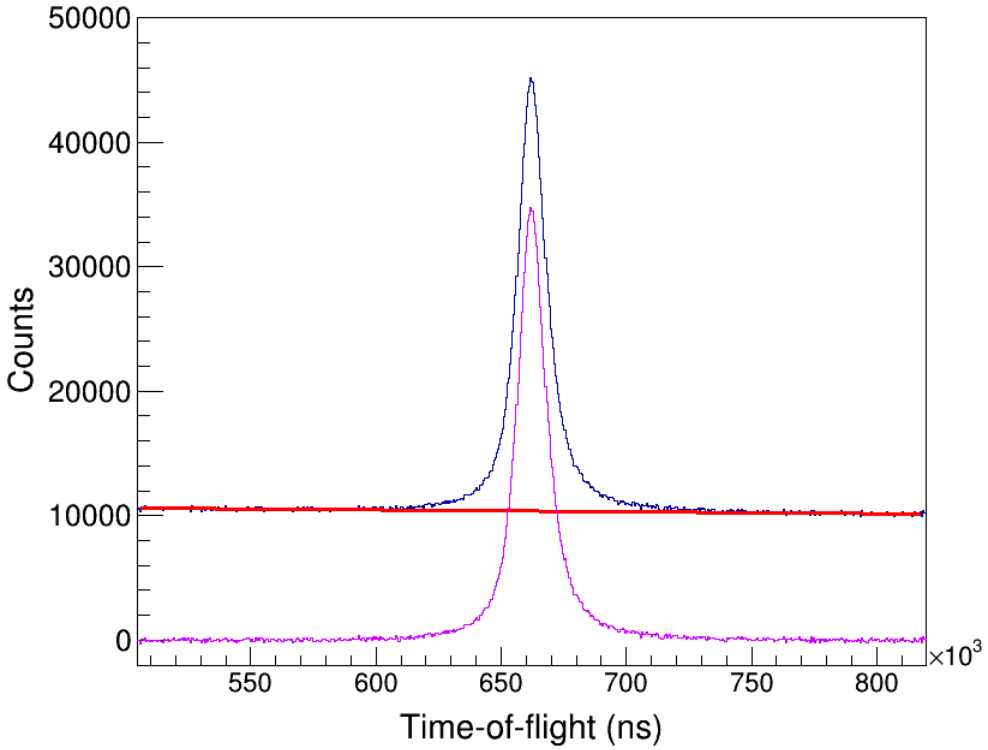

Figure 4.11: Figure depicting the subtraction of a linear background from the time-of-flight spectrum of neutron capture on ^{197}Au. The blue histogram is the data pre-subtraction, and the magenta histogram is the data after subtraction of the linear background, shown in red.

4.5 ^{82}Se Data Analysis

The neutron-capture cross section is determined using the following equation:

$$\sigma_{n\gamma}(E_n) = \frac{1}{\epsilon_{cut}} \frac{Y^{82}_{n,\gamma}(E_n)}{N_{82}} \underbrace{\left(\frac{\sigma_{BM}(E_n)}{\kappa Y_{BM}(E_n)} \right)}_{(\Phi^0(E_n))^{-1}} \tag{4.6}$$

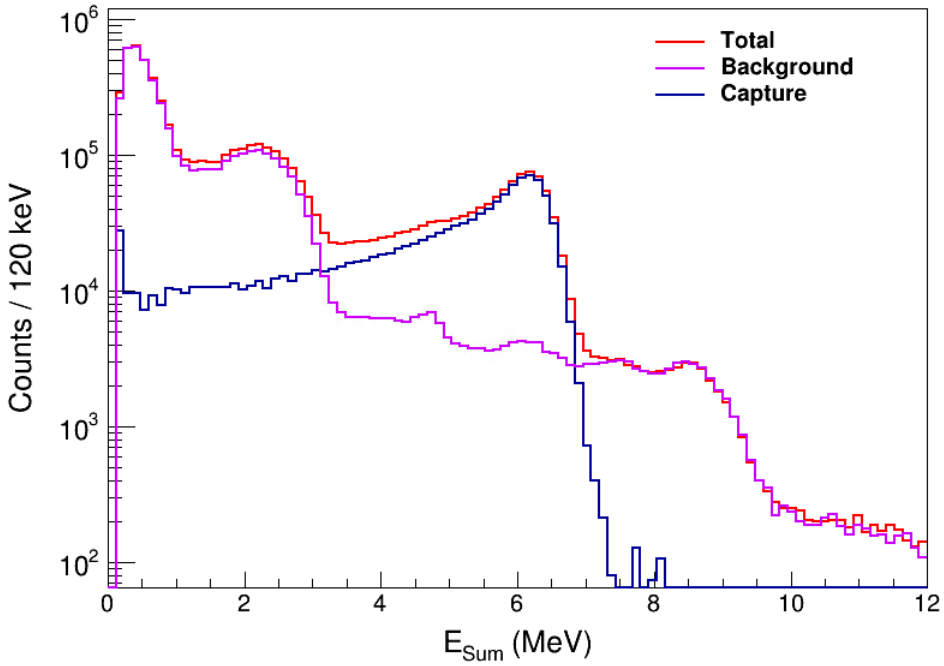

Figure 4.12: Diagnostic plot showing the E_{Sum} projections of the different components of the background subtraction on the 4.89 eV ^{197}Au resonance. The total E_{Sum} shape (red) corresponds to the data before the background subtraction was performed. The magenta E_{Sum} shape corresponds to the sum of the background regions on either side of the resonance. The blue E_{Sum} shape is the background subtracted capture E_{Sum}.

where $Y^{82}_{n,\gamma}(E_n)$ is the yield of ^{82}Se neutron-capture events in each neutron energy bin, N_{82} is the number of atoms of ^{82}Se in the target, ϵ_{cut} is the efficiency of DANCE in the E_{Sum} and multiplicity cut chosen, and Φ^0 is the neutron fluence normalized to the target position. The determination of the normalized neutron fluence was previously discussed in Section 4.4; this section will discuss the determination of the yield of neutron capture events after background subtraction (Section 4.5.1) as well as the determination of the efficiency in the E_{Sum} and multiplicity cut (Section 4.5.2).

4.5.1 Background Subtraction

The raw ^{82}Se(n,γ) data are shown in Figure 4.14, with total energy, E_{Sum}, plotted on the y-axis and neutron energy, E_n, plotted on the x-axis. The z-axis shows the number of counts

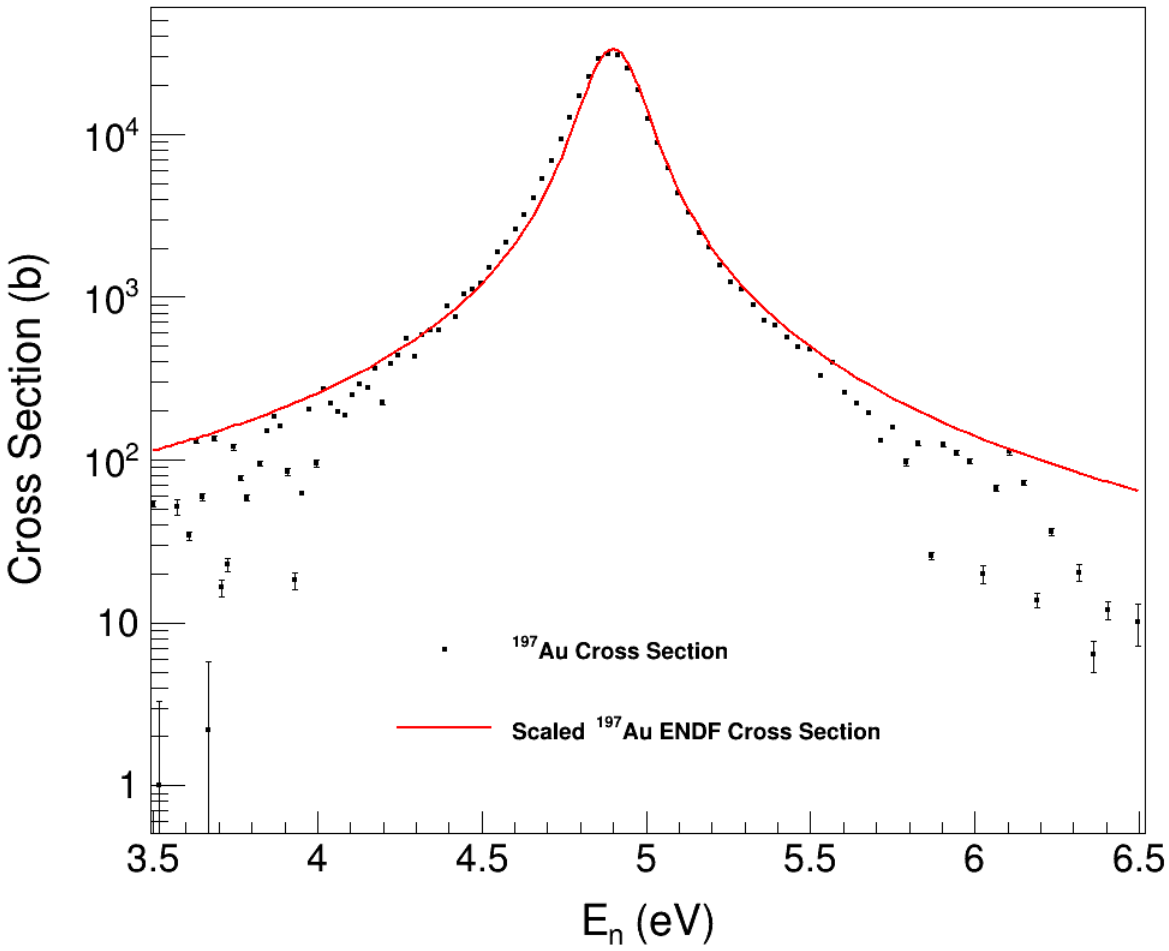

Figure 4.13: Cross section of neutron capture on ^{197}Au, in the region of the 4.89 eV resonance (black squares). The scaled ENDF/B-VII.1 cross section is shown in red [96].

for each bin of E_{Sum} and E_n. Resonances expected from neutron capture on ^{82}Se are visible above 3 keV, with an E_{Sum} distribution peaking around 5.8 MeV (^{82}Se (n, γ) Q-value = 5.82 MeV). Due to incomplete summing of all γ rays, the E_{Sum} distribution extends to lower energies. Along with the ^{82}Se resonances, there are other resonances that show up at E_{Sum} values corresponding to the Q-values of other Se isotopes, namely ^{80}Se (Q-value = 6.70 MeV), ^{78}Se (Q-value = 6.96 MeV), ^{74}Se (Q-value = 8.04 MeV), and ^{77}Se (Q-value = 10.5 MeV). There are also several horizontal bands visible in Figure 4.14. These are from neutron capture induced in the BaF_2 crystals of DANCE due to neutrons that scatter off

of the target. The neutron capture on BaF_2 will appear at E_{Sum} values corresponding to the Q-values of barium isotopes. While the background attributed to scattered neutrons is greatly reduced by the ^{6}LiH shell, it does not absorb 100% of the scattered neutrons, so the scattering background needs to be characterized and removed.

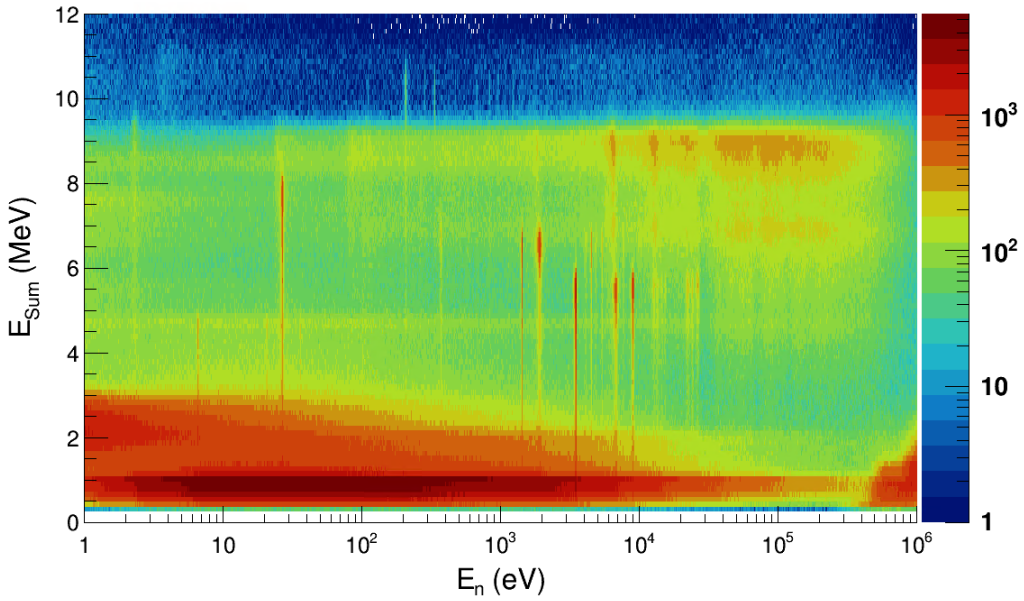

Figure 4.14: Counts as a function of the sum of energy deposited in DANCE (E_{Sum}) and neutron energy (E_n) for the ^{82}Se data.

4.5.1.1 Scattering Background

Neutrons incident on the targets used in this experiment have a probability of scattering off the target instead of capturing. These scattered neutrons may then capture on the barium in the DANCE detectors, which leads to signatures corresponding to E_{Sum} values of barium isotopes. This scattering background is characterized using a ^{208}Pb target. The nuclide ^{208}Pb is used for this characterization due to its relatively low neutron-capture cross section, relatively high neutron elastic scattering cross section, and low Q-value of ^{208}Pb(n, γ) (3.94 MeV).

The raw data from running with the ^{208}Pb target are shown in Figure 4.15. For each neutron energy bin, an E_{Sum} projection was made for both the Se data and the ^{208}Pb data, and the ^{208}Pb projection was normalized to the Se data using the normalization factor, α_{Pb}. The normalization parameter is described in Equation 4.7, where C indicates the yield of the respective isotope.

$$\alpha_{Pb}(E_n) = \frac{\int_{8.6MeV}^{9.3MeV} C_{Se}(E_n, E_{Sum})dE_{Sum}}{\int_{8.6MeV}^{9.3MeV} C_{Pb}(E_n, E_{Sum})dE_{Sum}} \tag{4.7}$$

The E_{Sum} peak at approximately 9 MeV corresponds to neutron capture on ^{135}Ba, and is used for normalization since this E_{Sum} region does not have contributions from other isotopes present in the Se sample. After normalization, the scattering contribution characterized by the ^{208}Pb is subtracted from the raw Se data. An example of this subtraction procedure for a neutron energy bin on a ^{82}Se resonance is shown in Figure 4.16. The full 2D E_{Sum},E_n plot after the scattering background has been removed from each neutron energy bin is shown in Figure 4.17.

4.5.1.2 Target contaminants

One of the key abilities of DANCE is the capability to distinguish events from different reactions based on the reaction Q-value. The ability to distinguish events is attributed to the fact that DANCE has a high efficiency for detecting the total energy (E_{Sum}) of the γ-ray cascades released following neutron capture. As discussed previously, there are several resonances observed that, based on their E_{Sum} value, correspond to other stable selenium isotopes present in the target. To remove these contaminates, a step wise subtraction was performed.

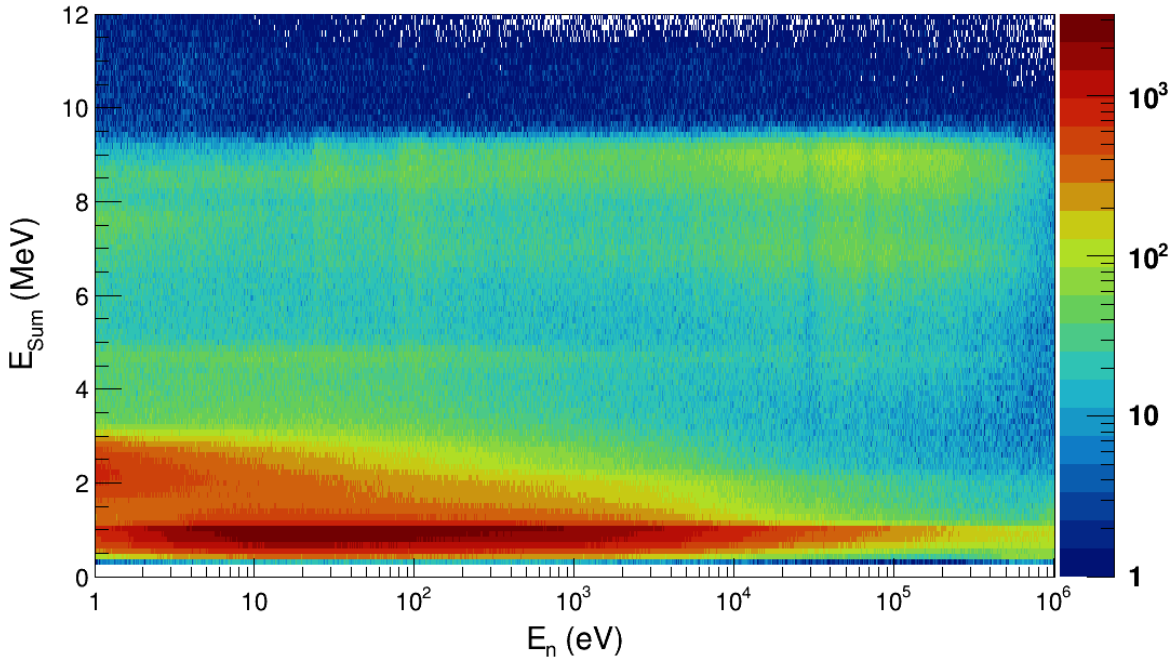

Figure 4.15: Counts as a function of the sum of energy deposited in DANCE (E_{Sum}) and neutron energy (E_n) for the ^{208}Pb data.

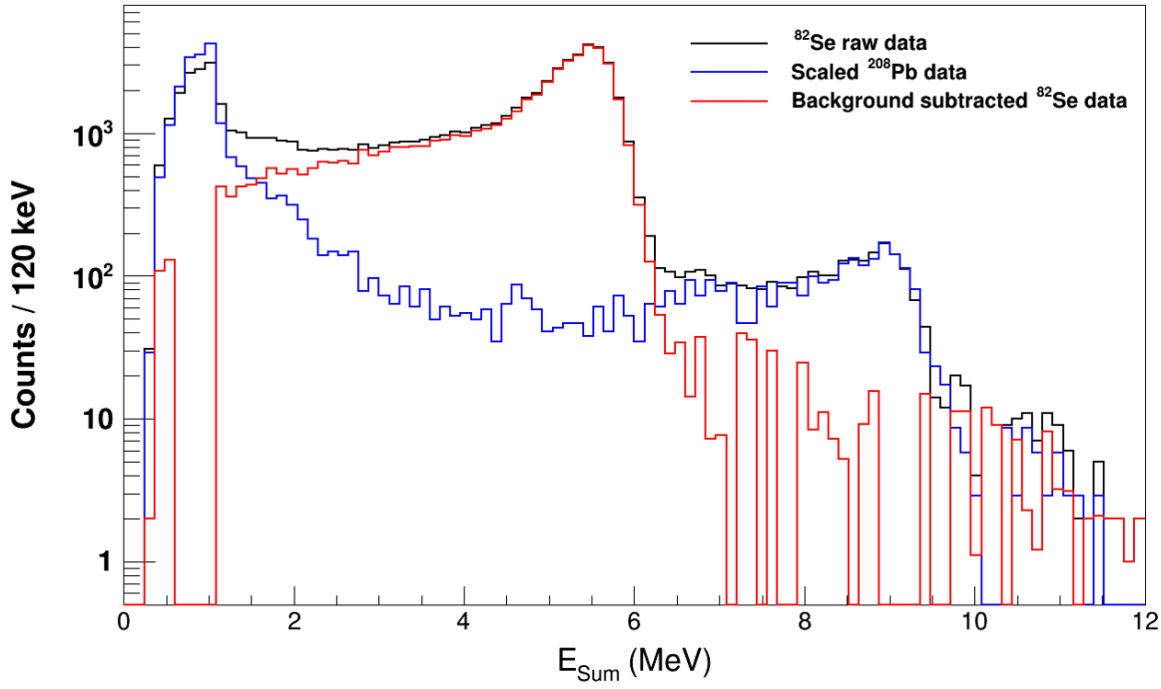

Figure 4.16: Example scattering background subtraction for a single E_n bin on a ^{82}Se resonance.

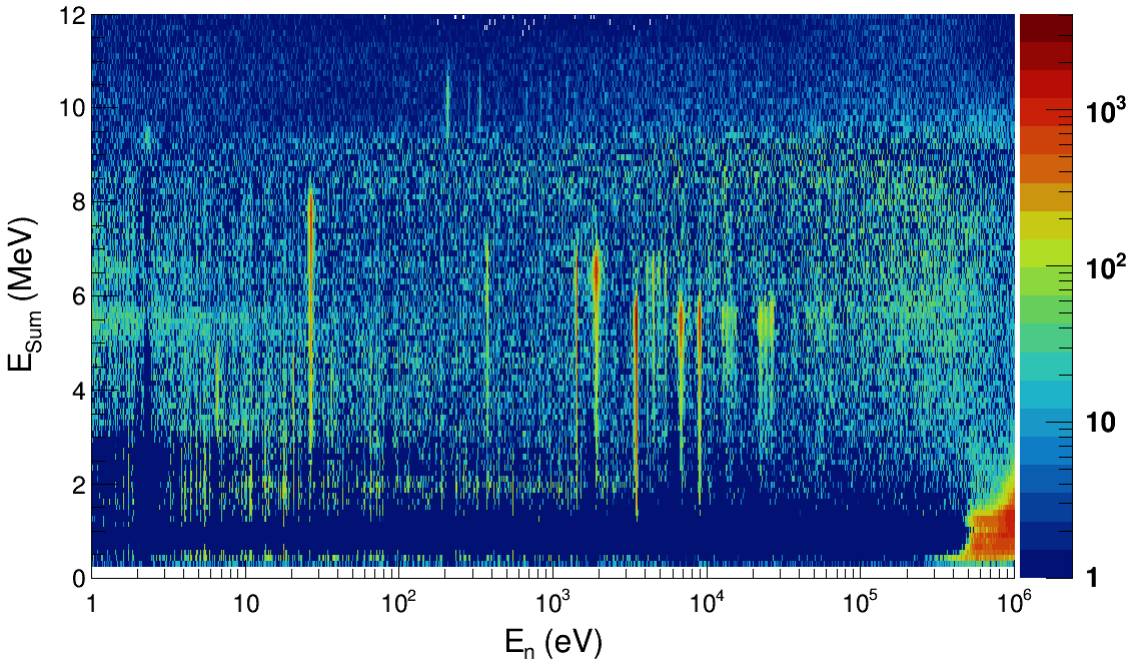

Figure 4.17: Counts as a function of the sum of energy deposited in DANCE (E_{Sum}) and neutron energy (E_n) for the ^{82}Se data, after the scattering background was subtracted.

For each isotope identified in the E_{Sum} vs. E_n spectra, an E_{Sum} gate was placed to obtain the neutron capture yield spectra for that isotope. The range of each gate is summarized in Table 4.2. Due to incomplete summing of some γ-ray cascades, the E_{Sum} distribution of each isotope will extend to lower energies. Therefore, many of the isotopes have contributions that appear in the E_{Sum} gated spectra of other isotopes. As an example, the ^{82}Se E_{Sum} gated spectrum is shown in Figure 4.18. Observed resonances from other isotopes are labeled. To characterize this contribution of each isotope to the E_{Sum} gated spectra of the other isotopes, a strong resonance was chosen: 211.7 eV for ^{77}Se, 27.13 eV for ^{74}Se, 383 eV for ^{78}Se, and 1970 eV for ^{80}Se. Projections were made for each of these strong resonances and shown in Figure 4.19. From the projection representing each isotope, integrals were taken over each E_{Sum} range to determine the contribution of that isotope in the spectra of each other isotope. From these integrals, scaling factors were determined for the subsequent subtractions. The subtractions proceeded in an order beginning with the

isotope with the largest Q-value, ^{77}Se. The contribution of ^{77}Se was subtracted from the spectra of ^{74}Se, ^{78}Se, ^{80}Se, and ^{82}Se. The (now isolated) spectra of ^{74}Se, which has the next largest Q-value, was then subtracted from each of the following in the same manner. This step was repeated for each isotope, until all were removed from the spectrum of ^{82}Se.

Table 4.2: E_{Sum} gate used for each isotope identified in the ^{82}Se target data.

Isotope	E_{Sum} Gate (MeV)
^{77}Se	9.3 - 11.0
^{74}Se	7.7 - 8.6
^{78}Se	6.8 - 7.7
^{80}Se	6.4 - 6.8
^{82}Se	5.0 - 5.9

To describe this method in more detail, the subtraction of each isotope from the ^{82}Se spectrum will be discussed. The subtraction of ^{77}Se from ^{82}Se will not be shown here, as its contribution is negligible and is not observed in the spectrum of ^{82}Se. To begin with, the spectrum of ^{74}Se, gated on an E_{Sum} range of 7.7 - 8.6 MeV, is shown in Figure 4.20. This spectrum was scaled by $\alpha_{74}(E_n)$, as determined by

$$\alpha_{74}(E_n) = \frac{\int_{5.0MeV}^{5.9MeV} C_{74}(E_n, E_{Sum})dE_{Sum}}{\int_{7.7MeV}^{8.6MeV} C_{74}(E_n, E_{Sum})dE_{Sum}}, \tag{4.8}$$

where the integrals are taken from the ^{74}Se E_{Sum} projection shown in panel (b) of Figure 4.19. After being scaled, the ^{74}Se spectrum was subtracted from the ^{82}Se spectrum, to obtain the spectrum shown in Figure 4.21. The spectrum of the next isotope to be removed, ^{78}Se, is shown in Figure 4.22. The scaling factor was determined in the same manner as previously described, using the ^{78}Se E_{Sum} projection shown in panel (c) of Figure 4.19, and

Equation 4.9.

$$\alpha_{78}(E_n) = \frac{\int_{5.0MeV}^{5.9MeV} C_{78}(E_n, E_{Sum})dE_{Sum}}{\int_{6.8MeV}^{7.7MeV} C_{78}(E_n, E_{Sum})dE_{Sum}} \tag{4.9}$$

The scaled ^{78}Se spectrum was then subtracted from the ^{82}Se spectrum to obtain Figure 4.23. The final isotope, ^{80}Se, was subtracted in the same manner. The spectrum of ^{80}Se is shown in Figure 4.24, and the E_{Sum} projection is shown in panel (d) of Figure 4.19. The scaling factor was determined via,

$$\alpha_{80}(E_n) = \frac{\int_{5.0MeV}^{5.9MeV} C_{80}(E_n, E_{Sum})dE_{Sum}}{\int_{6.4MeV}^{6.8MeV} C_{80}(E_n, E_{Sum})dE_{Sum}}, \tag{4.10}$$

and the ^{82}Se spectrum with the scaled ^{80}Se spectrum subtracted (shown in Figure 4.25), is the final yield of neutron capture on ^{82}Se. There is a slight over-subtraction of the 1970 eV resonance of ^{80}Se and an under-subtraction of the 1482 eV resonance of ^{80}Se, which could possibly be due to the scattering cross section of the higher energy resonance, which would cause the peak to be smaller than predicted by the scaling.

4.5.2 Efficiency Determination

To enhance the signal-to-noise ratio of the data, several gates are made in software. Events with a multiplicity of 1 are excluded due to an unfavorable signal-to-noise ratio. Events with a multiplicity of 6 and above are excluded as there are not enough statistics available to characterize the events. Therefore, for the ^{82}Se data, events with multiplicities from 2 to 5 were used. A gate was also placed on the E_{Sum}, as the E_{Sum} distribution should only go up to the Q-value of ^{82}Se (5.818 MeV). For the ^{82}Se data, total energies of 5.0 MeV to 5.9 MeV were used. While these gates enhance the signal-to-noise ratio, it comes at the cost

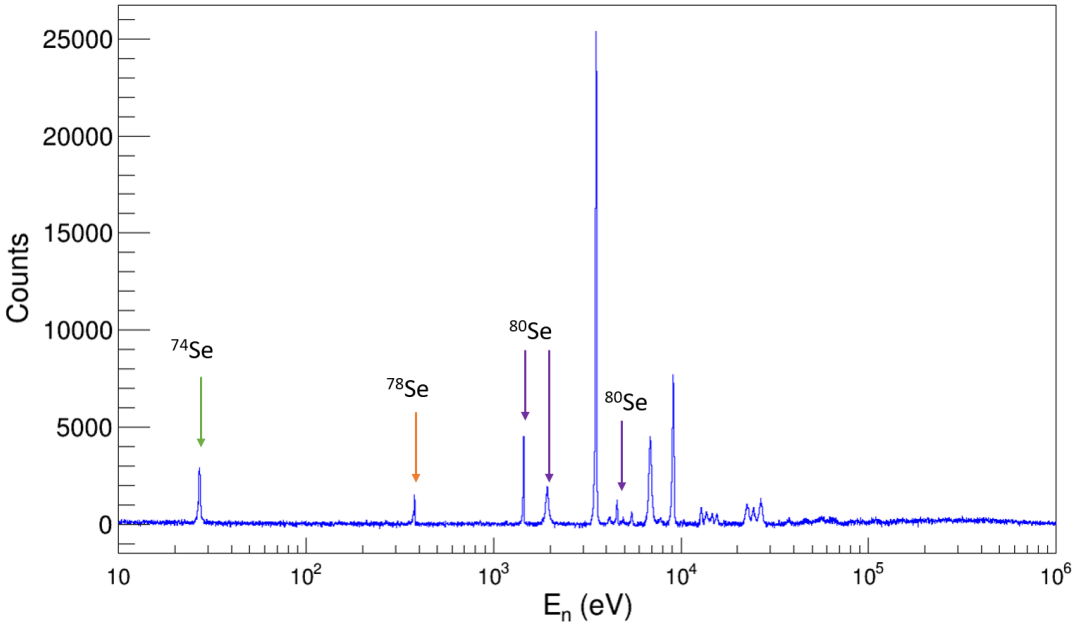

Figure 4.18: Yield of neutron capture on ^{82}Se, gated on an E_{Sum} range of 5.0 - 5.9 MeV. Contributions of resonances from other Se isotopes are labeled.

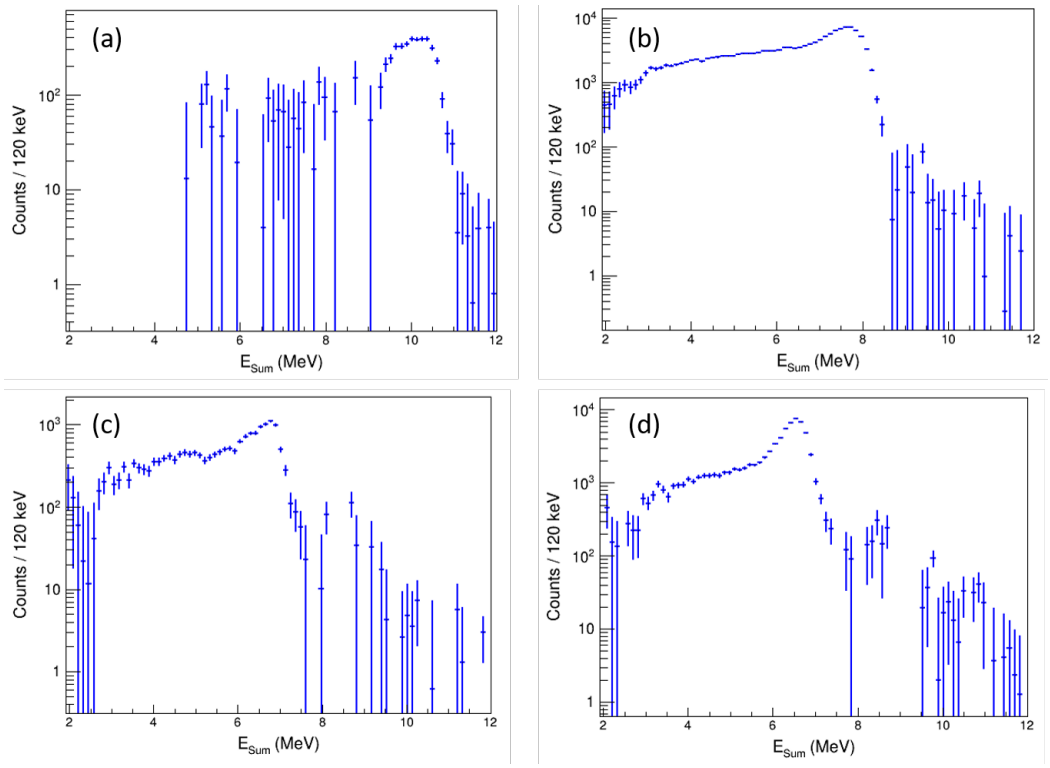

Figure 4.19: E_{Sum} projection of (a) ^{77}Se (b) ^{74}Se (c) ^{78}Se and (d) ^{80}Se

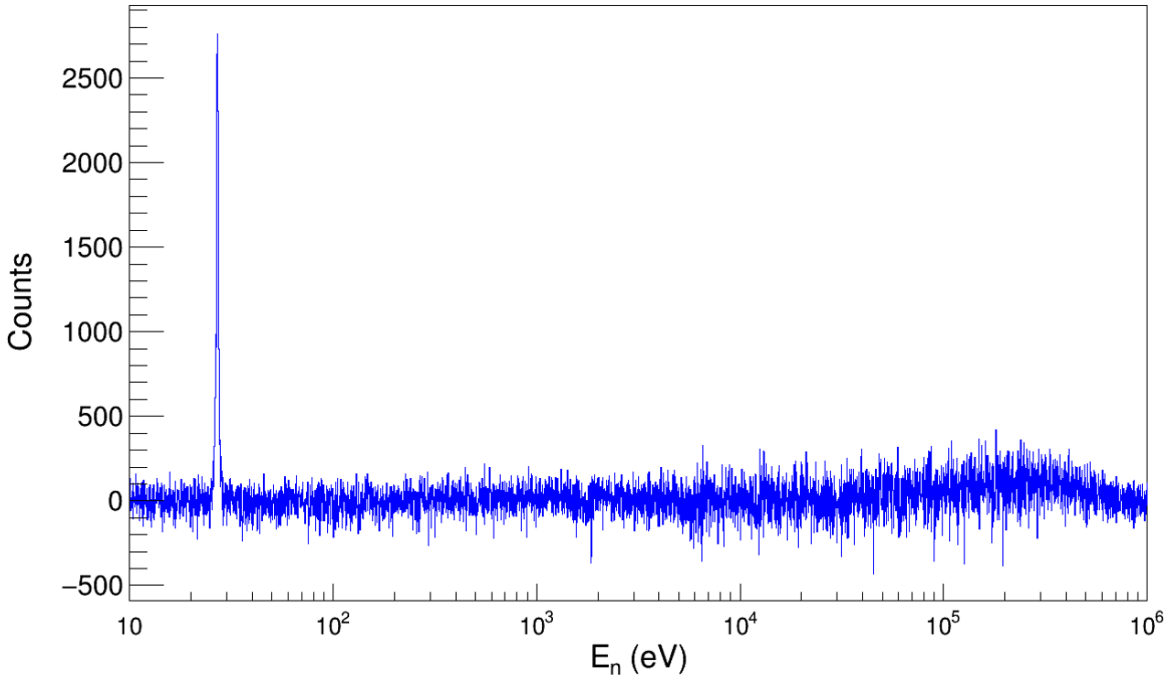

Figure 4.20: Spectra of ^{74}Se (with ^{77}Se contributions removed) gated on an E_{Sum} range of 7.7 - 8.6 MeV.

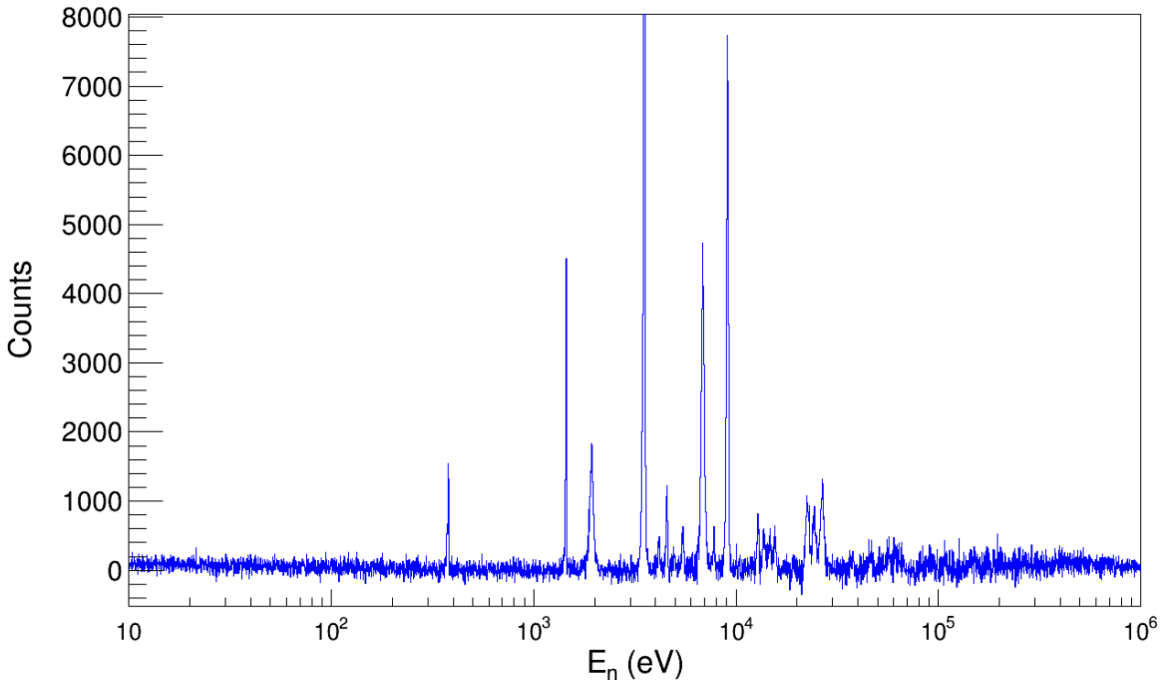

Figure 4.21: Yield of neutron capture on ^{82}Se, gated on an E_{Sum} range of 5.0 - 5.9 MeV, after the contribution from ^{74}Se has been subtracted.

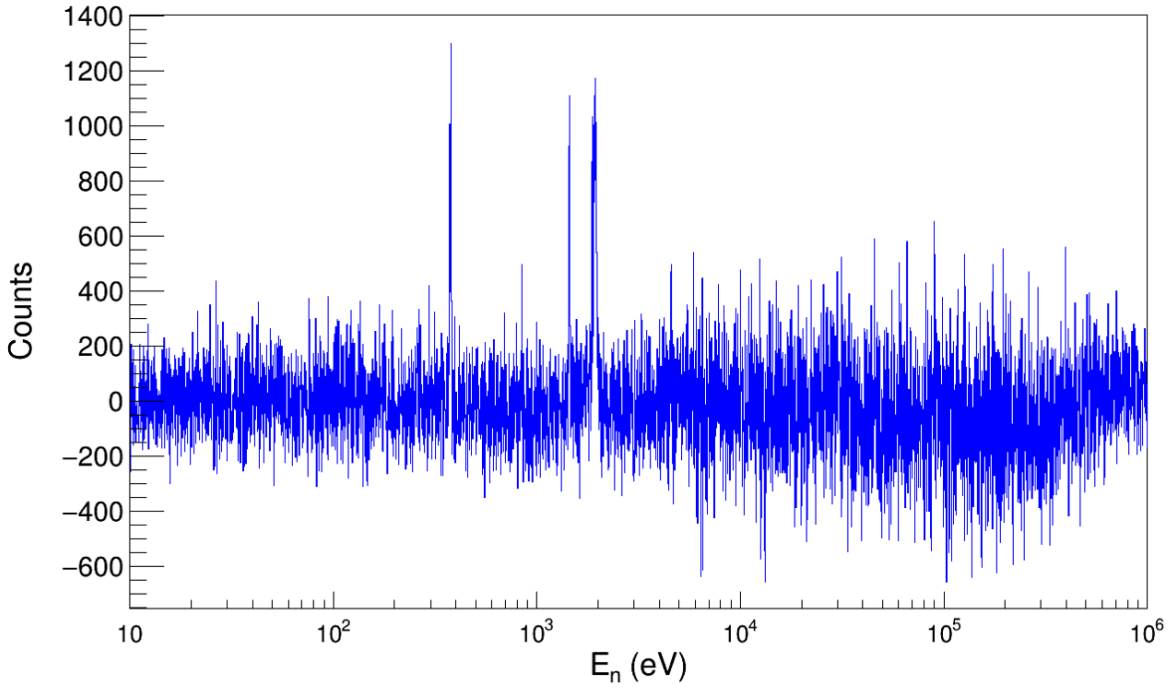

Figure 4.22: Spectra of ^{78}Se (with ^{77}Se and ^{74}Se contributions removed) gated on an E_{Sum} range of 6.8 - 7.7 MeV.

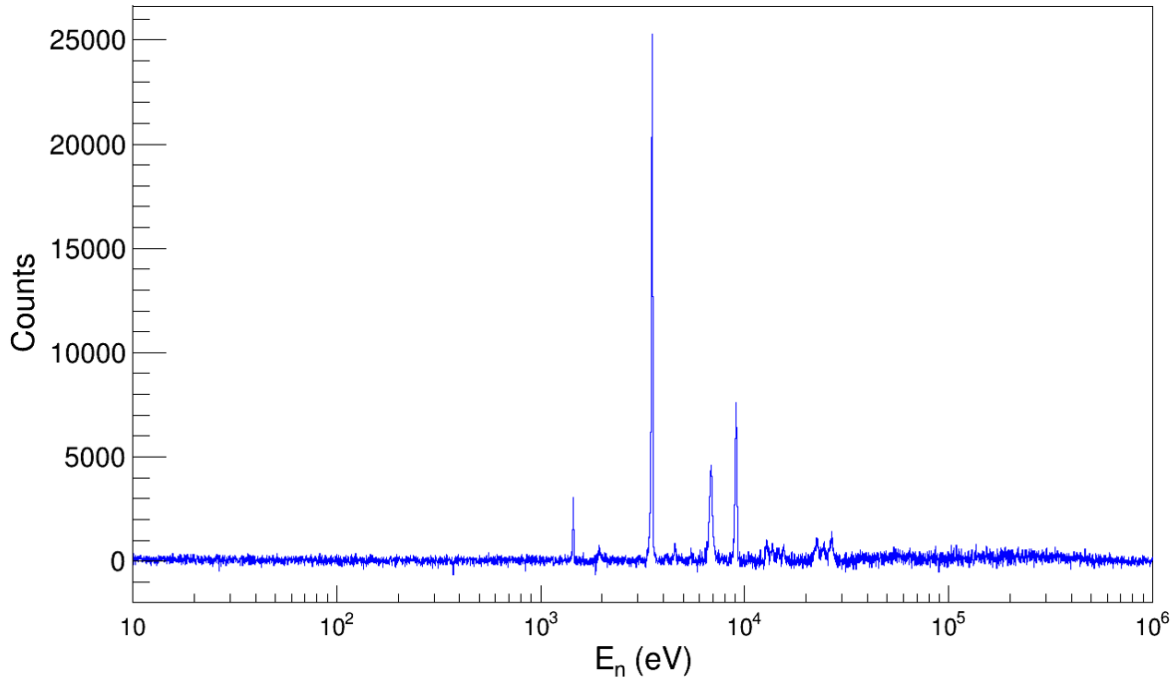

Figure 4.23: Yield of neutron capture on ^{82}Se, gated on an E_{Sum} range of 5.0 - 5.9 MeV, after the contributions from ^{74}Se and ^{74}Se have been subtracted.

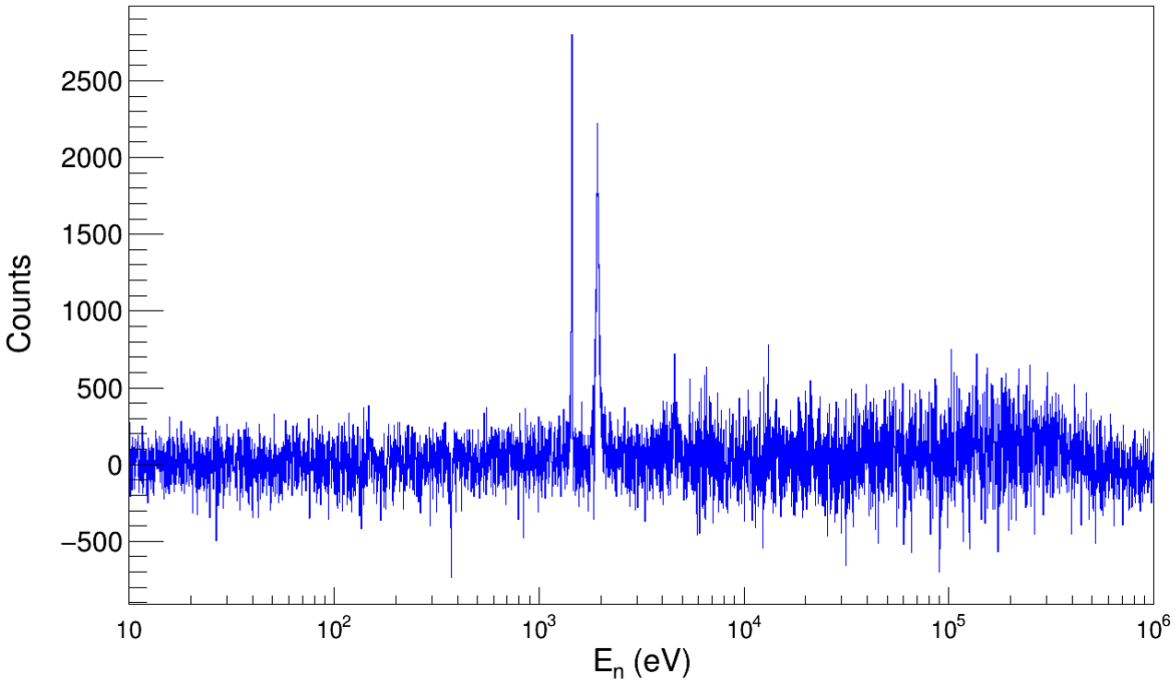

Figure 4.24: Spectra of ^{80}Se (with ^{77}Se, ^{74}Se, and ^{78}Se contributions removed) gated on an E_{Sum} range of 6.4 - 6.8 MeV.

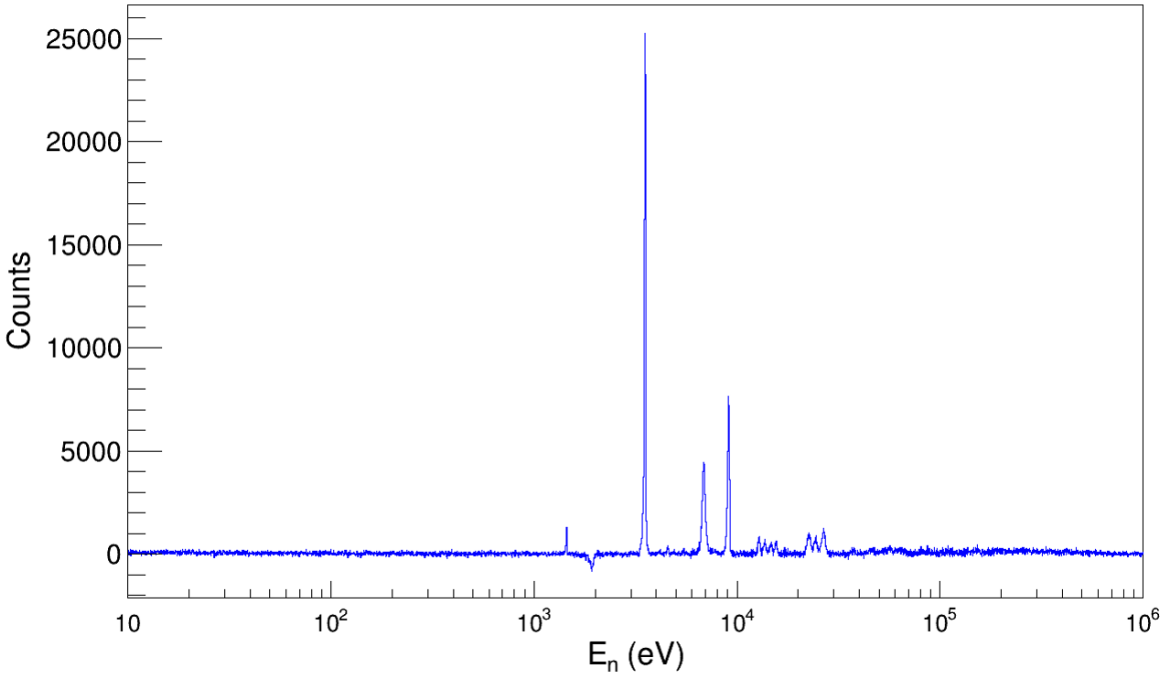

Figure 4.25: Yield of neutron capture on ^{82}Se, gated on an E_{Sum} range of 5.0 - 5.9 MeV, after the contributions from ^{74}Se, ^{78}Se and ^{80}Se have been subtracted.

of losing valid events. Therefore, an efficiency of these cuts (ε_{cut}) is determined to account for the lost counts by determining the ratio of events counted within these gates to the true number of neutron captures. The multiplicity and E_{Sum} gates were chosen to minimize the uncertainty on ε_{cut}.

Due to a strong dependence on the properties of the γ-ray cascades emitted after neutron capture, such as the energy and multiplicity distribution, the efficiency was determined through simulations. Ultimately, the energy and multiplicity distribution depend on the characteristics of the nucleus formed in neutron capture, in this case, ^{83}Se, and the resonances populated through neutron capture. The γ-ray cascades also depend strongly on the spin and parity of the resonances. One of the strongest ^{83}Se resonances observed (at an energy of 6580 eV) has an assigned spin and parity of $\frac{1}{2}+$, while the other two strongest resonances observed (at energies of 3630 eV and 9508 eV) have tentative negative parity assigned, but do not have a spin assigned [82]. Based on selection rules, the spin of these two resonances can be assumed to be either $\frac{1}{2}$ or $\frac{3}{2}$. Therefore, simulations were performed for $J^\pi = \frac{1}{2}+$, $\frac{1}{2}-$, and $\frac{3}{2}-$.

Cascades of γ rays following neutron capture were simulated using the DICEBOX program [97]. Below a certain energy, E_{crit} (1.85 MeV for ^{83}Se), the known levels and transitions are used, as the level scheme is assumed to be complete. Above E_{crit}, a statistical model is used to determine levels and transition probabilities to generate simulated cascades. A nuclear level density model is chosen and used to generate the levels, while the transition probabilities are calculated from the partial radiative widths via:

$$\Gamma_{i,f} = \sum_{XL} y_{XL}^2 (E_i - E_f)^{2L+1} \frac{f_{XL}(E_i - E_f)}{\rho(E_i, J_i^\pi)}, \tag{4.11}$$

where f_{XL} is the chosen γ-ray strength function model for the transition type X (electric E or magnetic M) and multipolarity L, $\rho(E_i, J_i^\pi)$ is the nuclear level density at the initial excitation energy E_i, and y_{XL}^2 is a random value independent of the normal distribution, with a zero mean and a unit variance. For ^{83}Se, the Constant Temperature model was chosen for the nuclear level density, and the generalized Lorentzian model was chosen for the γ-ray strength function to be consistent with the models utilized in the β-Oslo analysis described in Chapter 3. Both of these models have previously been described in Chapter 1.

For each spin and parity, 30 simulated systems (referred to here as realizations) with 100,000 cascades each were generated. Each realization is a different system of levels and decay probabilities. These simulated cascades were then used as input in a Geant4 detector simulation and then analyzed using the same conditions under which the ^{82}Se data was analyzed. The total energy, E_{Sum}, distribution and the individual γ-ray spectra, or Multi-Step Cascade (MSC) spectra, were averaged over all 30 simulations and compared to the experimental data to validate the simulations and choice of NLD and γSF models. Comparisons of MSC spectra from the simulations and from three strong resonances, gated on multiplicities 2, 3, 4 and 5, are shown in Figures 4.26 - 4.29.

As stated before, the uncertainty of the efficiency was taken into account when choosing the range of the E_{Sum} gate. A study of the average efficiency across all 30 realizations and the standard deviation as a function of the lower boundary of the E_{Sum} gate is shown in Figure 4.30. The lower E_{Sum} boundary of 5.0 MeV was chosen to keep the uncertainty of the efficiency to a relative minimum. Therefore, for $< M > =$ [2,5] and 5.0 MeV $> E_{Sum} >$ 5.9 MeV, efficiencies were calculated, and are shown in Table 4.3. A global average was taken over all simulations to obtain an average efficiency of 0.422 ± 0.038. A global average is used to represent all contributing neutron capture resonances.

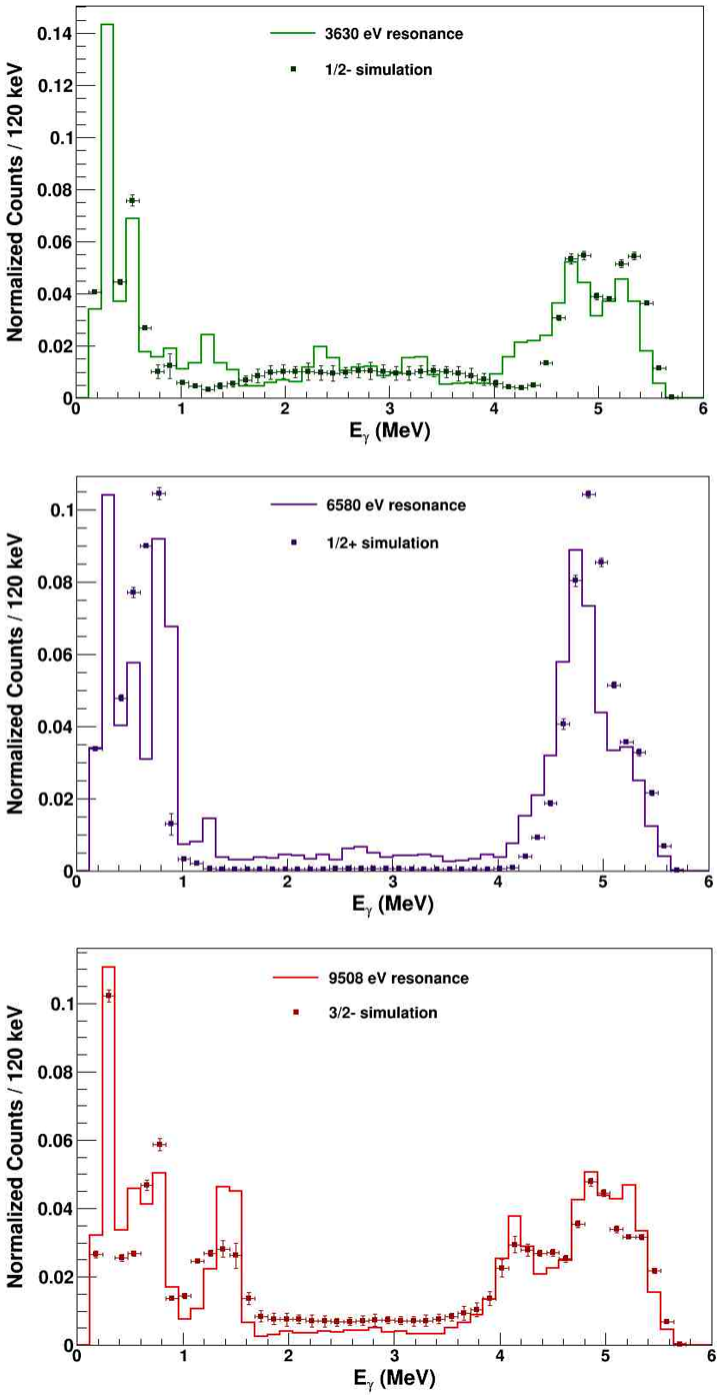

Figure 4.26: Energy of individual γ rays, gated on multiplicity 2, for several strong resonances in the ^{82}Se data compared to simulated data for $J^\pi = \frac{1}{2}+, \frac{1}{2}-, \frac{3}{2}-$. Points correspond to the average across all realizations, while error bars correspond to the standard deviation of the bin content for each realization. The integral of each plot is normalized to unity for a true comparison.

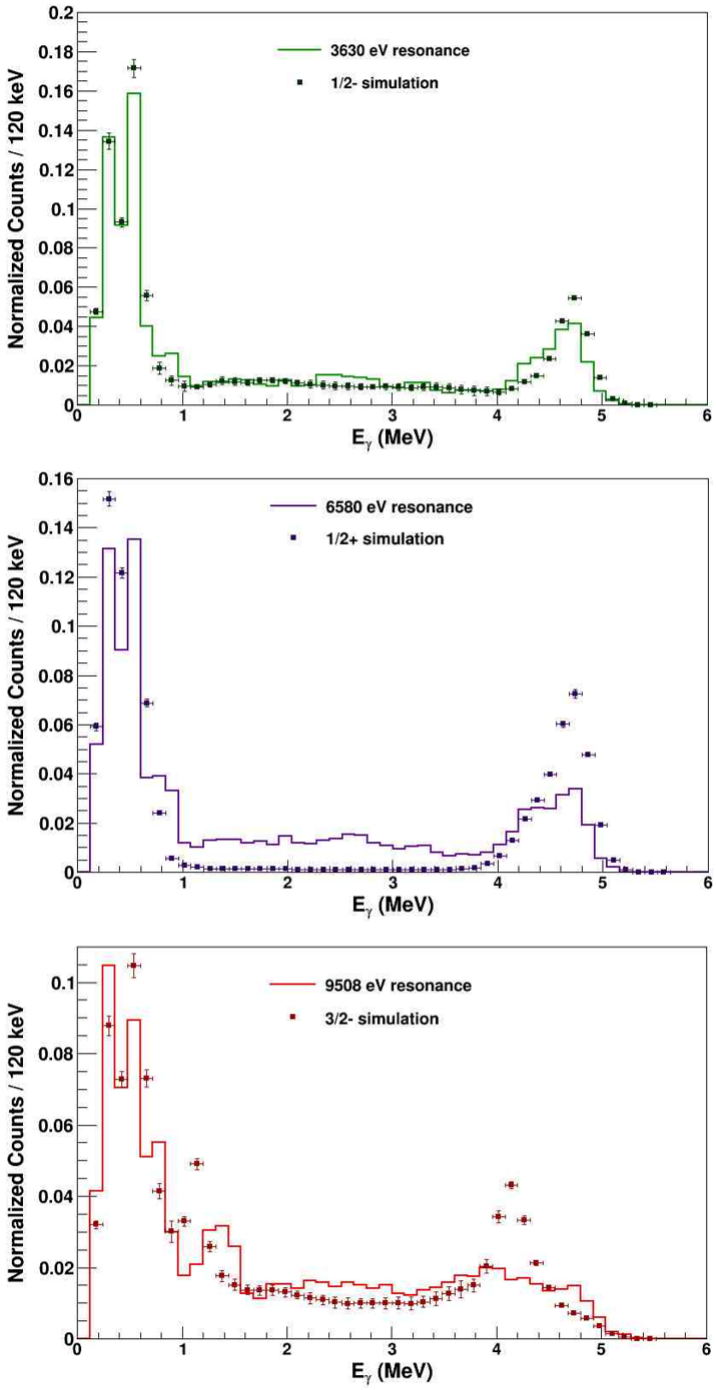

Figure 4.27: Energy of individual γ rays, gated on multiplicity 3, for several strong resonances in the ^{82}Se data compared to simulated data for $J^\pi = \frac{1}{2}+, \frac{1}{2}-, \frac{3}{2}-$. Points correspond to the average across all realizations, while error bars correspond to the standard deviation of the bin content for each realization. The integral of each plot is normalized to unity for a true comparison.

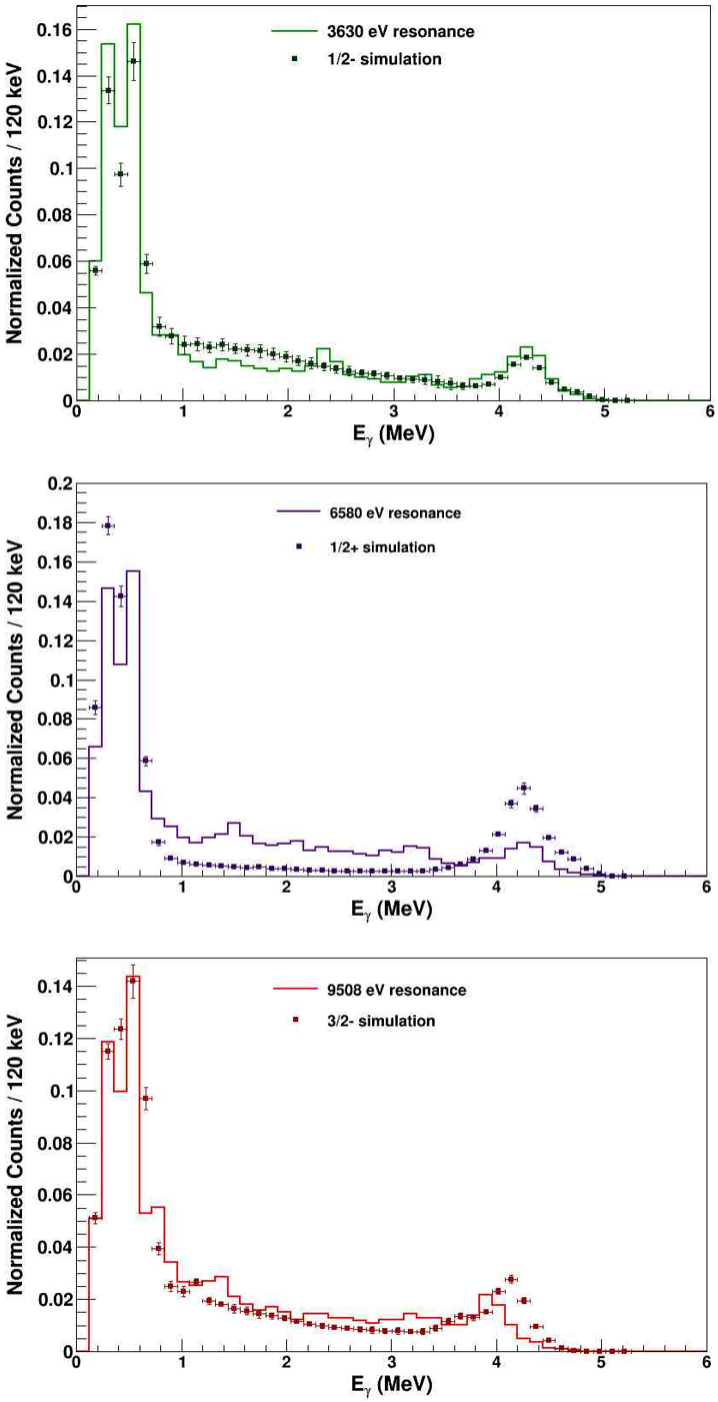

Figure 4.28: Energy of individual γ rays, gated on multiplicity 4, for several strong resonances in the ^{82}Se data compared to simulated data for $J^\pi = \frac{1}{2}+, \frac{1}{2}-, \frac{3}{2}-$. Points correspond to the average across all realizations, while error bars correspond to the standard deviation of the bin content for each realization. The integral of each plot is normalized to unity for a true comparison.

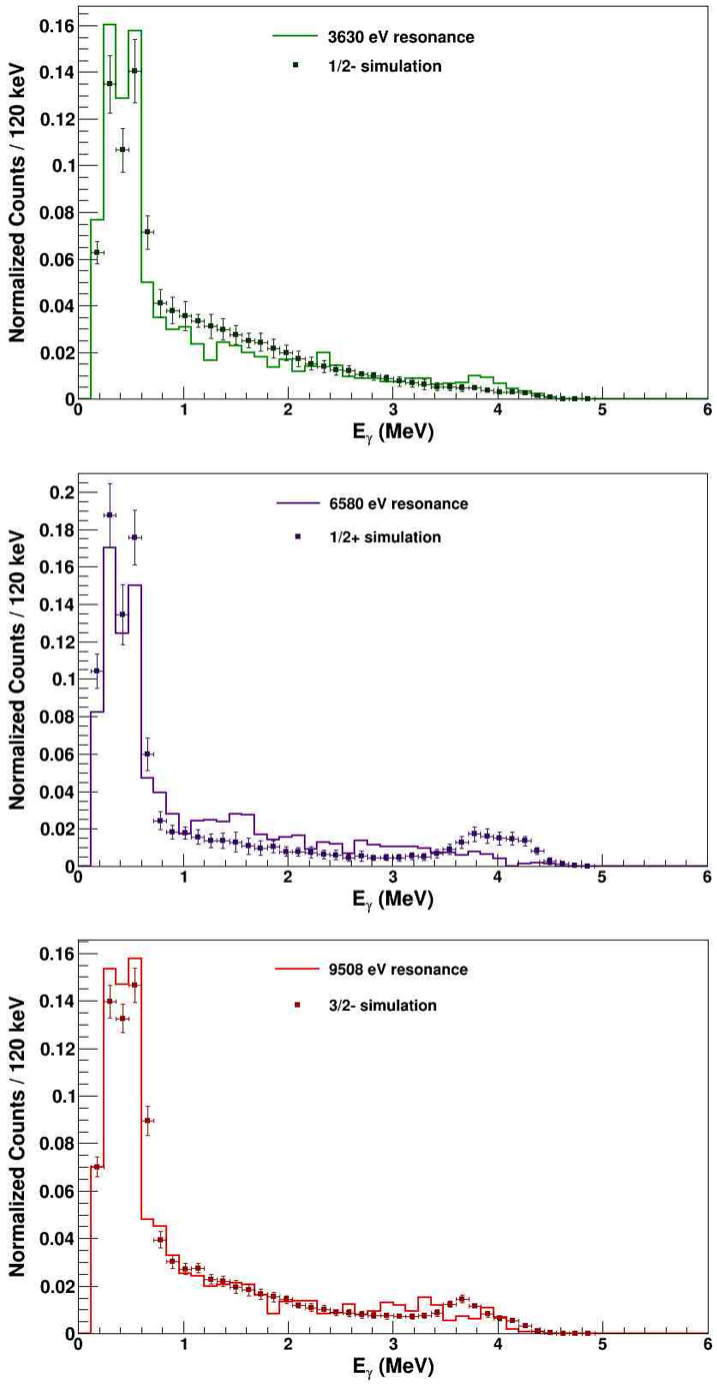

Figure 4.29: Energy of individual γ rays, gated on multiplicity 5, for several strong resonances in the ^{82}Se data compared to simulated data for $J^\pi = \frac{1}{2}+, \frac{1}{2}-, \frac{3}{2}-$. Points correspond to the average across all realizations, while error bars correspond to the standard deviation of the bin content for each realization. The integral of each plot is normalized to unity for a true comparison.

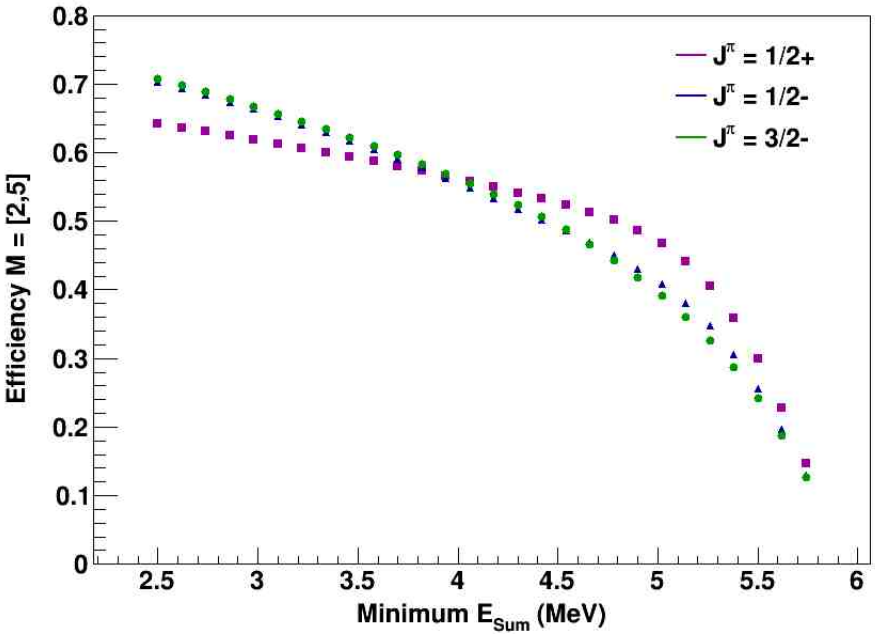

Figure 4.30: Simulation efficiencies and their uncertainties as a function of the lower E_{Sum} gate boundary, for M = [2,5] and an upper E_{Sum} gate boundary of 5.9 MeV.

4.5.3 Cross Section Results

With the yield of neutron capture on ^{82}Se determined and the efficiency of γ rays detected within the E_{Sum} and multiplicity cuts calculated, the cross section of ^{82}Se(n,γ)^{83}Se was determined using Equation 4.6. The results are shown in Figure 4.31. The statistical uncertainty shown in Figure 4.31 includes the uncertainty of the measured yield of neutron capture propagated through all background subtractions, as well as the uncertainty of the beam-monitor yields propagated through the determination of the neutron fluence. In addition to the statistical uncertainty shown, there is a systematic uncertainty of 4.25%. The systemic uncertainty includes the 4% uncertainty from the neutron-fluence normalization and the 0.47% uncertainty from the efficiency, added in quadrature.

The measured cross section was converted to a Maxwellian-Averaged Cross Section (MACS) using Equation 4.12, where μ is the reduced mass, $\sigma(E_n)$ is the cross section at

neutron energy E_n, and $\delta(E_n)$ is the bin width of the bin centered on E_n. At a temperature (kT) of 30 keV the MACS was determined to be 5.67 $\pm$ 4.72 mb. The experimentally determined MACS is in agreement with the recommended theoretical value of 9 $\pm$ 8 mb at 30 keV from the Karlsruhe Astrophysical Database of Nucleosynthesis in Stars (KADoNiS) [98].

$$\sigma^{MACS}(kT) = \frac{2}{\sqrt{\pi}}\left(\frac{\mu}{kT}\right)^2 \sum_{E_n=10eV}^{1MeV} \sigma(E_n)E_n e^{\frac{E_n}{kT}}\delta(E_n) \tag{4.12}$$

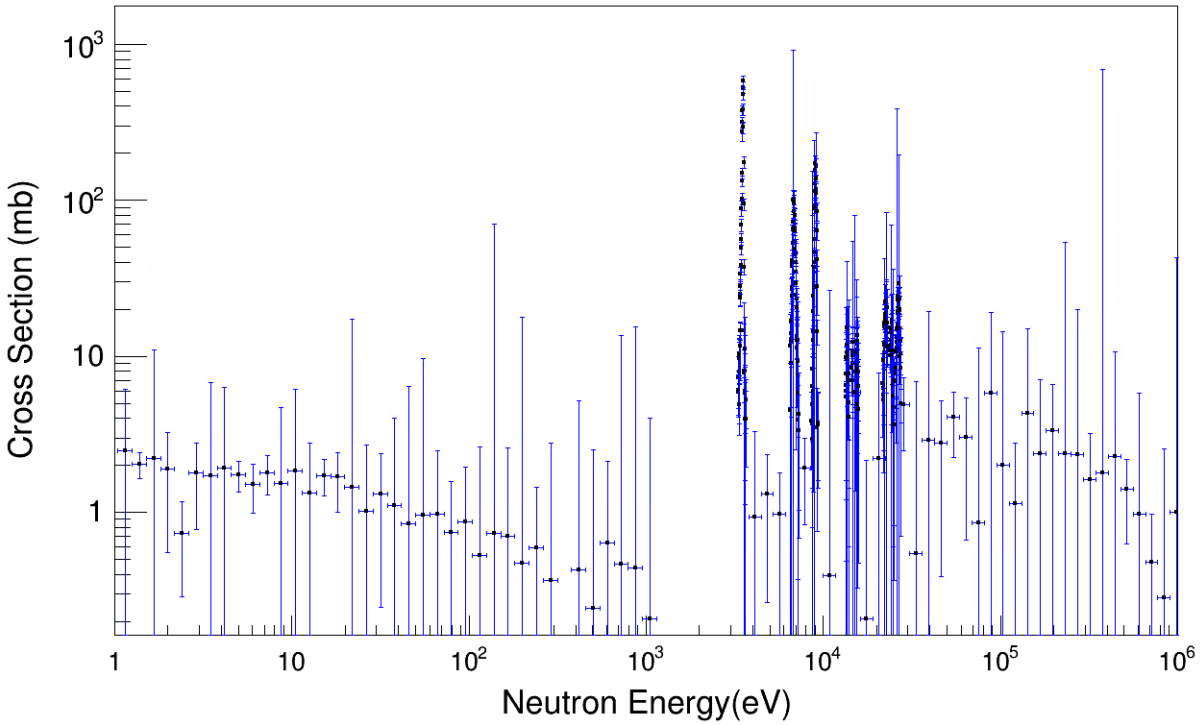

Figure 4.31: Cross section of the ^{82}Se(n,γ)^{83}Se reaction measured with DANCE.

Table 4.3: Efficiencies determined by DICEBOX and GEANT4 simulations (M = [2,5], 5.0 MeV $> E_{Sum} >$ 5.9 MeV) for $J^\pi = \frac{1}{2}+, \frac{1}{2}-, \frac{3}{2}-$. 100000 γ-ray cascades were simulated for 30 realizations of artificial nuclei.

Realization	$J^\pi = \frac{1}{2}+$	$J^\pi = \frac{1}{2}-$	$J^\pi = \frac{3}{2}-$
1	0.468	0.409	0.392
2	0.469	0.413	0.389
3	0.466	0.408	0.394
4	0.470	0.406	0.390
5	0.466	0.406	0.391
6	0.467	0.405	0.390
7	0.466	0.406	0.390
8	0.466	0.408	0.389
9	0.468	0.409	0.392
10	0.466	0.407	0.391
11	0.467	0.410	0.390
12	0.466	0.407	0.389
13	0.469	0.407	0.386
14	0.470	0.408	0.390
15	0.467	0.404	0.387
16	0.468	0.407	0.392
17	0.469	0.405	0.389
18	0.465	0.404	0.391
19	0.467	0.406	0.388
20	0.472	0.409	0.395
21	0.467	0.411	0.395
22	0.467	0.411	0.392
23	0.471	0.411	0.391
24	0.465	0.413	0.386
25	0.468	0.412	0.392
26	0.465	0.406	0.393
27	0.467	0.411	0.394
28	0.466	0.413	0.392
29	0.469	0.408	0.394
30	0.466	0.405	0.390

Chapter 5

Results and Conclusion

5.1 Comparison of β-Oslo Cross Section to Directly Measured Cross Section

The cross section of the ^{82}Se(n,γ)83Se reaction was determined via a direct method and an indirect method. As discussed in Chapter 3, the β-Oslo method was utilized to determine the ^{82}Se(n,γ)83Se cross section through a study of ^{83}As β decay. As discussed in Chapter 4, a direct measurement of neutron capture on ^{82}Se has been measured using the Detector for Advanced Neutron Capture Experiments, DANCE. These two cross section determinations were compared to validate the β-Oslo method. The results are shown in Figure 5.1. The β-Oslo cross section is systematically higher compared to the directly measured cross section. The discrepancy is likely due to the β-Oslo cross section missing the resonance behavior, which is not unsurprising, since TALYS calculates an average cross section. There is better agreement at higher energies (above approximately 40 keV).

5.2 Conclusions and Outlook

The r-process is important to understanding the production of heavy elements, but there is still a lack of knowledge about the r-process, including the astrophysical sites where it takes

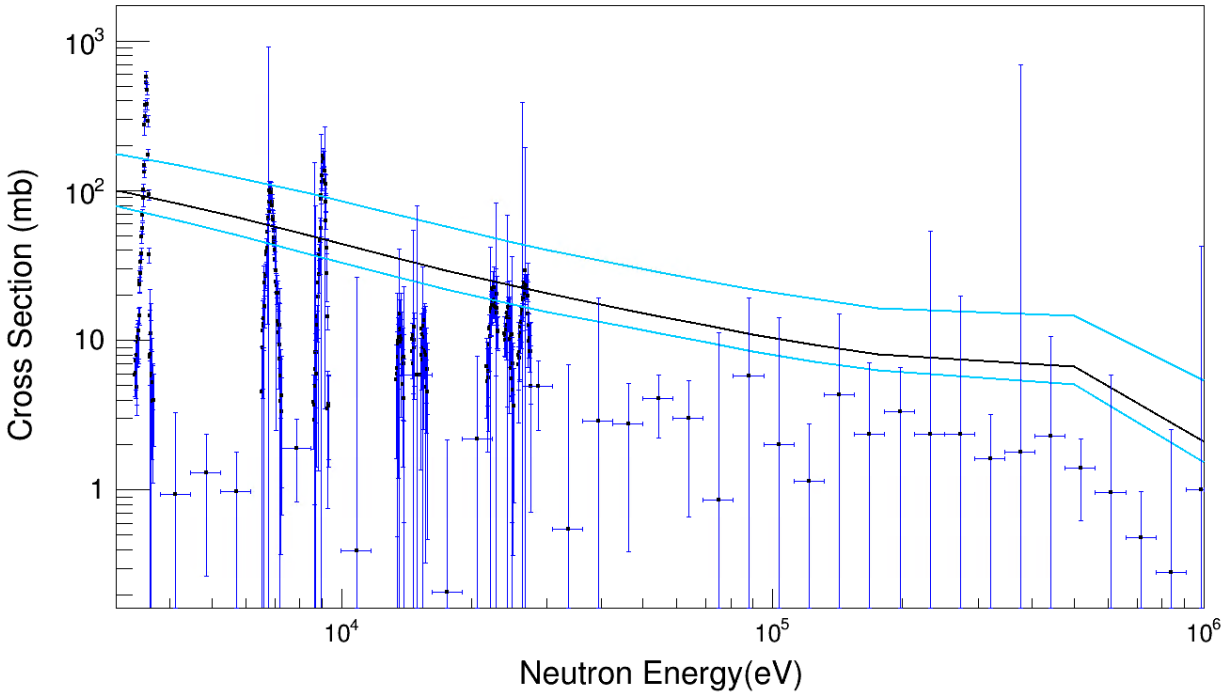

Figure 5.1: Comparison of the directly measured cross section of ^{82}Se(n,γ)^{83}Se (black) to the neutron capture cross section determined via the β-Oslo method (black line). The blue lines indicate the upper and lower limits of the cross section determined via the β-Oslo method through a systematic study of the uncertainty.

place. Models of the r-process can be used to produce abundance patterns with the aim of pinpointing the astrophysical site, but such models require information on nuclear properties of the nuclei involved, including neutron-capture cross sections. The cross sections of the neutron-capture reactions that drive the r-process are a critical piece of information, but presently there is a lack of directly measured neutron-capture cross sections in the neutron-rich region where the r-process takes place. Results from theoretical models are used for cases where experimental data does not exist. The lack of knowledge on the accuracy of these theoretical calculations leads to an inability to reproduce r-process abundance patterns to the degree of certainty needed for successful comparisons to known solar abundance patterns. The β-Oslo method has been developed to constrain neutron-capture cross sections for β-unstable nuclei not amenable to direct measurement, using experimental data from β-decay

studies. The nuclear level density and γ-ray strength function can be extracted from the experimental β-decay data, and used to perform a Hauser-Feschbach calculation of the cross section.

A previous study showed that the cross section of ^{50}Ti$(n,\gamma)^{51}$Ti, obtained via the β-Oslo method, had excellent agreement with a directly measured cross section of ^{50}Ti$(n,\gamma)^{51}$Ti. Since ^{51}Ti is a relatively low mass nucleus with a low level density, a comparison of a higher mass nucleus (and therefore a higher level density) is necessary to validate that the efficacy of the β-Oslo method and the assumptions made in the analysis will hold for higher level densities. The present work has determined a cross section for ^{82}Se$(n,\gamma)^{83}$Se from both a direct measurement of neutron capture on ^{82}Se, and the application of the β-Oslo method on the β decay of ^{83}As to ^{83}Se. The two cross sections are in reasonable agreement. It is recommended to investigate the slight overestimation of the indirectly determined cross section in the future to determine whether the overestimation is a systematic deviation or an artifact of the analysis performed. It is also recommended to perform a validation in a heavier mass region for a nucleus with a higher level density than. Both ^{50}Ti and ^{82}Se are located near shell closures, so it would be advantageous to perform a validation with a nucleus that somewhere between shell closures. Overall, the β-Oslo method has been shown to be a viable method for constraining neutron-capture cross sections.

BIBLIOGRAPHY

BIBLIOGRAPHY

[1] Christopher Sneden, John J Cowan, and Roberto Gallino. Neutron-Capture Elements in the Early Galaxy.

[2] Walter Loveland, David J. Morriessey, and Glenn T. Seaborg. *Modern Nuclear Chemistry*. John Wiley & Sons, Inc., 2006.

[3] M. Arnould, S. Goriely, and K. Takahashi. The r-process of stellar nucleosynthesis: Astrophysics and nuclear physics achievements and mysteries. *Physics Reports*, 450:97–213, 2007.

[4] LIGO Scientific Collaboration and Virgo Collaboration. GW170817: Observation of Gravitational Waves from a Binary Neutron Star Inspiral. *Phys. Rev. Lett.*, 119(16):30–33, 2017.

[5] B. D. Metzger, G. Martínez-Pinedo, S. Darbha, E. Quataert, A. Arcones, D. Kasen, R. Thomas, P. Nugent, I. V. Panov, and N. T. Zinner. Electromagnetic counterparts of compact object mergers powered by the radioactive decay of r-process nuclei. *Monthly Notices of the Royal Astronomical Society*, 406(4):2650–2662, 8 2010.

[6] Daniel Kasen, Brian Metzger, Jennifer Barnes, Eliot Quataert, and Enrico Ramirez-Ruiz. Origin of the heavy elements in binary neutron-star mergers from a gravitational-wave event. *Nature*, 551:80–84, 2017.

[7] M R Drout, A L Piro, B J Shappee, C D Kilpatrick, J D Simon, C Contreras, D A Coulter, R J Foley, M R Siebert, N Morrell, K Boutsia, F Di Mille, S Holoien, D Kasen, J A Kollmeier, B F Madore, A J Monson, A Murguia-Berthier, Y.-C Pan, J X Prochaska, E Ramirez-Ruiz, A Rest, C Adams, K Alatalo, E Bañados, J Baughman, T C Beers, R A Bernstein, T Bitsakis, A Campillay, T T Hansen, C R Higgs, A P Ji, G Maravelias, J L Marshall, C Moni Bidin, J L Prieto, K C Rasmussen, C Rojas-Bravo, A L Strom, N Ulloa, J Vargas-González, Z Wan, and D D Whitten. Light curves of the neutron star merger GW170817/SSS17a: Implications for r-process nucleosynthesis. *Science*, 358:1570–1574, 2017.

[8] M. R. Mumpower, R. Surman, G. C. McLaughlin, and A. Aprahamian. The impact of individual nuclear properties on r-process nucleosynthesis. *Progress in Particle and Nuclear Physics*, 86:86–126, 2016.

[9] S Goriely, N Chamel, and J M Pearson. Skyrme-Hartree-Fock-Bogoliubov Nuclear Mass Formulas: Crossing the 0.6 MeV Accuracy Threshold with Microscopically Deduced Pairing. *Phys. Rev. Lett.*, 102:152503, 2009.

[10] J Duflo and A. P. Zuker. Microscopic mass formulas. *Phys. Rev. C*, 52(1), 1995.

[11] P. Moller, J. R. Nix, W. D. Myers, and W. J. Swiatecki. Nuclear Ground-State Masses and Deformations. *Atomic Data and Nuclear Data Tables*, 59:185–381, 1995.

[12] Arjan Koning, Stephane Hilaire, and Stephane Goriely. TALYS User Manual (v. 1.95). Technical report.

[13] Thomas Rauscher and Friedrich-Karl Thielemann. Astrophysical Reaction Rates From Statistical Model Calculations. *Atomic Data and Nuclear Data Tables*, 75(1-2):1–351, 2000.

[14] M. Beard, E. Uberseder, R. Crowter, and M. Wiescher. Comparison of statistical model calculations for stable isotope neutron capture. *Phys. Rev. C*, 90:034619–undefined, 2014.

[15] G. Savard, R. C. Pardo, S. Baker, C. N. Davids, A. Levand, D. Peterson, D. G. Phillips, T. Sun, R. Vondrasek, B. J. Zabransky, and G. P. Zinkann. CARIBU: A new facility for the study of neutron-rich isotopes. *Hyperfine Interactions*, 199(1):301–309, 7 2011.

[16] J Van Schelt, D Lascar, G Savard, J A Clark, P F Bertone, S Caldwell, A Chaudhuri, A F Levand, G Li, G E Morgan, R Orford, R E Segel, K S Sharma, and M G Sternberg. First Results from the CARIBU Facility: Mass Measurements on the r-Process Path. *Phys. Rev. Lett.*, 111:–undefined, 2013.

[17] J Hakala, J Dobaczewski, D Gorelov, T Eronen, A Jokinen, A Kankainen, V S Kolhinen, M Kortelainen, I D Moore, H Penttilä, S Rinta-Antila, J Rissanen, A Saastamoinen, V Sonnenschein, and J A Ystö. Precision Mass Measurements beyond 132 Sn: Anomalous Behavior of Odd-Even Staggering of Binding Energies.

[18] M Matoš, A Estrade, M Amthor, A Aprahamian, D Bazin, A Becerril, T Elliot, D Galaviz, A Gade, S Gupta, G Lorusso, F Montes, J Pereira, M Portillo, A M Rogers, H Schatz, D Shapira, E Smith, A Stolz, and M Wallace. TOF-Bρ mass measurements of very exotic nuclides for astrophysical calculations at the NSCL. *Journal of Physics G: Nuclear and Particle Physics*, 35:6, 2008.

[19] G Lorusso, S Nishimura, Z Y Xu, A Jungclaus, Y Shimizu, G S Simpson, P.-A Söderström, H Watanabe, F Browne, P Doornenbal, G Gey, H S Jung, B Meyer, T Sumikama, J Taprogge, Zs Vajta, J Wu, H Baba, G Benzoni, K Y Chae, F C L Crespi, N Fukuda, R Gernhäuser, N Inabe, T Isobe, T Kajino, D Kameda, G D Kim, Y.-K Kim, I Kojouharov, F G Kondev, T Kubo, N Kurz, Y K Kwon, G J Lane, Z Li, A Montaner-Pizá, K Moschner, F Naqvi, M Niikura, H Nishibata, A Odahara, R Orlandi, Z Patel, Zs Podolyák, H Sakurai, H Schaffner, P Schury, S Shibagaki, K Steiger, H Suzuki, H Takeda, A Wendt, A Yagi, and K Yoshinaga. β-Decay Half-Lives of 110

Neutron-Rich Nuclei across the N 82 Shell Gap: Implications for the Mechanism and Universality of the Astrophysical r Process. *Phys. Rev. Lett.*, 114, 2015.

[20] M Quinn, A Aprahamian, J Pereira, R Surman, O Arndt, T Baumann, A Becerril, T Elliot, A Estrade, D Galaviz, T Ginter, M Hausmann, S Hennrich, R Kessler, K.-L Kratz, G Lorusso, P F Mantica, M Matos, F Montes, B Pfeiffer, M Portillo, H Schatz, F Schertz, L Schnorrenberger, E Smith, A Stolz, W B Walters, and A Wöhr. β decay of nuclei around 90Se: Search for signatures of a N = 56 subshell closure relevant to the r process. *Phys. Rev. C*, 85:35807, 2012.

[21] A I Morales, J Benlliure, T Kurtukián-Nieto, K.-H Schmidt, S Verma, P H Regan, Z Podolyák, M Górska, S Pietri, R Kumar, E Casarejos, N Al-Dahan, A Algora, N Alkhomashi, H Álvarez-Pol, G Benzoni, A Blazhev, P Boutachkov, A M Bruce, L S Cáceres, I J Cullen, A M Denis Bacelar, P Doornenbal, M E Estévez-Aguado, G Farrelly, Y Fujita, A B Garnsworthy, W Gelletly, J Gerl, J Grebosz, R Hoischen, I Kojouharov, N Kurz, S Lalkovski, Z Liu, C Mihai, F Molina, D Mücher, B Rubio, H Shaffner, S J Steer, A Tamii, S Tashenov, J J Valiente-Dobón, P M Walker, H J Wollersheim, and P J Woods. Half-Life Systematics across the N 126 Shell Closure: Role of First-Forbidden Transitions in the β Decay of Heavy Neutron-Rich Nuclei. *Phys. Rev. Lett.*, 113, 2014.

[22] T. Kurtukian-Nieto, J. Benlliure, K. H. Schmidt, L. Audouin, F. Becker, B. Blank, I. N. Borzov, E. Casarejos, F. Farget, M. Fernández-Ordóñez, J. Giovinazzo, D. Henzlova, B. Jurado, K. Langanke, G. Martínez-Pinedo, J. Pereira, and O. Yordanov. Beta-decay half-lives of new neutron-rich isotopes of Re, Os and Ir approaching the r-process path near N = 126. *Eur. Phys. J. A*, 50(9):1–8, 2014.

[23] A. C. Larsen, A. Spyrou, S. N. Liddick, and M. Guttormsen. Novel techniques for constraining neutron-capture rates relevant for r-process heavy-element nucleosynthesis. *Progress in Particle and Nuclear Physics*, 2019.

[24] Walter Hauser and Herman Feshbach. The inelastic scattering of neutrons. *Physical Review*, 87(2):366–373, 1952.

[25] N Bohr, R Peierls, and G Placzek. Nuclear Reactions in the Continuous Energy Region. *Nature*, 144:200–201, 1939.

[26] A J Koning and J P Delaroche. Local and global nucleon optical models from 1 keV to 200 MeV. *Nucl. Phys. A*, 713:231–310, 2003.

[27] J.-P Jeukenne, A Lejeune, and C Mahaux˜. Microscopic calculation of the symmetry and Coulomb components of the complex optical-model potential. *Phys. Rev. C*, 15(1):10–29, 1977.

[28] Torleif Ericson. The statistical model and nuclear level densities. *Advances in Physics*, 9(36):425–511, 1960.

[29] T Von Egidy and D Bucurescu. Experimental energy-dependent nuclear spin distributions. *Phys. Rev. C*, 80:54310, 2009.

[30] H. A. Bethe. Nuclear Physics B. Nuclear Dynamics, Theoretical. *Rev. Mod. Phys.*, 9:69, 1937.

[31] W Dilg, W Schantl, H Vonach, and M Uhl. Level density parameters for the back-shifted fermi gas model in the mass range 40 ¡ A ¡ 250. *Nuclear Physics A*, 217:269–298, 1973.

[32] A. G. W. Cameron. Nuclear Level Spacings. *Can. J. Phys.*, 36:1040–1057, 1958.

[33] T. D. Newton. Shell Effects on the Spacing of Nuclear Levels. *Can. J. Phys*, 34:804–829, 1956.

[34] A Gilbert and A G W Cameron. A composite nuclear level density formula with shell corrections. *Can. J. Phys.*, 43:1446, 1965.

[35] A. Gilbert, F. S. Chen, and A. G. W. Cameron. Level Densities in Lighter Nuclei. *Can. J. Phys*, 43:1248–1258, 1965.

[36] S. Goriely, F. Tondeur, and J. M. Pearson. a HartreeFock Nuclear Mass Table. *Atomic Data and Nuclear Data Tables*, 77(2):311–381, 2001.

[37] S Goriely, S Hilaire, and A J Koning. Improved microscopic nuclear level densities within the Hartree-Fock-Bogoliubov plus combinatorial method. *Phys. Rev. C*, 78:64307, 2008.

[38] S Hilaire, M Girod, S Goriely, and A J Koning. Temperature-dependent combinatorial level densities with the D1M Gogny force. *Phys. Rev. C*, 86:064317, 2012.

[39] M Krticka and F Bevá. What do we really know about photon strength functions? Related content Scissors mode of Gd nuclei measured, with the DANCE detector. *Journal of Physics G*, 35:014025, 2007.

[40] D M Brink. Individual Particle and Collective Aspects of the Nuclear Photoeffect. *Nuclear Physics*, 4:215–220, 1957.

[41] Peter Axel. Electric Dipole Ground-State Transition Width Strength Function and 7-Mev Photon Interactions. *Phys. Rev.*, 126(2), 1962.

[42] J Kopecky and M Uhl. Test of gamma-ray strength functions in nuclear reaction model calculations. *Phys. Rev. C*, 41(5), 1990.

[43] A Voinov, E Algin, U Agvaanluvsan, T Belgya, R Chankova, M Guttormsen, G E Mitchell, J Rekstad, A Schiller, and S Siem. Large Enhancement of Radiative Strength for Soft Transitions in the Quasicontinuum. *Phys. Rev. Lett*, 93(14), 2004.

[44] M. Guttormsen, R. Chankova, U. Agvaanluvsan, E. Algin, L. A. Bernstein, F. Ingebretsen, T. Lönnroth, S. Messelt, G. E. Mitchell, J. Rekstad, A. Schiller, S. Siem, A. C. Sunde, A. Voinov, and S. Ødegård. Radiative strength functions in 93-98Mo. *Phys. Rev. C*, 71(4):044307–undefined, 2005.

[45] M Wiedeking, L A Bernstein, M Krtička, D L Bleuel, J M Allmond, M S Basunia, J T Burke, P Fallon, R B Firestone, B L Goldblum, R Hatarik, P T Lake, I-Y Lee, S R Lesher, S Paschalis, M Petri, L Phair, and N D Scielzo. Low-Energy Enhancement in the Photon Strength of 95Mo. *Phys. Rev. Lett.*, 108:162503, 2012.

[46] A. C. Larsen, M. Guttormsen, R. Chankova, F. Ingebretsen, T. Lönnroth, S. Messelt, J. Rekstad, A. Schiller, S. Siem, N. U. H. Syed, and A. Voinov. Nuclear level densities and γ-ray strength functions in Sc44,45. *Physical Review C*, 76(4):044303, 2007.

[47] A. Bürger, A. C. Larsen, S. Hilaire, M. Guttormsen, S. Harissopulos, M. Kmiecik, T. Konstantinopoulos, M. Krtička, A. Lagoyannis, T. Lönnroth, K. Mazurek, M. Norrby, H. T. Nyhus, G. Perdikakis, S. Siem, A. Spyrou, and N. U.H. Syed. Nuclear level density and γ-ray strength function of 43Sc. *Physical Review C - Nuclear Physics*, 85(6):1–5, 2012.

[48] B. V. Kheswa, M. Wiedeking, F. Giacoppo, S. Goriely, M. Guttormsen, A. C. Larsen, F. L. Bello Garrote, T. K. Eriksen, A. Görgen, T. W. Hagen, P. E. Koehler, M. Klintefjord, H. T. Nyhus, P. Papka, T. Renstrøm, S. Rose, E. Sahin, S. Siem, and T. Tornyi. Galactic production of 138La: Impact of 138,139La statistical properties. *Phys. Lett. B*, 744:268–272, 5 2015.

[49] A Simon, M Guttormsen, A C Larsen, C W Beausang, P Humby, J T Burke, R J Casperson, R O Hughes, T J Ross, J M Allmond, R Chyzh, M Dag, J Koglin, E Mccleskey, M Mccleskey, S Ota, and A Saastamoinen. First observation of low-energy γ-ray enhancement in the rare-earth region. *Phys. Rev. C*, 93(3):034303–undefined, 2016.

[50] A. C. Larsen and S. Goriely. Impact of a low-energy enhancement in the γ-ray strength function on the neutron-capture cross section. *Physical Review C - Nuclear Physics*, 82(1):1–7, 2010.

[51] A C Larsen, N Blasi, A Bracco, F Camera, T K Eriksen, A Görgen, M Guttormsen, T W Hagen, S Leoni, B Million, H T Nyhus, T Renstrøm, S J Rose, I E Ruud, S Siem, T Tornyi, G M Tveten, A V Voinov, and M Wiedeking. Evidence for the Dipole Nature of the Low-Energy Enhancement in 56 Fe. *Phys. Rev. Lett.*, 111:242504, 2013.

[52] M D Jones, A O Macchiavelli, M Wiedeking, L A Bernstein, H L Crawford, C M Campbell, R M Clark, M Cromaz, P Fallon, I Y Lee, M Salathe, A Wiens, A D Ayangeakaa, D L Bleuel, S Bottoni, M P Carpenter, H M Davids, J Elson, A Görgen, M Guttormsen, R V F Janssens, J E Kinnison, L Kirsch, A C Larsen, T Lauritsen, W Reviol, D G

Sarantites, S Siem, A V Voinov, and S Zhu. Examination of the low-energy enhancement of the γ-ray strength function of 56Fe. *Phys. Rev. C*, 97:24327, 2018.

[53] B. Alex Brown and A.C. Larsen. Large Low-Energy M1Strength for Fe-56,57 within the Nuclear Shell Model. *Physical Review Letters*, 113(25), 12 2014.

[54] S Goriely and E Khan. Large-scale QRPA calculation of E1-strength and its impact on the neutron capture cross section. *Nuclear Physics A*, 706:217–232, 2002.

[55] S. Goriely, E. Khan, and M. Samyn. Microscopic HFB + QRPA predictions of dipole strength for astrophysics applications. *Nuclear Physics A*, 739:331–352, 7 2004.

[56] J E Escher, J T Burke, R O Hughes, N D Scielzo, R J Casperson, S Ota, H I Park, A Saastamoinen, and T J Ross. Constraining neutron capture cross sections for unstable nuclei with surrogate reaction data and theory. *Phys. Rev. Lett.*, 121:052501, 2018.

[57] H. Utsunomiya, S. Goriely, H. Akimune, H. Harada, F. Kitatani, S. Goko, H. Toyokawa, K. Yamada, T. Kondo, O. Itoh, M. Kamata, T. Yamagata, Y.-W. Lui, I. Daoutidis, D. P. Arteaga, S. Hilaire, and A. J. Koning. γ-ray strength function method and its application to 107Pd. *Phys. Rev. C*, 82:064610–undefined, 2010.

[58] H Utsunomiya, S Goriely, T Kondo, C Iwamoto, H Akimune, T Yamagata, H Toyokawa, H Harada, F Kitatani, Y.-W Lui, A C Larsen, M Guttormsen, P E Koehler, S Hilaire, S Péru, M Martini, and A J Koning. Photoneutron cross sections for Mo isotopes: A step toward a unified understanding of (γ,n) and (n,γ) reactions. *Phys. Rev. C*, 88:15805, 2013.

[59] M Guttormsen, T S Tveter, L Bergholt, F Ingebretsen, and J Rekstad. The unfolding of continuum y-ray spectra. *Nuclear Instruments and Methods in Physics Research A*, 374:371–376, 1996.

[60] M Guttormsen, T Ramsoy, and J Rekstad. The First Generation γ-rays From Hot Nuclei. *Nuclear Instruments and Methods in Physics Research*, 255:518–523, 1987.

[61] A. Schiller, L. Bergholt, M. Guttormsen, E. Melby, J. Rekstad, and S. Siem. Extraction of level density and γ strength function from primary γ spectra. *Nuclear Instruments and Methods in Physics Research, Section A: Accelerators, Spectrometers, Detectors and Associated Equipment*, 447(3):498–511, 2000.

[62] A. C. Larsen, M. Guttormsen, M. Krtička, E. Běták, A. Bürger, A. Görgen, H. T. Nyhus, J. Rekstad, A. Schiller, S. Siem, H. K. Toft, G. M. Tveten, A. V. Voinov, and K. Wikan. Analysis of possible systematic errors in the Oslo method. *Physical Review C - Nuclear Physics*, 83(3):1–23, 2011.

[63] A. Spyrou, S. N. Liddick, A. C. Larsen, M. Guttormsen, K. Cooper, A. C. Dombos, D. J. Morrissey, F. Naqvi, G. Perdikakis, S. J. Quinn, T. Renstrøm, J. A. Rodriguez, A. Simon, C. S. Sumithrarachchi, and R. G. T. Zegers. Novel technique for Constraining r-Process (n,γ) Reaction Rates. *Physical Review Letters*, 113(23):232502, 2014.

[64] A Ratkiewicz, J A Cizewski, J E Escher, G Potel, J T Burke, R J Casperson, M Mccleskey, R A E Austin, S Burcher, R O Hughes, B Manning, S D Pain, W A Peters, S Rice, T J Ross, N D Scielzo, C Shand, and K Smith. Towards Neutron Capture on Exotic Nuclei: Demonstrating (d,pγ) as a Surrogate Reaction for (n,γ). *Phys. Rev. Lett.*, 122:052502, 2019.

[65] T A Laplace, F Zeiser, M Guttormsen, A C Larsen, D L Bleuel, L A Bernstein, B L Goldblum, S Siem, F L Bello Garotte, J A Brown, L Crespo Campo, T K Eriksen, F Giacoppo, A Görgen, K Hadynska, Hadynska-Klek Klek, R A Henderson, M Klintefjord, M Lebois, T Renstrøm, S J Rose, E Sahin, T G Tornyi, G M Tveten, A Voinov, M Wiedeking, J N Wilson, and W Younes. Statistical properties of 243 Pu, and 242 Pu(n,γ) cross section calculation. *Phys. Rev. C*, 93:014323–undefined, 2016.

[66] T. G. Tornyi, M. Guttormsen, T. K. Eriksen, A. Görgen, F. Giacoppo, T. W. Hagen, A. Krasznahorkay, A. C. Larsen, T. Renstrøm, S. J. Rose, S. Siem, and G. M. Tveten. Level density and γ-ray strength function in the odd-odd Np238 nucleus. *Phys. Rev. C*, 89:044323–undefined, 2014.

[67] B V Kheswa, M Wiedeking, J A Brown, A C Larsen, S Goriely, M Guttormsen, F L Bello Garrote, L A Bernstein, D L Bleuel, T K Eriksen, F Giacoppo, A Görgen, B L Goldblum, T W Hagen, P E Koehler, M Klintefjord, K L Malatji, J E Midtbø, H T Nyhus, P Papka, T Renstrøm, S J Rose, E Sahin, S Siem, and T G Tornyi. 137,138,139 La(n,γ) cross sections constrained with statistical decay properties of 138,139,140 La nuclei. *Phys. Rev. C*, 95:045805, 2017.

[68] S N Liddick, A C Larsen, M Guttormsen, A Spyrou, B P Crider, F Naqvi, J E Midtbø, F L Bello Garrote, D L Bleuel, L Crespo Campo, A Couture, A C Dombos, F Giacoppo, A Görgen, K Hadynska-Klek, T W Hagen, V W Ingeberg, B V Kheswa, R Lewis, S Mosby, G Perdikakis, C J Prokop, S J Quinn, T Renstrøm, S J Rose, E Sahin, S Siem, G M Tveten, M Wiedeking, and F Zeiser. Benchmarking the extraction of statistical neutron capture cross sections on short-lived nuclei for applications using the beta-Oslo method. *Phys. Rev. C*, 100:024624, 2019.

[69] D. J. Morrissey, B. M. Sherrill, M. Steiner, A. Stolz, and I. Wiedenhoever. Commissioning the A1900 projectile fragment separator. *Nuclear Instruments and Methods in Physics Research, Section B: Beam Interactions with Materials and Atoms*, 204:90–96, 2003.

[70] A. Stolz, T. Baumann, T. N. Ginter, D. J. Morrissey, M. Portillo, B. M. Sherrill, M. Steiner, and J. W. Stetson. Production of rare isotope beams with the NSCL

fragment separator. *Nuclear Instruments and Methods in Physics Research, Section B: Beam Interactions with Materials and Atoms*, 241:858–861, 12 2005.

[71] A. Simon, S. J. Quinn, A. Spyrou, A. Battaglia, I. Beskin, A. Best, B. Bucher, M. Couder, P. A. Deyoung, X. Fang, J. Gorres, A. Kontos, Q. Li, S. N. Liddick, A. Long, S. Lyons, K. Padmanabhan, J. Peace, A. Roberts, D. Robertson, K. Smith, M. K. Smith, E. Stech, B. Stefanek, W. P. Tan, X. D. Tang, and M. Wiescher. SuN: Summing NaI(Tl) gamma-ray detector for capture reaction measurements. *Nuclear Instruments and Methods in Physics Research, Section A: Accelerators, Spectrometers, Detectors and Associated Equipment*, 703:16–21, 2013.

[72] H. Bateman. The solution of a system of differential equations occurring in the theory of radioactive transformations. *Proc. Cambridge Philos. Soc.*, 15:423–427, 1910.

[73] Daniel Abriola, Melih Bostan, Sefa Erturk, Manssour Fadil, Monica Galan, Sakari Juutinen, Tibor Kibédi, Filip Kondev, Aurelian Luca, Alexandru Negret, Ninel Nica, Bernd Pfeiffer, Balraj Singh, Alejandro Sonzogni, Janos Timar, Jagdish Tuli, Tsanka Venkova, and Kazimierz Zuber. Nuclear Data Sheets for A = 84. *Nuclear Data Sheets*, 110:2815–2944, 2009.

[74] E. A. McCutchan. Nuclear data sheets for A = 83. *Nuclear Data Sheets*, 125:201–394, 2015.

[75] Rebecca L Lewis. *Indirect Neutron-capture Cross Sections for the Weak r-process*. PhD thesis, Michigan State University, 2019.

[76] M. Guttormsen. Matrix Manipulation Program (MAMA), 2019.

[77] M. Guttormsen, A. C. Larsen, A. Gorgen, T. Renstrom, S. Siem, T. G. Tornyi, and G. M. Tveten. Validity of the Generalized Brink-Axel Hypothesis in Np 238. *Physical Review Letters*, 116(1):1–5, 2016.

[78] J. Allison, K. Amako, J. Apostolakis, P. Arce, M. Asai, T. Aso, E. Bagli, A. Bagulya, S. Banerjee, G. Barrand, B. R. Beck, A. G. Bogdanov, D. Brandt, J. M.C. Brown, H. Burkhardt, Ph Canal, D. Cano-Ott, S. Chauvie, K. Cho, G. A.P. Cirrone, G. Cooperman, M. A. Cortés-Giraldo, G. Cosmo, G. Cuttone, G. Depaola, L. Desorgher, X. Dong, A. Dotti, V. D. Elvira, G. Folger, Z. Francis, A. Galoyan, L. Garnier, M. Gayer, K. L. Genser, V. M. Grichine, S. Guatelli, P. Guèye, P. Gumplinger, A. S. Howard, I. Hřivnáčová, S. Hwang, S. Incerti, A. Ivanchenko, V. N. Ivanchenko, F. W. Jones, S. Y. Jun, P. Kaitaniemi, N. Karakatsanis, M. Karamitrosi, M. Kelsey, A. Kimura, T. Koi, H. Kurashige, A. Lechner, S. B. Lee, F. Longo, M. Maire, D. Mancusi, A. Mantero, E. Mendoza, B. Morgan, K. Murakami, T. Nikitina, L. Pandola, P. Paprocki, J. Perl, I. Petrović, M. G. Pia, W. Pokorski, J. M. Quesada, M. Raine, M. A. Reis, A. Ribon, A. Ristić Fira, F. Romano, G. Russo, G. Santin, T. Sasaki, D. Sawkey, J. I. Shin, I. I. Strakovsky, A. Taborda, S. Tanaka, B. Tomé, T. Toshito, H. N. Tran, P. R.

Truscott, L. Urban, V. Uzhinsky, J. M. Verbeke, M. Verderi, B. L. Wendt, H. Wenzel, D. H. Wright, D. M. Wright, T. Yamashita, J. Yarba, and H. Yoshida. Recent developments in GEANT4. *Nucl. Instr. Meth. Phys. Res. A*, 835:186–225, 11 2016.

[79] M. Guttormsen, A.C. Larsen, A. Spyrou, S.N. Liddick, and F. Zeiser. Unfolding of excitation-energy spectra from total absorption γ-ray spectroscopy for the β-Oslo method. In Preparation. 2020.

[80] A.V. Ignatyuk. Contribution to the Second CRP Meeting on RIPL. Technical report, Vienna, 11 1996.

[81] P. Carlos, H. Beil, R. Bergere, J. Fagot, A. Lepretre, A. Veyssiere, and G. V. Solodukhov. A Study of the Photoneutron Contribution to the Giant Dipole Resonance of Nuclei in the 64 ¡ A ¡ 86 Mass Region. *Nuclear Physics*, 258:365–387, 1976.

[82] S.F. Mughabghab. *Atlas of Neutron Resonances: Resonance Parameters and Thermal Cross Sections Z = 1-100.* Elsevier, 5th edition, 2006.

[83] A.V. Ignatyuk, J.L. Well, S. Raman, and S. Kahane. Density of discrete levels in 116Sn. *Phys. Rev. C*, 47:1504–undefined, 1993.

[84] R. Capote, M. Herman, P. Obložinský, P. G. Young, S. Goriely, T. Belgya, A. V. Ignatyuk, A. J. Koning, S. Hilaire, V. A. Plujko, M. Avrigeanu, O. Bersillon, M. B. Chadwick, T. Fukahori, Zhigang Ge, Yinlu Han, S. Kailas, J. Kopecky, V. M. Maslov, G. Reffo, M. Sin, E. Sh Soukhovitskii, and P. Talou. RIPL - Reference Input Parameter Library for Calculation of Nuclear Reactions and Nuclear Data Evaluations. *Nuclear Data Sheets*, 110(12):3107–3214, 2009.

[85] S. Goriely. Radiative neutron captures by neutron-rich nuclei and the r-process nucleosynthesis. *Phys. Lett. B*, 436(1-2):10–18, 1998.

[86] M. Heil, R. Reifarth, M. M. Fowler, R. C. Haight, F. Käppeler, R. S. Rundberg, E. H. Seabury, J. L. Ullmann, J. B. Wilhelmy, and K. Wisshak. 4π BaF2 detector for (n,γ) cross-section measurements at a spallation neutron source. *Nuclear Instruments and Methods in Physics Research, Section A: Accelerators, Spectrometers, Detectors and Associated Equipment*, 459:229–246, 2001.

[87] C J Prokop, A Couture, S Jones, S Mosby, G Rusev, J Ullmann, and M Krtička. Measurement of the 65Cu(n, γ) cross section using the Detector for Advanced Neutron Capture Experiments at LANL. *Phys. Rev. C*, 99, 2019.

[88] S. Mosby, F. Tovesson, A. Couture, D. L. Duke, V. Kleinrath, R. Meharchand, K. Meierbachtol, J. M. ODonnell, B. Perdue, D. Richman, and D. Shields. A fission fragment detector for correlated fission output studies. *Nuclear Instruments and Methods in Physics*

Research, Section A: Accelerators, Spectrometers, Detectors and Associated Equipment, 757:75–81, 9 2014.

[89] P W Lisowski, C D Bowman, G J Russell, and S A Wender. The Los Alamos National Laboratory Spallation Neutron Sources. *Nuclear Science and Engineering*, 106(2):208–218, 10 1990.

[90] D Habs, F S Stephens, and R M Diamond. A Proposal for a Crystal-Ball Detector System. Technical report, 1979.

[91] M. Jandel, T. A. Bredeweg, A. Couture, M. M. Fowler, E. M. Bond, M. B. Chadwick, R. R.C. Clement, E. I. Esch, J. M. O'Donnell, R. Reifarth, R. S. Rundberg, J. L. Ullmann, D. J. Vieira, J. B. Wilhelmy, J. M. Wouters, R. A. Macri, C. Y. Wu, and J. A. Becker. GEANT4 simulations of the DANCE array. *Nuclear Instruments and Methods in Physics Research, Section B: Beam Interactions with Materials and Atoms*, 261(1-2 SPEC. ISS.):1117–1121, 8 2007.

[92] A. Couture and R. Reifarth. Direct measurements of neutron capture on radioactive isotopes. *Atomic Data and Nuclear Data Tables*, 2007.

[93] Saint-Gobain Crystals. BaF 2 Barium Fluoride Scintillation Material, 2016.

[94] Jan M. Wouters, Ana Alpizar Vicente, Todd A. Bredeweg, Ernst Esch, Robert C. Haight, Robert Hatarik, John M. O'Donnell, Rene Reifarth, Robert S. Rundberg, Jon M. Schwantes, Steven A. Sheets, John L. Ullmann, David J. Vieira, and Jerry B. Wilhelmy. Acquisition - Analysis system for the DANCE (detector for advanced neutron capture experiments) BaF 2 gamma-ray calorimeter. *IEEE Transactions on Nuclear Science*, 53(3):880–885, 6 2006.

[95] Trace Sciences International. Stable Isotopes Supplier.

[96] M. B. Chadwick, M. Herman, P. Obložinský, M. E. Dunn, Y. Danon, A. C. Kahler, D. L. Smith, B. Pritychenko, G. Arbanas, R. Arcilla, R. Brewer, D. A. Brown, R. Capote, A. D. Carlson, Y. S. Cho, H. Derrien, K. Guber, G. M. Hale, S. Hoblit, S. Holloway, T. D. Johnson, T. Kawano, B. C. Kiedrowski, H. Kim, S. Kunieda, N. M. Larson, L. Leal, J. P. Lestone, R. C. Little, E. A. McCutchan, R. E. MacFarlane, M. MacInnes, C. M. Mattoon, R. D. McKnight, S. F. Mughabghab, G. P.A. Nobre, G. Palmiotti, A. Palumbo, M. T. Pigni, V. G. Pronyaev, R. O. Sayer, A. A. Sonzogni, N. C. Summers, P. Talou, I. J. Thompson, A. Trkov, R. L. Vogt, S. C. van der Marck, A. Wallner, M. C. White, D. Wiarda, and P. G. Young. ENDF/B-VII.1 nuclear data for science and technology: Cross sections, covariances, fission product yields and decay data. *Nuclear Data Sheets*, 112(12):2887–2996, 12 2011.

[97] F. Becvar. Simulation of gamma cascades in complex nuclei with emphasis on assessment of uncertainties of cascade-related quantities. *Nuclear Instruments and Methods in Physics Research A*, 417:434–449, 1998.

[98] I. Dillmann, R. Plag, F Kappeler, and T. Rauscher. The third update of the "Karlsruhe Astrophysical Database of Nucleosynthesis in Stars". *EFNUDAT Fast Neutrons, Proceedings of the Scientific Workshop on Neutron Measurements*, 2009.